

DISSERTATION

INTRASEASONAL VARIABILITY IN THE TROPICAL DIURNAL CYCLE

Submitted by

Michael B. Natoli

Department of Atmospheric Science

In partial fulfillment of the requirements

For the Degree of Doctor of Philosophy

Colorado State University

Fort Collins, Colorado

Spring 2022

Doctoral Committee:

Advisor: Eric D. Maloney

Michael M. Bell

David A. Randall

Jeffrey D. Niemann

Copyright by Michael B. Natoli 2022

All Rights Reserved

## ABSTRACT

### INTRASEASONAL VARIABILITY IN THE TROPICAL DIURNAL CYCLE

The relationship between large-scale intraseasonal variability in tropical convection and the local diurnal cycle on tropical islands is explored with observations and an idealized model. In part one, the impact of quasi-biweekly variability in the monsoon southwesterly winds on the precipitation diurnal cycle in the Philippines is examined using CMORPH precipitation, ERA5 reanalysis, and outgoing longwave radiation (OLR) fields. Both a case study during the 2018 Propagation of Intraseasonal Tropical Oscillations (PISTON) field campaign and a 23-year composite analysis are used to understand the effect of the QBWO on the diurnal cycle. QBWO events in the west Pacific, identified with an extended EOF index, bring increases in moisture, cloudiness, and westerly winds to the Philippines. Such events are associated with significant variability in daily mean precipitation and the diurnal cycle. It is shown that the modulation of the diurnal cycle by the QBWO is remarkably similar to that by the boreal summer intraseasonal oscillation (BSISO). The diurnal cycle reaches a maximum amplitude on the western side of the Philippines on days with average to above average moisture, sufficient insolation, and weakly offshore prevailing wind. This occurs during the transition period from suppressed to active large-scale convection for both the QBWO and BSISO. Westerly monsoon surges associated with QBWO variability generally exhibit active precipitation over the South China Sea (SCS), but a depressed diurnal cycle. These results highlight that modes of large-scale convective variability in the tropics can have a similar impact on the diurnal cycle if they influence the local scale environmental background state similarly.

In part two, a specific large-scale mode is neglected, and the impact of variability in the background wind at any timescale on the local diurnal cycle is isolated. Luzon Island in the northern Philippines is used as an observational test case. Composite diurnal cycles of CMORPH precipitation are constructed based on an index derived from the first empirical orthogonal function (EOF)

of ERA5 zonal wind profiles. A strong precipitation diurnal cycle and pronounced offshore propagation in the leeward direction tends to occur on days with a weak, offshore prevailing wind. Strong background winds, particularly in the onshore direction, are associated with a suppressed diurnal cycle. Idealized high resolution 2-D Cloud Model 1 (CM1) simulations test the dependence of the diurnal cycle on environmental wind speed and direction by nudging the model base-state toward to composite profiles derived from the reanalysis zonal wind index. These simulations can qualitatively replicate the observed development, strength, and offshore propagation of diurnally generated convection under varying wind regimes. Under strong background winds, the land-sea contrast is reduced, which leads to a substantial reduction in the strength of the sea-breeze circulation and precipitation diurnal cycle. Weak offshore prevailing winds favor a strong diurnal cycle and offshore leeward propagation, with the direction of propagation highly sensitive to the background wind in the lower free troposphere. Offshore propagation speed appears consistent with density current theory rather than a direct coupling to a single gravity wave mode, though several gravity wave modes apparent in the model likely contribute to a destabilization of the offshore environment.

In part three, the hypotheses developed in parts one and two regarding the mechanisms regulating the diurnal cycle response are rigorously tested. A novel probabilistic framework is applied to the Luzon test case to improve the understanding of diurnal cycle variability. High amplitude diurnal cycle days tend to occur with weak to moderate offshore low-level wind and near to above average column moisture in the local environment. The transition from the BSISO suppressed phase to the active phase is most likely to produce the wind and moisture conditions supportive of a substantial diurnal cycle over western Luzon and the South China Sea (SCS). Thus, the impact of the BSISO on the local diurnal cycle can be understood in terms of the change in the probability of favorable environmental conditions. Idealized high-resolution 3-D Cloud Model 1 (CM1) simulations driven only by a base-state derived from BSISO composite profiles are able to reproduce several important features of the observed diurnal cycle variability with BSISO phase, including the strong, land-based diurnal cycle and offshore propagation in the transition phases. Background

wind appears to be the primary variable controlling the diurnal cycle response, but ambient moisture distinctly reduces precipitation strength in the suppressed BSISO phase, and enhances it in the active phase. A land-breeze, lingering deep convection over land after sunset, and strong mechanical convergence appear to all be required in order to produce offshore propagation in CM1. Simulations in which the diurnal cycle of insolation is removed suggest the potential for a natural timescale for convective regeneration related to the island size.

## ACKNOWLEDGEMENTS

I first want to thank my advisor, Prof. Eric Maloney for his support through difficult times and personal challenges, as well as his steady advice, and the professional opportunities he has given me. My committee members, Profs. Michael Bell, Dave Randall, and Jeff Niemann, also provided invaluable feedback through the duration of my time in graduate school. The time they have dedicated to my success is greatly appreciated. I would also like to thank Prof. Susan van den Heever, Dr. Leah Grant, and Prof. Russ Schumacher at Colorado State University for their helpful advice and guidance in designing and running the model experiments. This work was supported by the Office of Naval Research (ONR) under the Propagation of Tropical Intraseasonal Oscillations (PISTON) project N00014-16-1-3087, the NOAA CVP program under grant NA18OAR4310299, NASA CYGNSS grant 80NSSC21K1004, and the Climate and Large Scale Dynamics Program of the National Science Foundation under grant AGS-1735978.

## TABLE OF CONTENTS

ABSTRACT . . . . .	ii
ACKNOWLEDGEMENTS . . . . .	v
LIST OF TABLES . . . . .	viii
LIST OF FIGURES . . . . .	ix
Chapter 1    Introduction . . . . .	1
1.1        Large-Scale Modes of Tropical Convective Variability . . . . .	2
1.2        Diurnal Cycle Variability . . . . .	4
1.3        Scope and Significance of This Work . . . . .	5
Chapter 2    The Quasi-Biweekly Oscillation and the Philippines Diurnal Cycle . . . . .	8
2.1        Introduction . . . . .	8
2.2        Data and Methods . . . . .	10
2.2.1    Data Description . . . . .	10
2.2.2    Methods . . . . .	11
2.2.3    QBWO Index . . . . .	13
2.3        Results . . . . .	19
2.3.1    2018 PISTON Case Study . . . . .	19
2.3.2    Large Scale . . . . .	24
2.3.3    Luzon . . . . .	30
2.3.4    Mindanao . . . . .	34
2.4        Discussion . . . . .	37
2.4.1    Overview . . . . .	37
2.4.2    QBWO and BSISO Similarities . . . . .	40
2.4.3    QBWO and BSISO Differences . . . . .	41
2.5        Conclusions . . . . .	42
Chapter 3    The Tropical Diurnal Cycle Under Varying States of the Monsoonal Back- ground Wind . . . . .	46
3.1        Introduction . . . . .	46
3.2        Data and Methods . . . . .	49
3.2.1    Observations . . . . .	49
3.2.2    Binning Method . . . . .	49
3.2.3    CM1 Setup . . . . .	52
3.3        Observations . . . . .	55
3.3.1    Daily Mean . . . . .	55
3.3.2    Diurnal Cycle . . . . .	57
3.4        CM1 Experiments . . . . .	61
3.4.1    Simulation Overview . . . . .	61
3.4.2    Land-Sea-Breeze Circulation . . . . .	64
3.4.3    Gravity Waves . . . . .	68

3.4.4	Direction of Propagation Sensitivity Experiments . . . . .	74
3.5	Conclusions . . . . .	78
Chapter 4	The Mechanisms Involved in the Modulation of the Tropical Island Diurnal Cycle by the Boreal Summer Intraseasonal Oscillation . . . . .	83
4.1	Introduction . . . . .	83
4.2	Data and Methods . . . . .	84
4.2.1	Observations . . . . .	84
4.2.2	CM1 Setup . . . . .	85
4.3	Observations . . . . .	91
4.4	CM1 Experiments . . . . .	104
4.4.1	Control Experiments . . . . .	105
4.4.2	Sensitivity Experiments . . . . .	108
4.4.3	Impacts of Island Size and Diurnal Variation . . . . .	116
4.5	Conclusions . . . . .	124
Chapter 5	Conclusions . . . . .	127

## LIST OF TABLES

4.1	Summary of CM1 simulations examined in this study. . . . .	91
-----	--	----

## LIST OF FIGURES

2.1	NOAA ETOPO2 Topography (in meters) over the Philippines, with boxes of spatial averaging and important geographic features noted. The track of the R/V Thomas G. Thompson during the August-October 2018 PISTON field campaign is also shown in purple, with August in the darkest color and October in the lightest. . . . .	12
2.2	(a) Power spectrum of ERA5 850-mb zonal wind averaged inside box L in Fig. 2.1 during June-September (JJAS) 1998-2020 (blue), with theoretical red noise spectrum (red; Gilman et al. 1963), and its 90% confidence bound calculated with an F-test (gray, dotted). (b) As in (a) but for Mindanao, averaged inside box M. . . . .	15
2.3	Spatial pattern at -4 (top), -2 (middle), and 0-day (bottom) lags from extended EOFs 1 (left) and 2 (right) of 10-20 day bandpass filtered AVHRR OLR anomalies in physical units ( $W m^{-2}$ ). The bottom row shows the difference between power spectra of each corresponding principal component time series and the corresponding 90% confidence bound of a theoretical red noise spectrum with the same autocorrelation as the PC time series. Values above zero (dotted red line) can be considered statistically significant at the 90% confidence level. . . . .	17
2.4	Number of days in a certain Lee et al. (2013) BSISO phase distributed by active QBWO phase. The BSISO is considered to be inactive when the amplitude of the index is less than one. The darker color in the stacked bar chart indicates days that are classified as the same phase number in both indices. . . . .	18
2.5	Time-height diagram of zonal wind from each sounding taken as part of the PISTON field campaign between 14 August 2018 and 13 October 2018. Soundings were taken every 12 hours from the island of Yap (top) and every 3 hours from the R/V Thomas G. Thompson during operational periods (bottom). . . . .	20
2.6	Hovmöller plot of AVHRR OLR averaged between 0 and 25N at each longitude during 1 June-20 October 2018, bandpass filtered to the 10-20 day timescale using a Lanczos filter with 93 weights in $W m^{-2}$ (left), and OLR anomalies from the seasonal cycle defined by the average daily climatology smoothed with a 7-day running mean (right). Named tropical cyclone tracks from IBTrACS are superimposed with gray dotted lines when the storm center was inside 0-25N. . . . .	22
2.7	Phase space diagram of the QBWO index activity from 14 August-14 October 2018 (the PISTON field campaign period), with the first principal component on the y-axis and the second principal component on the x-axis. The split between the 8 phases is denoted with black dotted lines, while days with an amplitude less than 1 (inside the center circle) are considered inactive, and not part of any phase. August is shown in the darkest color, with October in the lightest pink. The corresponding numbers indicate the date of each month. . . . .	23

2.8	(a) CMORPH precipitation rate estimates (mm/hr) averaged from 6N-8N across Mindanao (Box M, Fig. 2.1) from 11 September 2018 to 23 September 2018, during one full cycle of the QBWO index. The average topography in this box from NOAA ETOPO2 is shown on the bottom, with the coastlines drawn as vertical dashed black lines. Note that there are some land points west of the western coastline here, part of the Zamboanga Peninsula. The horizontal dashed black lines correspond to 00 UTC, or 0800 local time. (b) Zonal wind at 850-hPa averaged across both latitude and longitude in Box M (red line) and total column water vapor (blue line) from ERA5, with the JJAS composite diurnal cycle removed at each hour. . . . .	25
2.9	Composite maps by select QBWO phase over the West Pacific ocean of anomalies of OLR ( $W m^{-2}$ ) and vector anomalies of 850-mb wind from ERA5 (left column), and anomalies of ERA5 total column water vapor ( $kg m^{-2}$ ) with total 850-mb vector wind (right column). The total number of days in each composite can be ascertained from Figure 2.4 . . . . .	27
2.10	Anomalies in daily mean CMORPH precipitation rate composited by QBWO phase, with statistical significance at the 95% confidence level shown as dots. . . . .	28
2.11	Anomalies in the amplitude of the CMORPH precipitation rate diurnal cycle by QBWO phase. Anomalies are calculated as the difference in diurnal amplitude between each phase composite, and amplitude of the JJAS composite diurnal cycle. Statistical significance at the 95% confidence level is shown as dots. . . . .	29
2.12	Hovmöller diagrams of the composite diurnal cycle of CMORPH precipitation rate (mm/day) for select phases of the QBWO index. Precipitation rates are averaged across latitude in box L (Fig. 2.1), with corresponding longitude noted below. The average elevation of topography from NOAA ETOPO2 inside box L is shown at the bottom for reference. . . . .	31
2.13	(a-c) Composites of the spatially averaged diurnal cycle of CMORPH precipitation rate (mm/day) in the QBWO (solid) and Lee et al. (2013) BSISO (dotted) phase with the highest diurnal range (orange), the QBWO/BSISO phase with the smallest diurnal range (blue), and the full JJAS composite (dotted black). Spatial averaging is done over ocean points inside box A (a), and land points inside boxes B (b) and C (c). (d-f) The corresponding daily mean precipitation (blue) and diurnal range (red) in mm/day of each phase's spatially averaged composite diurnal cycle, by QBWO phase (solid) and BSISO phase (dotted). Each box covers a domain near Luzon. . . . .	33
2.14	(a-c) Composites of the spatially averaged diurnal cycle of CMORPH precipitation rate (mm/day) in the QBWO (solid) and Lee et al. (2013) BSISO (dotted) phase with the highest diurnal range (orange), the QBWO/BSISO phase with the smallest diurnal range (blue), and the full JJAS composite (dotted black). Spatial averaging is done over ocean points inside box D (a), and land points inside boxes E (b) and F (c). (d-f) The corresponding daily mean precipitation (blue) and diurnal range (red) in mm/day of each phase's spatially averaged composite diurnal cycle, by QBWO phase (solid) and BSISO phase (dotted). As in Fig. 2.13 but for Mindanao. . . . .	36

2.15	Daily mean values of select variables from ERA5 composited by QBWO phase (solid, orange) and BSISO phase (dotted, blue), averaged over box L covering Luzon (left) and box M covering Mindanao (right). Total column water vapor ( $\text{kg m}^{-2}$ ) is shown on top (a, d), downwelling shortwave radiation ( $\text{W m}^{-2}$ ) at the surface in the middle row (b, e), and 850-hPa zonal wind ( $\text{m s}^{-2}$ ) at the bottom (c, f). Corresponding JJAS mean values for each variable on each island are shown as a horizontal dotted black line. . . . .	38
2.16	Daily mean anomalies from JJAS average of select variables from ERA5 composited by QBWO phase (top) and BSISO phase (bottom) over the Philippines. For each variables, phase 3 of each index is shown at the left, and phase 7 at the right. The grouping of 4 panels at the left shows total column water vapor ( $\text{kg m}^{-2}$ ), the middle grouping shows downwelling shortwave radiation ( $\text{W m}^{-2}$ ) at the surface, and the right grouping shows 850-hPa zonal wind ( $\text{m s}^{-2}$ ). . . . .	39
3.1	(a) NOAA ETOPO2 Topography (in meters) over the northern Philippines, with boxes of spatial averaging and important geographic features noted. (b) Structure of the first EOF of ERA5 zonal wind averaged in JJAS 1979-2020 inside Box A of (a), in m/s, by pressure level (hPa). (c) Normalized power spectrum of the principal component (PC) time series corresponding to the EOF in (b) in blue, with a theoretical red noise spectrum based on a time series with the same autocorrelation as the PC time series shown in dotted red. . . . .	50
3.2	(a) Composite ERA5 zonal wind profiles (m/s) for all JJAS 1998-2020 days that fall in a certain bin of the PC time series of the EOF in Fig. 3.1b. Values are averaged inside Box A (Fig. 3.1a). Bins include $0.25\sigma$ on either side of the value noted. That is, $+0.5\sigma$ days include any day between $0.25$ and $0.75\sigma$ . The minimum and maximum bins are unbounded. (b) Anomalous moisture profiles in g/kg for the same bins noted in (a). (c) The number of JJAS 1998-2020 days that fall into each bin is shown as bars, with this number noted on top. The second number after the slash indicates the number of days in which a tropical cyclone center was near Luzon (inside 10-22N, 115-127E). Color coding is based on zonal wind, with easterly low-level wind bins shown in blues, and westerly bins shown in reds. . . . .	53
3.3	Daily mean precipitation anomaly (mm/day) from CMORPH (JJAS, 1998-2020) averaged by bins of zonal wind EOF index. Anomalies are from the average precipitation rate on all JJAS days. Increasing zonal wind rotates clockwise around the figure. The $\pm 2\sigma$ bins are not shown due to heavy tropical cyclone influence. . . . .	56
3.4	Anomaly in the diurnal cycle amplitude (defined by the first harmonic of the composite diurnal cycle) composited by bin of the zonal wind EOF index for JJAS 1998-2020. Anomalies are from the amplitude of the full JJAS composite diurnal cycle. Increasing zonal wind rotates clockwise around the figure. The $\pm 2\sigma$ bins are not shown due to heavy tropical cyclone influence. . . . .	58

3.5	Hovmöller diagrams of CMORPH composite precipitation rate (mm/day) on days binned by zonal wind EOF index averaged across latitude inside Box L (Fig. 3.1a). Time starts at 08:00 local time in each panel, and increases downward. Dotted lines are estimates for a line of best fit between 16:00 and 01:00 of the longitude with the maximum precipitation rate at each time. This calculation only includes longitudes on the side of the island (east or west) that contains the maximum precipitation rate at 16:00. The estimated speed of propagation following this line of best fit is noted in the legend for each panel. This is not shown for the $+1.5\sigma$ bin since little offshore propagation can be discerned. Increasing zonal wind rotates clockwise around the figure, with the composite 850-hPa zonal wind shown as a vector in each panel. The $\pm 2\sigma$ bins are not shown due to heavy tropical cyclone influence. . . . .	59
3.6	Precipitation rate (mm/hr) for the full 14-day simulation of select Cloud Model 1 (CM1) experiments. The x-axis in each is in km, with the coastlines marked as vertical dotted black lines. 05:00 on each day is noted as a horizontal dotted black line. The base-state 850-hPa zonal wind is shown as a labelled vector in each panel. . . . .	62
3.7	Daily composite of the 14-day CM1 simulations showing precipitation rate by longitude at 1-km resolution. Each simulation varies the base state with the wind and moisture profile bins shown in Fig. 3.2 (as well as surface variables and thermal profiles, which are not shown). Dotted gray lines note the coastlines, and the dotted black line follows a line of best fit connecting the longitude of maximum precipitation rate at each time between 20:00 and 08:00. This is calculated based on precipitation rate smoothed to 8-km resolution. Increasing zonal wind in the base state rotates clockwise around the figure, with the base-state 850-hPa zonal wind shown as a labelled vector in each panel. . . . .	63
3.8	Lowest model level zonal wind (in m/s) Hovmöller diagrams for select experiments. The total zonal wind is shown on the top, and the perturbation from the base-state is shown on the bottom. The line of best fit for the maximum precipitation rate shown in Fig. 3.7 for the corresponding experiment is shown as a dotted black line. Coastlines are denoted with dotted gray lines. The base-state 850-hPa zonal wind is shown as a labelled vector in each panel in the top row. . . . .	66
3.9	(a) Diagnosed 2-m temperature (C) for each experiment averaged for each time across the western half of the island. (b) As in (a), except averaged over the eastern half of the island. (c) Onshore (i.e. westerly positive) perturbation zonal wind (m/s) at the lowest model level (25m) for each experiment averaged for each time between the western coast and 25-km offshore. (d) As in (c), except with easterly winds defined as positive, averaged between the eastern coast and 25-km offshore. . . . .	67
3.10	14-Day composite of perturbation potential temperature in colors, and total cloud mixing ratio (liquid+ice) contoured starting at 0.005 g/kg, then 0.02 g/kg and every 0.02 g/kg thereafter to 0.1 g/kg. Each variable is averaged over (a) the western half of the island for the $-1.0\sigma$ experiment, (b) the eastern half of the island for the $+0.0\sigma$ experiment, and (c) the eastern half of the island for the $-1.0\sigma$ experiment. Local time starts at 08:00 and increases to the right, with height in kilometers on the y-axis. . . . .	69

3.11	Perturbation potential temperature (K) for the second day of the $0.0\sigma$ experiment in color at (a) 2.0-km, (b) 4.0-km, (c) 6.4-km, and (d) 9.1-km. The black contour indicates 2 mm/hr precipitation rate on Day 2 and is the same in all panels. The base-state 850-hPa zonal wind is shown as a labelled vector in (a). . . . .	70
3.12	14-Day composites from the $-1.0\sigma$ experiment (left), the $0.0\sigma$ experiment (middle), and the $+1.0\sigma$ experiment(right) showing Hovmöller diagrams of convective available potential energy (CAPE, J/kg; top), convective inhibition (CIN, J/kg; middle), and the level of free convection (LFC, m; bottom), with local time starting at 08:00 increasing downwards. The line of best fit for the maximum precipitation rate shown in Fig. 3.7 for the corresponding experiment is shown as a dotted white line. The base-state 850-hPa zonal wind is shown as a labelled vector in each panel in the top row. . . . .	72
3.13	14-day composite CAPE (a; J/kg), CIN (b; J/kg), and LFC (c; m) averaged across the nearest 100-km of coastal waters on the eastern side of the simulated island in red, with composite precipitation rate (mm/hr) averaged in the same region in blue. . . . .	73
3.14	(a) Idealized base-state zonal wind profiles in the lower troposphere for sensitivity experiments set 1, based on linear interpolation between the $-0.5\sigma$ and $+0.0\sigma$ experiments shown in Fig. 3.2a. (b) As in (a) but for sensitivity experiments set 2, which are taken from set 1, but forced to a line (in pressure-wind coordinates) connecting a wind of -1 m/s at 1000-hPa and 0 m/s at 900-hPa if the set 1 profile is more westerly than the ideal line profile at a given height. (c) As in (a) but for sensitivity experiments set 3, which are interpolated between the $-1.0\sigma$ and $0.0\sigma$ experiments, with the shear profile between 800-hPa and 850-hPa extended to the surface. Profiles are color coded by the propagation velocity of the smoothed (to 5-km spacing) maximum precipitation rate between 20:00 and 08:00 in each experiment, with red indicating eastward propagation, and blue indicating westward propagation. The gray profiles are chosen subjectively as experiments with weak or inconsistent offshore propagation in which the objective algorithm to calculate propagation speed failed. . . . .	75
3.15	(a) Zonal wind profiles averaged from 17:00-20:00 within 25-km of the average location of maximum precipitation between 17:00 and 20:00 in the composite, for sensitivity experiments set 1. (b) As in (a) but for sensitivity experiments set 2. (c) As in (a) but for sensitivity experiments set 3. Profiles are color coded by the propagation velocity of the smoothed (to 5-km spacing) maximum precipitation rate between 20:00 and 08:00 in each experiment, with red indicating eastward propagation, and blue indicating westward propagation. The gray profiles are chosen subjectively as experiments with weak or inconsistent offshore propagation in which the objective algorithm to calculate propagation speed failed. . . . .	77
3.16	The average longitudinal position of the maximum precipitation rate (after smoothing to 5-km spacing) between 17:00 and 20:00 is shown on the x-axis (in kilometers), with the base-state zonal wind (in m/s) at the 0.68-km above the surface on the y-axis. Dotted black lines indicate the center of the island (vertical) and 0 m/s (horizontal). The dots are color-coded by experiment set, with Set 1 in red, Set 2 in black, and Set 3 in blue. . . . .	79
4.1	(a) NOAA ETOPO2 Topography (in meters) over the northern Philippines, overlaid with boxes of spatial averaging used in this study. . . . .	86

4.2	(a) Composite ERA5 zonal wind profiles (m/s) for each BSISO Phase in JJAS 1998-2020. Values are averaged inside Boxes A-F together (Fig. 4.1a). (b) Anomalous moisture profiles in g/kg by BSISO Phase. (c) The number of JJAS 1998-2020 days that fall into each bin is shown as bars, with this number noted on top. . . . .	88
4.3	Hovmöller diagrams of CMORPH composite precipitation rate (mm/day) on JJAS days by Lee et al. (2013) BSISO index. Results are averaged across latitude inside Boxes A-F (Fig. 4.1a), but additional longitude to the west of Box A and the east of Box B is also included. Time starts at 08:00 local time in each panel, and increases downward. Vertical dotted lines show the position of each coastline. The average topography from NOAA ETOPO2 inside boxes A-F is shown at the bottom for reference.	93
4.4	The composite diurnal cycle of CMORPH precipitation (mm/day) averaged inside each box on all JJAS 1998-2020 days in Fig. 4.1 (blue line). The composite diurnal cycle only from days on which the amplitude of the diurnal cycle (as defined by the difference between daily maximum precipitation and daily minimum precipitation rate) is greater than its 85th percentile (red line). A histogram showing the number of days on which the maximum precipitation rate occurs in each half-hour bin (gray). The first (23:30-00:00 UTC or 07:30-08:00 Local Time) and last (00:00-00:30 UTC or 08:00-08:30 Local Time) bins are excluded since those bins capture days on which precipitation is either increasing or decreasing through the whole day due to longer time-scale features. The top row shows Boxes C-E, which include mainly land points, while the bottom row shows Boxes A, B, and F, which include mainly oceanic points. .	94
4.5	The relative change in the probability of an 85th percentile diurnal cycle amplitude day occurring in each box from Fig. 4.1 given a specific BSISO phase (y-axis). For example, if 30% of BSISO Phase X days showed a 85th percentile diurnal cycle amplitude in Box Y, it would display as a 100% increase, since 15% of all days can be expected to exceed the 85th percentile. . . . .	96
4.6	In gray, histograms of the daily spatial average value inside Boxes A-F (Fig. 4.1) of ERA5 06:00-12:00 Local Time surface shortwave radiation ( $W/m^2$ ; top row), total column water vapor ( $kg/m^2$ ; middle row), and 850-hPa Zonal Wind (m/s; bottom row), for . The histogram in color is the histogram of the same variables, but only for days in which the diurnal cycle amplitude exceeded its 85th percentile over the coastal South China Sea (Box B in Fig. 4.1; left column), and the east coast of Luzon (Box E in Fig. 4.1; right column). Binned ERA5 variables still come from Boxes A-F together, but the diurnal cycle inside each sub-box determines the days from which to derive the distribution. . . . .	97

4.7	In contours, the 2-D histogram by bins of ERA5 850-hPa Zonal Wind averaged in Boxes A-F together (Fig. 4.1 on the x-axis (m/s), and ERA5 total column water vapor ( $\text{kg/m}^2$ ) averaged in Boxes A-F on the y-axis, and is the same in each panel. There are 20 total bins in both the zonal wind and total column water vapor distributed evenly between their respective maximum and minimum values. Contours are located every 12 days, with the innermost contour indicating 84 days. 2806 total days are used from JJAS 1998-2020 in this analysis. Colors indicate the anomalies in the histogram (of values for Boxes A-F together) given that an 85th percentile diurnal cycle amplitude day occurred in one of the 6 boxes A-F, and varies by panel. Values are scaled before calculating anomalies such that they represent the expected number of days in each 2-D bin if 2806 85th percentile days were to occur (i.e. the histogram is divided by 0.15, and then the anomaly is calculated). The top row's histograms comes from average precipitation rate Boxes C-E, which include mainly land points, while the bottom row comes from Boxes A, B, and F, which include mainly oceanic points. The vertical dotted black line indicates the JJAS mean 850-hPa Zonal Wind, while the horizontal dotted line indicates the JJAS mean total column water vapor. . . . .	99
4.8	As in Fig. 4.7 for the contours and vertical lines. Colors indicate the anomalies in the histogram given that the BSISO was active in a certain phase. Values are scaled before calculated anomalies such that they represent the expected number of days in each 2-D bin if 2806 days from each BSISO phase were to occur. For example, to display the Phase 1 anomaly, the 2-D histogram is multiplied by 2806/188 (188 is the number of BSISO Phase 1 active days shown in Fig. 4.2c in JJAS 1998-2020), and then the anomaly is calculated. . . . .	101
4.9	As in Fig. 4.3, but with the composite restricted to BSISO active days in a certain phase on which the first EOF of the Luzon vertical profile of zonal wind described in Chapter 3 was less than or equal to $-0.25\sigma$ , indicating anomalous easterly winds. The number in parentheses next to the title indicates the number of days in each composite.	102
4.10	As in Fig. 4.3, but with the composite restricted to BSISO active days in a certain phase on which the first EOF of the Luzon vertical profile of zonal wind described in Chapter 3 was greater than or equal to $+0.25\sigma$ , indicating anomalous westerly winds. The number in parentheses next to the title indicates the number of days in each composite.	103
4.11	Meridionally averaged precipitation rate (mm/hr) for the full 7-day simulation the Cloud Model 1 (CM1) control simulations with a BSISO Phase 3 base-state (a), and a BSISO Phase 7 base-state (b). The x-axis in each is in km, with the coastlines marked as vertical dotted black lines. 05:00 on each day is noted as a horizontal dotted black line. . . . .	106
4.12	Daily composite of the 7-day control CM1 simulations showing meridionally averaged precipitation rate (mm/hr) by longitude at 1-km resolution. Each simulation varies the base state with ERA5 BSISO composite profiles. The wind and moisture profiles are shown in Fig. 4.2a-b. Dotted gray lines note the coastlines, and the dotted black line follows a line of best fit connecting the longitude of maximum precipitation rate at each time between 20:00 and 08:00. This is calculated based on precipitation rate smoothed to 5-km resolution. . . . .	107

4.13	As in Figure 4.12, but for the wind-only CM1 simulations. The base-state for these simulations uses the wind profile from each BSISO phase composite (shown in Fig. 4.2a), and the JJAS mean profile for the moisture and temperature. . . . .	110
4.14	(a) CM1 precipitation rate (mm/day) averaged over land for each of simulations with varying BSISO composite derived base-states. Bars for the Control simulations (Fig. 4.12) are solid colors, while those for the Wind-Only simulations (Fig. 4.13) are hatched. (b) As in (a), but averaged over the ocean grid points on the leeward side of the island (west for Phases 2-5, east for others). . . . .	111
4.15	Composite precipitation rate (mm/hr) averaged over land for the moisture experiments (left), and solar experiments (right). Simulations in the top row use BSISO Phase 3 profile in the base-state, while the bottom row forces BSISO Phase 7 profile in the base-state. The moisture experiments use the BSISO profile only for the winds, the JJAS mean temperature profile, and prescribe the moisture profile. The solar experiments use the control BSISO profile in the base-state, but vary the solar constant. . . .	112
4.16	As in Fig. 4.15, but averaged over ocean on the leeward side of the island (west for Phase 3, east for Phase 7). . . . .	113
4.17	Daily composite of meridionally averaged lowest model level zonal wind (m/s) in color, with the 2 mm/hr contour of composite precipitation rate superimposed. BSISO Phase 3 base-state is used in each simulation in the top row, while BSISO phase 7 base-state is used in the bottom row. The size of the island positioned in the center of the domain is 25-km (a, f), 100-km (b, g), 200-km (c, h), 400-km (d, i), and 800-km (e, j). The 200-km simulation is identical to the control simulation in Fig. 4.11a. The domain size is 800-km for (a-c, f-g), but increases to 1600-km for (d-e, i-j). . . . .	117
4.18	Meridionally averaged precipitation rate (mm/hr) for the full 7-day Island Size experiments. BSISO Phase 3 base-state is used in each simulation. The size of the island positioned in the center of the domain is 25-km (a), 100-km (b), 200-km (c), 400-km (d), and 800-km). The 200-km simulation is identical to the control simulation in Fig. 4.11a. The domain size is 800-km for (a-c), but increases to 1600-km for (d-e). . . . .	118
4.19	Meridionally averaged precipitation rate (mm/hr) for the first 2 days of the No-Diurnal-Cycle experiments. Simulations from each of the 8 BSISO base-states are shown. The diurnal cycle is removed by fixing the solar constant at the daily mean top-of-atmosphere incident shortwave on 1 August at 17N and fixing the solar zenith angle at 0°. . . . .	120
4.20	Meridionally averaged precipitation rate (mm/hr) for the full 7-day Island Size experiments with no insolation diurnal cycle. BSISO Phase 2 base-state is used in each simulation. The size of the island positioned in the center of the domain is 25-km (a), 100-km (b), 200-km (c), 400-km (d), and 800-km). The domain size is 800-km for (a-c), but increases to 1600-km for (d-e). The diurnal cycle is removed by fixing the solar constant at the daily mean top-of-atmosphere incident shortwave on 1 August at 17N and fixing the solar zenith angle at 0°. . . . .	122
4.21	2-m Temperature (C) averaged over land points by time for the full 7-day Island Size No Diurnal Cycle Experiments. Phase 2 base-state is used for (a), while Phase 6 base-state is used for (b). Shades of orange have a larger island and domain size compared to the control. Shades of purple have a smaller island but the same domain size. . . . .	123

# Chapter 1

## Introduction

The Maritime Continent (MC) and its surrounding waters are prone to numerous types of atmospheric phenomena that make it highly vulnerable to climate risks Yusef and Francisco (2009). Variability in the diurnal cycle can be a critical factor in determining total precipitation on the islands and in coastal waters (Biasutti et al., 2012; Bergemann et al., 2015; Zhu et al., 2017). The warm sea surface temperatures (SSTs), numerous islands of varying size, and complex topography make understanding the abundant precipitation in this region a challenging problem for numerical models with global ramifications (Ramage, 1968; Neale and Slingo, 2003). The diurnal cycle is also critical for the development of extreme rainfall and the high mean-state rainfall found in coastal oceans (Ruppert and Chen, 2020). While the diurnal cycle has been extensively studied, uncertainty remains regarding its variability and response to large-scale controls.

The canonical diurnal cycle behavior over MC islands develops from convergence associated with the sea-breeze or mountain-breeze in the late morning, typically contributing maximum precipitation rates in the late afternoon and evening hours (Dai, 2001; Kikuchi and Wang, 2008). Frequently, convection will then propagate offshore during the overnight hours, leading to an overnight or morning maximum in precipitation rates over coastal oceanic regions (Yang and Slingo, 2001; Mori et al., 2004; Sakurai et al., 2005; Natoli and Maloney, 2019). Offshore propagation has been attributed to convergence associated with the land-breeze (e.g. Houze et al. 1981; Ho et al. 2008; Fujita et al. 2011), advection by the mean wind (e.g. Ichikawa and Yasunari 2006, 2008; Yanase et al. 2017), and destabilization of the offshore environment by low-level ascent initiated by gravity waves (e.g. Mapes et al. 2003; Love et al. 2011; Hassim et al. 2016; Yokoi et al. 2017). Diurnal cycle behavior and the tendency for offshore propagation varies widely from one day to the next, motivating continued research. The MC region is also influenced by numerous large-scale modes of variability from features on global, inter-annual time scales like the El Niño Southern Oscillation

(ENSO; Rauniyar and Walsh 2013) to equatorial waves on synoptic scales (Ferrett et al., 2020). Any of these can significantly affect the diurnal cycle and local precipitation (Sakaeda et al., 2020).

The monsoon is an important driver of precipitation variability that generally follows the seasonal cycle. For example, the Philippine archipelago experiences southwesterly monsoon winds during boreal summer (June-September, JJAS), which brings moisture-laden air away from the equator and delivers much of the region's annual precipitation (Moron et al., 2009; Matsumoto et al., 2020). Drier trade easterlies dominate the rest of the year, which is generally much drier (Lee et al., 2021). While the agricultural sector relies on monsoon moisture, it can also bring devastating flooding (Cruz et al., 2013). The southwest monsoon is not always consistent throughout the season. rather, it is subject to numerous active and break cycles (Annamalai and Slingo, 2001; Olaguera et al., 2020). These alternating periods of relatively enhanced activity and quiescence are modulated by several other modes of intraseasonal variability in the tropics.

## **1.1 Large-Scale Modes of Tropical Convective Variability**

The largest source of convective variability on intraseasonal timescales in the tropics is contributed by the Madden-Julian Oscillation (MJO; Madden and Julian 1971, 1972). The MJO is an eastward-propagating area of enhanced convection in the tropical warm pool with a time-scale of 30-90 days. The active phase is characterized by strong westerly winds and abundant free-tropospheric moisture, while the suppressed phase exhibits easterly winds, a dry free-troposphere, and sunnier skies (Madden and Julian, 1994; Maloney and Hartmann, 1998; Riley et al., 2011). During boreal summer (June-September, JJAS), convection on this timescale tends to propagate northward into the Asian and West Pacific summer monsoon regions, and influence the onset of the monsoon in addition to producing active and break periods in the heart of the season (Wang and Xu, 1997; Annamalai and Slingo, 2001). This mode is often referred to as the boreal summer intraseasonal oscillation (BSISO). The MJO and BSISO can generally be considered to be the same phenomenon that exists in a different seasonal background state (e.g. Jiang et al. 2018; Wang and Sobel 2022).

As the BSISO (or MJO) can be manifest as active and break periods in the southwesterly monsoon over the SCS (Chen and Chen, 1995; Bagtasa, 2020), other modes of variability that similarly modulate the monsoonal flow over the Philippines may also impact the diurnal cycle. Differences in how another mode impacts the monsoon background may be insightful in ascertaining the primary controls on the diurnal cycle itself. Variance in boreal summer outgoing longwave radiation (OLR) shows the global maximum of the quasi-biweekly (10-20 day) time scale occurring in the South China and Philippine Seas (Qian et al., 2019). The importance of this mode in determining monsoon activity has been a subject of research for decades, first identified in the Indian monsoon region (Krishnamurti and Bhalme, 1976; Krishnamurti and Ardanuy, 1980; Chen and Chen, 1993), before being later explored in the west Pacific and east Asian monsoon regions (Chen and Chen, 1995; Chen et al., 2000).

This mode has often been described as the quasi-biweekly oscillation (QBWO), consisting of a northwestward propagating region of anomalous moisture, convection, westerly winds, and cyclonic vorticity (Kikuchi and Wang, 2009; Tao et al., 2009; Li et al., 2020). Disturbances tend to emerge in the equatorial western Pacific and propagate through the Philippine Sea, South China Sea, and into Asia, frequently impacting the Philippines (Chen and Sui, 2010; Yan et al., 2019). Many of these studies refer to the QBWO in a statistical rather than physical sense, but there is evidence that multiple phenomena can contribute to quasi-biweekly variability, and thus project onto various QBWO indices. The westward propagating mode ubiquitous in the west Pacific is often traced to a moist, R1 wave (Matsuno, 1966) that is modified by the monsoon background state (Chatterjee and Goswami, 2004). In addition to its modulation of the monsoon onset and persistence (Qian et al., 2019), the QBWO has noteworthy impacts on tropical cyclones (Zhou et al., 2018; Han et al., 2020), extreme rainfall (Liu et al., 2014), and heatwaves in China (Chen et al., 2016; Gao et al., 2018).

## 1.2 Diurnal Cycle Variability

The MJO impact on the diurnal cycle has been one of the more widely studied relationships, in part because of the potential for the diurnal cycle to feed back onto MJO propagation across the MC (Oh et al., 2013; Peatman et al., 2014; Hagos et al., 2016). However, a consensus remains out of reach, and the mechanisms involved in explaining this potential relationship are poorly understood. While oceanic precipitation generally follows the enhanced moisture of the MJO active phase, several studies have shown a relative minimum in the amplitude of the diurnal cycle and in total precipitation over land masses during the active phase of the MJO (Sui and Lau, 1992; Rauniyar and Walsh, 2011; Oh et al., 2012). Such a signal has also been observed for regions impacted by the BSISO (e.g. Chen and Takahashi 1995; Ho et al. 2008; Xu and Rutledge 2018), although a weaker diurnal cycle is still present over land during the active phase (Chudler et al., 2020). Taking a more precise view, Peatman et al. (2014) demonstrated a peak in the amplitude of the diurnal cycle in the transition from suppressed to active MJO state for several MC islands using satellite observations. Vincent and Lane (2017) identified a double-peak in the diurnal cycle amplitude as a function of MJO phase in a WRF simulation, with a secondary peak at the end of the MJO active state, but noted this was less significant in observations.

An understanding of the mechanism regulating this diurnal cycle behavior has not yet been convincingly established. Many of the above studies have attributed the enhanced diurnal cycle during the suppressed phase to the reduced cloudiness, which leads to a stronger thermal differential between the land and sea during daytime, and thus a stronger sea-breeze and stronger diurnal precipitation. This, however, would not explain the specific preference for a diurnal cycle peak near the end of the MJO suppressed period. Peatman et al. (2014) speculated that frictional moisture convergence associated with the Kelvin wave east of enhanced MJO convection (Gill, 1980) can explain this difference. Equatorial wave dynamics fall short of explaining why the strongest diurnal cycle occurs during the transition to BSISO active conditions in the northern Philippines, much further from the equator (Natoli and Maloney, 2019). Moreover, budget analyses by Lu et al. (2019) and Chen et al. (2019) found moisture convergence to be an important factor, but attributed

it to convergence of MJO-scale moisture by the local land-sea breeze circulation rather than equatorial wave dynamics. Free tropospheric moisture availability has been shown to be an important control on tropical precipitation and its diurnal cycle (Bretherton et al., 2004; Vincent and Lane, 2017). The wind profile, especially in the lower troposphere, has also been identified as an important player. Specifically, the strong winds in the MJO active phase reduce the land-sea contrast and thus daytime convection over land (Shige et al., 2017; Wang and Sobel, 2017; Wu et al., 2017, 2018; Yokoi et al., 2019). Conversely, light winds tend to favor a substantial diurnal cycle on the leeward side of islands (Virts et al., 2013; Short et al., 2019; Qian, 2020). Since MJO moisture leads the strong westerly winds in phase (Maloney and Hartmann, 1998), the arrival of increased moisture before the strong winds during the transition to active could present a compelling hypothesis explaining the preference for strong, offshore propagating diurnal cycles during these MJO phases.

### **1.3 Scope and Significance of This Work**

This dissertation aims to address several of the gaps in our knowledge regarding the tropical diurnal cycle and its variability that have not been adequately covered by the body of literature outlined above. The main goal is to understand the mechanisms regulating diurnal cycle behavior as influenced by large-scale modes of tropical convective variability. In particular, each chapter will address a part of the hypothesis stated at the end of the previous section and in Natoli and Maloney (2019). More explicitly, it is proposed that the intraseasonal variability in diurnal cycle behavior can be understood in terms of the free tropospheric moisture and background wind profiles that are favored by a certain phase of a large-scale mode of tropical convective variability, such as the MJO. In each chapter, a different perspective will be taken in the aim of examining this problem. While there will be a heavy focus on the boreal summer MJO (i.e. the BSISO) and the Philippine archipelago as a case study, it is possible that the results and conclusions can be generalized to other tropical islands in the MC.

This work is intended to provide the most clarity to date on the regulators of convective precipitation on the diurnal timescale. The varied perspectives presented in each chapter will all reinforce certain aspects of the stated hypothesis, provided a holistic view on the intraseasonal variability in tropical island diurnal cycle. An improved understanding of this relationship is important for several reasons. Most directly, due to the skill in predicting large-scale modes of convective variability such as the MJO on subseasonal timescales, a solid grasp on how this influences the local diurnal cycle on MC islands could lead to improved lead time for hydrometeorologically significant events such as flooding and drought. Additionally, while there is subseasonal prediction skill for the MJO, there is lesser skill in predicting whether the MJO convection will successfully transit the MC and progress into the west Pacific (Kerns and Chen, 2016; Kim et al., 2016). The diurnal cycle over MC islands has been identified as a potential reason for this heightened uncertainty (Hagos et al., 2016; Zhang and Ling, 2017), which suggests that improved comprehension of diurnal cycle variability could lead to improved prediction skill regarding MJO transit across the MC.

In the next chapter, the QBWO will be explored in detail to address how other modes of tropical convective variability impact the local diurnal cycle. Prior to this work, this relationship has not been studied in prior literature. The results will show that the diurnal cycle in the Philippines behaves very similarly through a QBWO event compared to a BSISO event, and that the same mechanisms proposed by Natoli and Maloney (2019) to explain the BSISO-diurnal cycle relationship can explain the QBWO-diurnal cycle relationship. This chapter has been published, with minor changes, in *Monthly Weather Review*. In Chapter 3, we take a step back from a specific large-scale mode of tropical convective variability, and explore the impact of monsoon winds on any timescale. The impact of the background wind profile on the diurnal cycle will be isolated through analysis of observations and an idealized model to show how several important aspects of diurnal cycle variability can be explained by the background wind on an individual day. This chapter, with slight modifications, has been submitted for publication in *Journal of the Atmospheric Sciences*. Our stated hypothesis will be tested most directly in Chapter 4. Through a probabilistic analysis of observational data and sensitivity tests using an idealized model, it will be shown

that the a background state of near to above average moisture and weak offshore winds leads to a strong diurnal cycle with offshore propagation into coastal waters. Certain phases of the BSISO make such conditions more likely, which is invoked to explain the observed BSISO-diurnal cycle relationship found in composites. The results of this chapter are in preparation for publication in *Journal of Climate*. Lastly, some overall conclusions, caveats, and an outline of potential avenues for future research will be discussed in Chapter 5.

## Chapter 2

# The Quasi-Biweekly Oscillation and the Philippines

## Diurnal Cycle<sup>1</sup>

### 2.1 Introduction

While the relationship between the boreal winter MJO and the tropical island diurnal cycle has received considerable scrutiny in the recent literature, the boreal summer mode (e.g. the BSISO) and its impact on landmasses in the Asian/West Pacific summer monsoon region has had much less attention. However, research surrounding the 2018 field campaign titled Propagation of Intraseasonal Tropical Oscillations (PISTON) showed that diurnal cycle variability over the Philippine archipelago can behave similarly through a BSISO event (Natoli and Maloney, 2019) compared to that over large equatorial islands such as Sumatra, Borneo, and New Guinea through an MJO event (e.g. Peatman et al. 2014; Vincent and Lane 2016). For example, the diurnal cycle in the Philippines appears to reach a maximum during the BSISO suppressed state (Ho et al., 2008; Park et al., 2011; Xu and Rutledge, 2018; Xu et al., 2021), although the typical afternoon maximum is still present in the active state (Chudler et al., 2020). Natoli and Maloney (2019) noted a maximum in the diurnal amplitude over land and coastal waters of the South China Sea (SCS) during the transition from suppressed to active BSISO state when the mid-tropospheric moisture begins to increase, but prior to the arrival of strong westerly monsoon winds.

The relationship between local precipitation and other modes of tropical variability has also been recently getting more attention. Ferrett et al. (2020) showed a significant modulation of local precipitation extremes by various types of equatorial waves. Additionally, Sakaeda et al. (2020) took a thorough look at the impact of various equatorial wave modes on the MC diurnal

---

<sup>1</sup>This chapter, as well as some text from Chapter 1, has been published in *Monthly Weather Review* with minor changes under the title “Quasi-Biweekly Extensions of the Monsoon Winds and the Philippines Diurnal Cycle”

cycle during boreal winter, noting important differences in behavior between various wave modes and individual islands. These results highlight the importance of a more local-scale approach, in particular, that the mode of variability should be considered based on its modulation of the local environmental background conditions, which then modulates the diurnal cycle. They also distinguished diurnal cycle behavior within an individual island related to the position relative to the wind (leeward vs. windward), and aspect of topography. Specifically, the diurnal cycle was found to be enhanced on the leeward side of MC islands for the MJO and  $n=1$  equatorial Rossby (R1) waves, consistent with Virts et al. (2013) and Qian (2020).

Since the monsoon system over the SCS is modulated by variability on the quasi-biweekly timescale (Chen and Chen, 1995), and significant variability on that timescale was observed during PISTON (Sobel et al., 2021), another interesting opportunity to explore diurnal cycle variability is presented. The impact of the QBWO on the diurnal cycle in the Philippines has not been explored, but recent work suggests that the same mechanisms could be at play as those important to the MJO, as well as equatorial waves. This chapter aims to explore this relationship in detail, and determine how well the ideas presented for the MJO/BSISO-diurnal cycle interaction apply to a different mode of tropical convective variability that has received less attention. Specifically, if another large-scale feature impacts the environmental background conditions (e.g. lower tropospheric wind and mid-tropospheric moisture) in a similar way to the BSISO, will the diurnal cycle respond similarly?

The first goal is to describe west Pacific variability on the 10-20 day timescale and its importance to the Philippine archipelago. This includes examination of prominent variability on this timescale that occurred during a recent major field program (Sobel et al., 2021). Second, an index for the QBWO will be described that can be used to composite precipitation and other variables. Third, we aim to establish the impact of the quasi-biweekly mode on the diurnal cycle of the Philippines and its offshore propagation. The final goal is to compare and contrast the QBWO-diurnal cycle relationship with the MJO-diurnal cycle relationship over the Philippines to help reveal important controls on diurnal convection and the mechanisms involved.

The next section will describe the data and methods used, followed by a description of the QBWO index used in this study. In Section 3, results will be discussed, starting with a case study during the 2018 PISTON field campaign, then leading into a composite analysis for the period 1998-2020 from the large scale to the island scale. Section 4 includes a discussion of the mechanisms and a comparison with the BSISO, with a summary and major conclusions for this chapter outlined in section 5.

## **2.2 Data and Methods**

### **2.2.1 Data Description**

This chapter employs several datasets to analyze quasi-biweekly variability in the monsoon and the diurnal cycle of precipitation. First, precipitation data comes from version one of the Climate Prediction Center (CPC) Morphing Technique (CMORPH; Joyce et al. 2004; Xie et al. 2017). The data is available as 30-minute total precipitation accumulation estimates at 8-km spatial resolution, covering 60°S-60°N. The CMORPH method takes precipitation rate estimates from passive microwave satellite retrievals and then uses cloud-motion vectors derived from infrared satellites to morph and interpolate through space and time to other passive microwave estimates. Thus, infrared information is only used to predict storm motion, and is not directly used to estimate precipitation rates. These initial estimates are bias-corrected against gauge data and the Global Precipitation Climatology Project (Adler et al., 2003) to yield the final product. Other studies have shown that this bias-corrected CMORPH technique removes most of the bias over land in warm climates (as in this study), and performs favorably when compared with the commonly used TRMM 3B42 precipitation dataset (Xie et al., 2017). CMORPH also demonstrates similar skill compared against the IMERG product (Huffman et al., 2015; Sahlu et al., 2016). The same analysis described below was performed for IMERG during the available period of 2000-2020 and the results remain robust.

Complementing the precipitation data, the 5th Generation Reanalysis from the European Centre for Medium-Range Weather Forecasting (ERA5; Hersbach et al. 2020; Copernicus Climate

Change Service (C3S) 2017) is used for JJAS, 1998-2020. Variables analyzed here include total column water vapor, surface downwelling shortwave radiation, and 850-hPa wind. Each of these fields are considered at 1-hour temporal resolution and  $0.25^\circ$  spatial resolution. In this study, the purpose of the ERA5 data is to contextualize the precipitation results and elucidate potential mechanisms. Additional variables were examined on numerous pressure levels through the troposphere, but these did not add further insight and are not included in this discussion.

In addition, interpolated outgoing longwave radiation (OLR) data from the Advanced Very High Resolution Radiometer (AVHRR) is analyzed at daily temporal and  $2.5^\circ$  spatial resolution for JJAS, 1979-2020 (Liebmann and Smith, 1996). OLR is used to calculate the QBWO index used in this study, as well as track large-scale convection associated with it. Zonal wind data from balloon soundings in the 2018 PISTON field campaign are also used at 3-hourly resolution from the R/V Thomas G. Thompson and 12-hourly resolution from Yap Island (Sobel et al., 2021). Processing and quality control for sounding data follows Ciesielski et al. (2014). These locations relative to the Philippines are shown in Figure 2.1. Lastly, topographic data from the National Oceanic and Atmospheric Administration's (NOAA) ETOPO2 dataset are incorporated to provide geographic context for the results (National Geophysical Data Center, 2006). The BSISO index used in this dissertation for comparison to the QBWO results is that by Lee et al. (2013), which we used in Natoli and Maloney (2019). The QBWO index used will be described below.

### **2.2.2 Methods**

The compositing method in this dissertation follows that of Natoli and Maloney (2019), in which a single composite diurnal cycle is created for CMORPH precipitation for all days in JJAS in the analysis period, defined here as the boreal summer composite diurnal cycle. In addition, separate composite diurnal cycles are created by averaging measurements from only days in that period in which an index of intraseasonal variability (e.g. QBWO or BSISO) was considered active and in a certain phase (one of eight). An anomaly in this study refers to the difference between the composite of interest and the JJAS mean. Statistical significance of the precipitation results also

## PISTON Ship Track and Philippine Geography

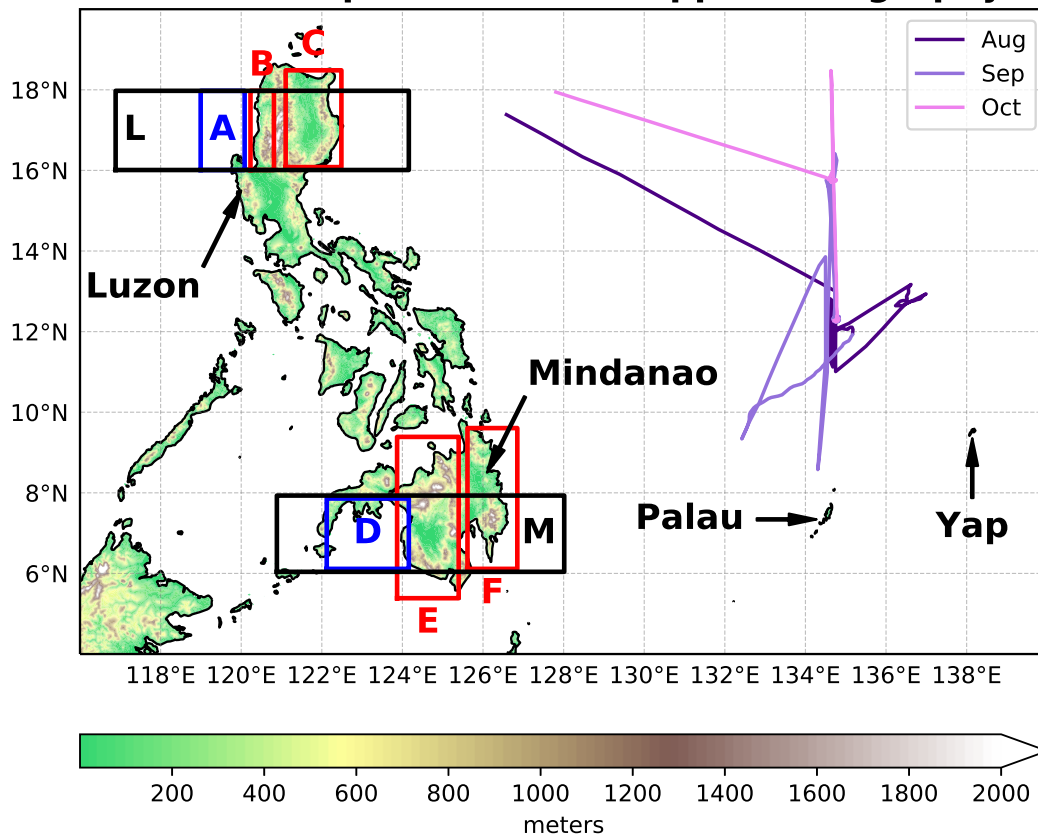


**Figure 2.1:** NOAA ETOPO2 Topography (in meters) over the Philippines, with boxes of spatial averaging and important geographic features noted. The track of the R/V Thomas G. Thompson during the August-October 2018 PISTON field campaign is also shown in purple, with August in the darkest color and October in the lightest.

follows Natoli and Maloney (2019) using a bootstrapping method, where the composite diurnal cycle in an ISO phase was compared against 1000 composite diurnal cycles taken from random days in the study period, with a Poisson distribution used to account for the fact that ISO active days tend to come in non-independent groups of several days. More details can be found in Natoli and Maloney (2019).

This study also calculates power spectra for a few different time series. This is done by calculating the spectrum for each season individually (e.g. JJAS 1998, 1999, etc.) after applying a Hanning window to reduce the Gibbs phenomenon. Then, spectra are averaged from all years to increase degrees of freedom, only considering the relevant season (boreal summer). The theoretical red noise spectra follow equation 5 of Gilman et al. (1963), which provides an estimate for how a power spectrum of a pure red noise process with the same autocorrelation as the time series of interest would appear. An F-test is employed to determine if the calculated power spectrum is significantly different from its corresponding theoretical red noise spectrum. OLR data is also bandpass filtered to 10-20 days in this study to prepare the data for calculation of the QBWO index, and highlight variability on relevant timescales for analysis of the 2018 PISTON period. This is done by applying a Lanczos filter with 93 weights to detrended OLR data at each grid point (Duchon, 1979).

### **2.2.3 QBWO Index**

An index was created to track the QBWO in the west Pacific and facilitate analysis of its relationship to the Philippine diurnal cycle. Many prior studies have created indices for this features, but a consensus has yet to emerge on the best method (Kikuchi and Wang, 2009; Han et al., 2020; Yan et al., 2019; Qian et al., 2019). The timescale studied for the QBWO also differs in the literature, but most include the 10-20 day period, with some extending to 25 or 30 days on the low frequency end, and others extending to 5 or 7 days on the high frequency end. Here, we attempt to exclude both timescales more characteristic of synoptic scale variability (5-10 days), as well as the longer time scales approaching the BSISO mode (20-30 days), and select a band of 10-20

days upon which to base our index. This timescale was found to display consistent westward propagating activity in the region of interest that also resembles the QBWO behavior documented in previous studies (Chatterjee and Goswami, 2004; Chen and Sui, 2010; Li et al., 2020). Additionally, the 10-20 day band well-captures the spectral peak in lower tropospheric wind variability near the Philippines.

Figure 2.2a shows the power spectrum calculated from 850-mb ERA5 zonal wind averaged over northern Luzon (box L in Fig. 2.1) during JJAS 1998-2020. A statistically significant spectral peak is identified around 10-15 days. This peak is robust across averaging domains that vary in both size and shape surrounding the Philippine archipelago. Thus, the 10-20 day band encompasses the spectral peak in the region of interest, produces the structure outlined in previous studies, and excludes other time scales that may muddy results (Chen and Sui, 2010; Yan et al., 2019). Fig. 2.2b shows the same for Mindanao over box M, indicating a weaker but noticeable peak in the 10-15 day band that does not reach statistical significance.

The architecture of our index is most similar to that of Qian et al. (2019), only differing in temporal and spatial domain, and filtering time scale that improve variance explained by the index. EEOFs are calculated from the 10-20 day OLR anomalies inside the domain of 0-35N, and 115-165W for JJAS 1979-2020, with information included at lags 0, 2, and 4 days prior. The spatial patterns associated with the two leading modes of variability in 10-20 day OLR are shown in Fig. 2.3, which explain 16.67% and 16.31% of the variance respectively. They are well separated from the other EOFs (not shown) and represent a propagating wave-like signal based on a lag correlation analysis of their unfiltered principal components (described below in more detail) that maximizes at 3-4 days. The coherence squared between the two PCs averaged inside the 10-20 day band is 0.81. The patterns are presented in Figure 2.3 such that time progresses going downward, and the pattern at lag 4 of EEOF 2 is roughly equivalent to the lag 0 pattern of EEOF 1. Thus, the time progression continues through EEOF 1 first, and then through the lags of EEOF 2. The spatial patterns shown here were not highly sensitive to choice of domain, filtering timescale (as long as 10-20 day band was included), lag timescale, and months analyzed. Other periods in addition to

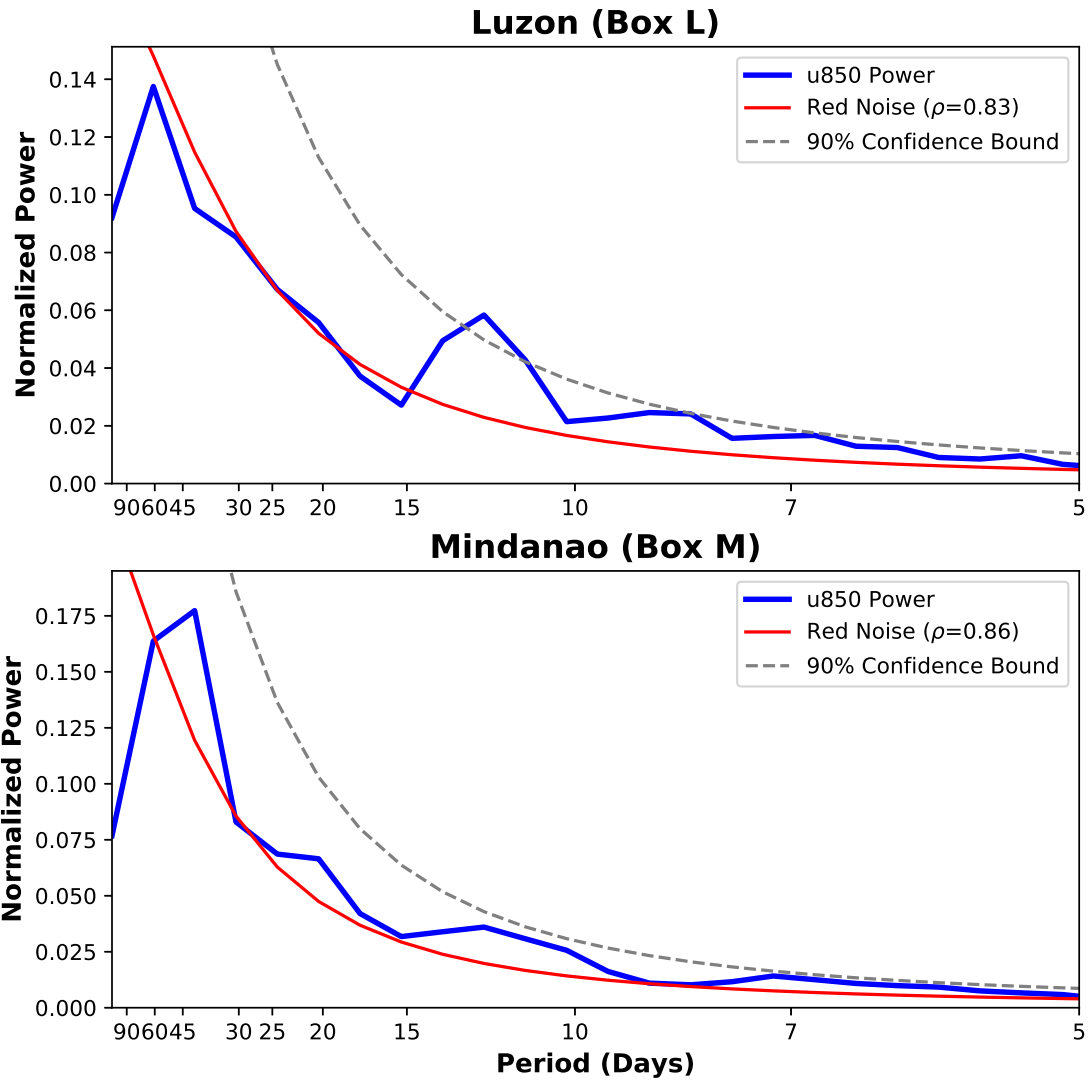


**Figure 2.2:** (a) Power spectrum of ERA5 850-mb zonal wind averaged inside box L in Fig. 2.1 during June-September (JJAS) 1998-2020 (blue), with theoretical red noise spectrum (red; Gilman et al. 1963), and its 90% confidence bound calculated with an F-test (gray, dotted). (b) As in (a) but for Mindanao, averaged inside box M.

JJAS were considered, but precipitation patterns over the northern Philippines appear somewhat distinct in May or October (not shown), which motivated the choice for the shorter season.

To calculate the principal component (PC) time series, the *unfiltered* OLR anomalies (with the seasonal cycle removed) are projected back onto the EEOF patterns in Fig. 2.3. Since unfiltered OLR anomalies make up the PCs, it must be assured that they still capture the 10-20 day timescale well, as we do allow for other time scales to project on the index. Spectra for both PC1 and PC2 (Fig. 2.3d, h) show strong, statistically significant peaks in spectral power on 10-20 day timescales. While there is some bleeding to both higher and lower frequencies, no distinct peak can be seen elsewhere in the spectrum, which provides confidence that this index is picking up westward propagating signals that oscillate on roughly 10-20 day time scales.

The use of an EEOF index also allows for more direct comparison to MJO or BSISO studies that employ the commonly-used RMM index for the MJO (Wheeler and Hendon, 2004), or the Lee et al. (2013) index for the BSISO. We can split the phase space into 8 phases according to the sign and magnitude of the corresponding PC time series for each day. Since the choices of the sign of each PC and which PC to make the x-axis or y-axis in the phase space are arbitrary, we defined them in this study such that the “active” phases for the Philippines most closely correspond to the “active” phases of the Lee et al. (2013) index for the BSISO. In other words, phases 2-4 generally correspond to suppressed convection and low-level easterly winds over Luzon for both indices, while phases 6-8 generally indicate enhanced convection and strong westerlies. This allows for the direct comparison of the precipitation behavior and background conditions over the Philippines later in this manuscript.

It is important to verify that our QBWO index is reasonably independent from the Lee et al. (2013) BSISO index before composites for each are directly compared in the subsequent sections. Fig. 2.4 shows the number of days in a certain Lee et al. (2013) BSISO phase classified by each QBWO phase. The vast majority (between 71 and 80%) of active QBWO days have an inactive BSISO, and there is no preference for a day to be classified as the same numbered phase in each index. This percentage is consistent with BSISO activity across the entire study period, as the index

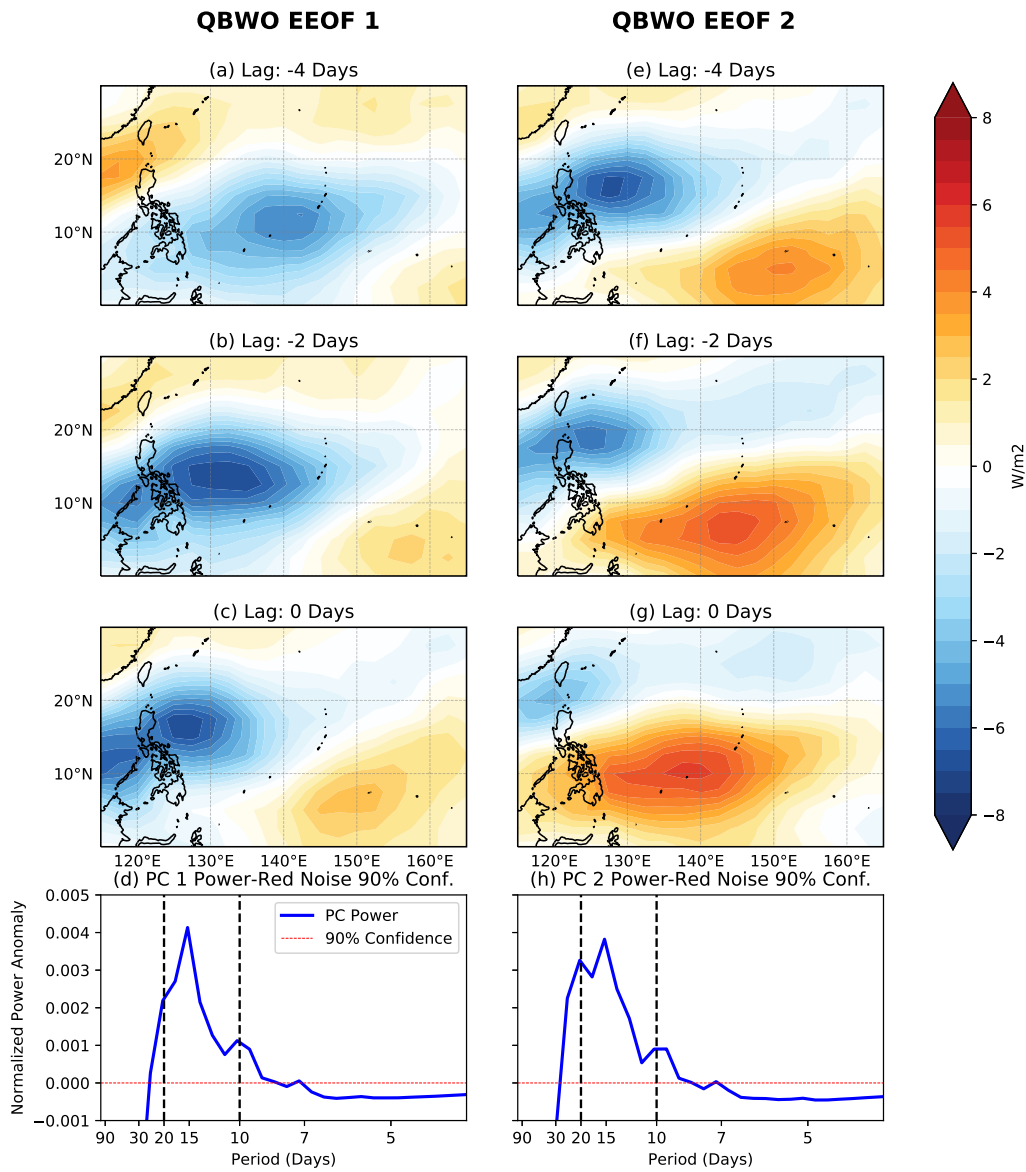


**Figure 2.3:** Spatial pattern at -4 (top), -2 (middle), and 0-day (bottom) lags from extended EOFs 1 (left) and 2 (right) of 10-20 day bandpass filtered AVHRR OLR anomalies in physical units ( $W m^{-2}$ ). The bottom row shows the difference between power spectra of each corresponding principal component time series and the corresponding 90% confidence bound of a theoretical red noise spectrum with the same autocorrelation as the PC time series. Values above zero (dotted red line) can be considered statistically significant at the 90% confidence level.

is inactive about 75% of the JJAS days between 1998 and 2020. Anti-correlation between QBWO and BSISO activity has also been found on interannual timescales (Yang et al., 2008). The third and fourth multivariate EOF identified by Lee et al. (2013), which are by definition independent from the first two EOFs which make up the BSISO index, have been shown to capture some QBWO variability (Qian et al., 2019). Thus, the QBWO index appears to be randomly selecting from BSISO activity, and we can assume that they are independent.

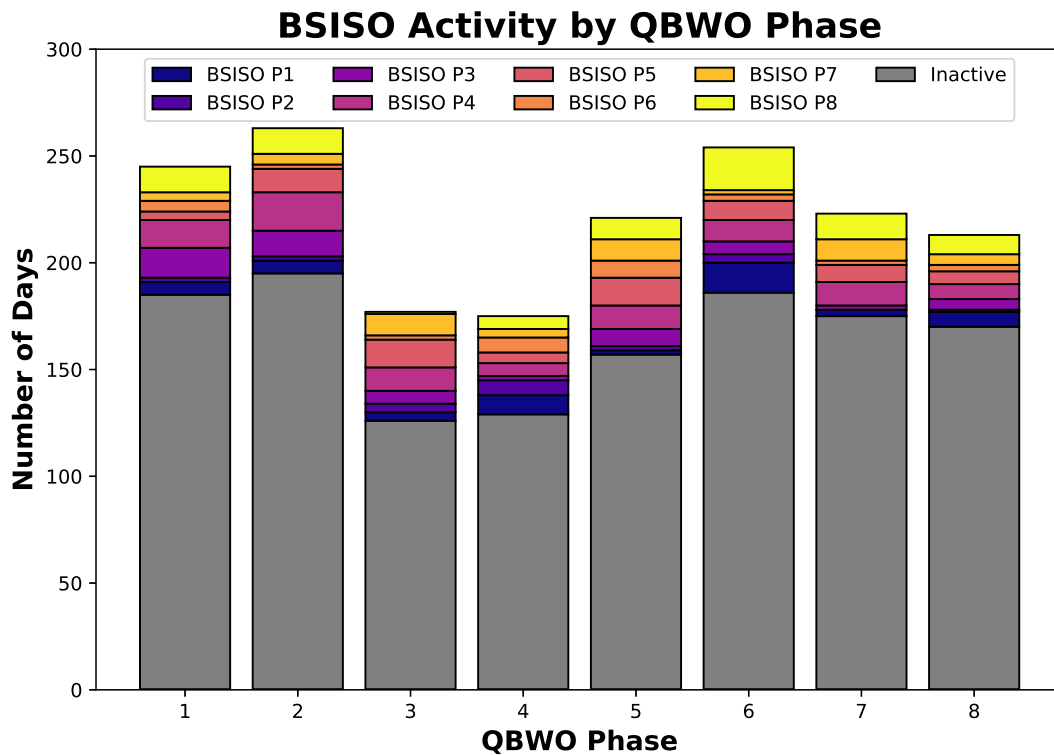


**Figure 2.4:** Number of days in a certain Lee et al. (2013) BSISO phase distributed by active QBWO phase. The BSISO is considered to be inactive when the amplitude of the index is less than one. The darker color in the stacked bar chart indicates days that are classified as the same phase number in both indices.

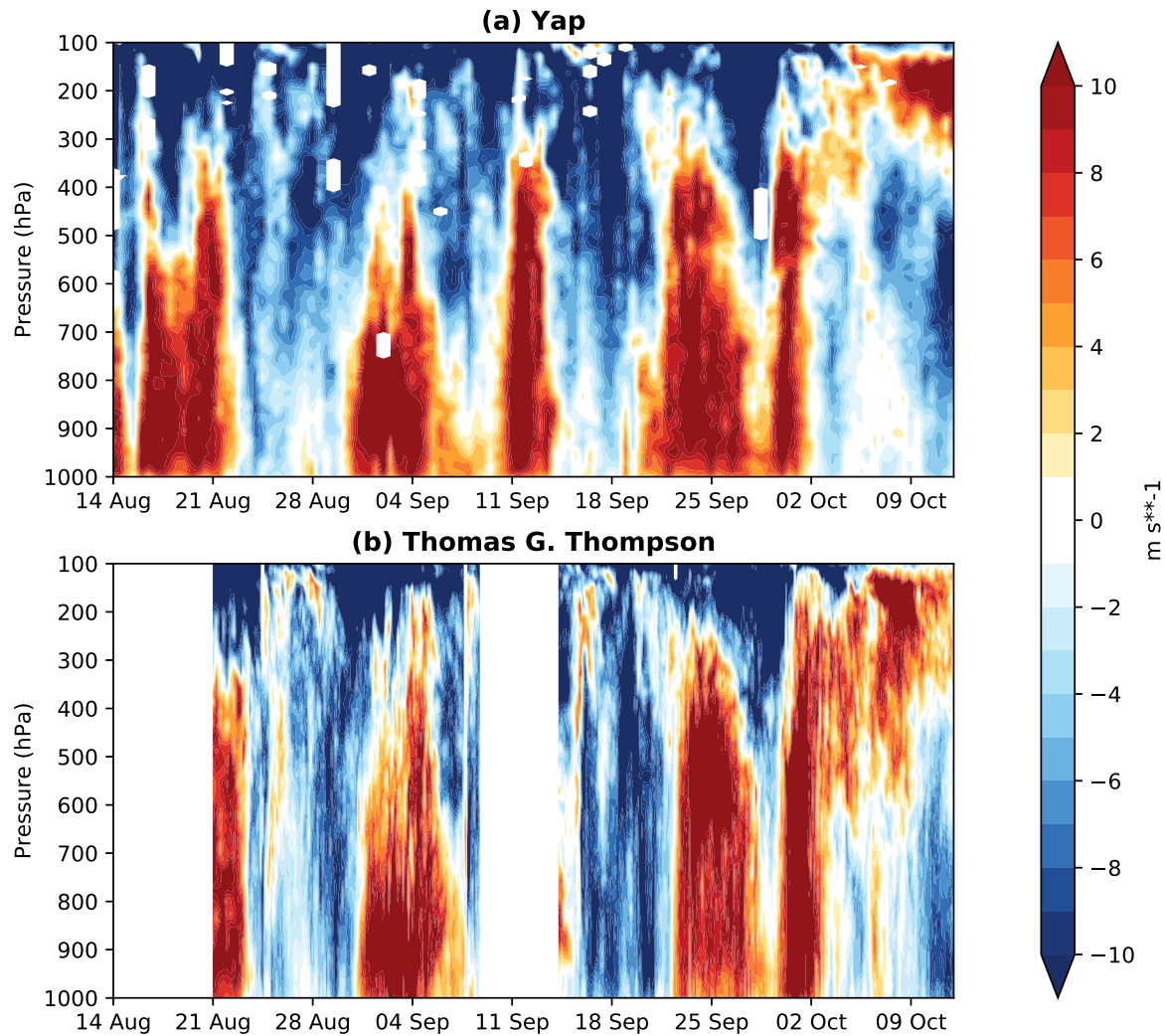
## 2.3 Results

### 2.3.1 2018 PISTON Case Study

The operational period of the 2018 PISTON field campaign (14 August - 14 October 2018) is used as a case study to assess this index and 10-20 day variability for a specific time period, before leading into a more general composite analysis in the next subsection. This time period was selected because prominent 10-20 day variability was apparent in raw data during a major field campaign (Sobel et al., 2021). One of the original goals of the 2018-19 PISTON project was to sample lower frequency intraseasonal oscillations, like the BSISO. However, the 2018 leg of the experiment witnessed minimal BSISO activity during the two month long cruise, only sampling a suppressed phase of an MJO-like disturbance in early October. While exploration of the tropical QBWO was not an original goal, the noteworthy variability observed on this timescale described below presents an opportunity to learn more about this feature (Sobel et al., 2021).

Figure 2.5 shows a time-height diagram of zonal wind observations from radiosondes released during PISTON. The top panel shows 12-hourly soundings released from the Yap island, while the bottom shows the 3-hourly soundings released aboard the R/V Thomas G. Thompson, with white space when the ship was in port or in transit (see Fig. 2.1 for locations). Both locations in the west Pacific observed significant variability in zonal wind on 10-20 day timescales. Roughly every two or three weeks, the region experienced surges of fairly strong westerly winds in the low levels, extending through much of the troposphere and lasting about 7-10 days. Westerly winds tapped into deep monsoonal flow bringing increased moisture and increased mesoscale convective system activity (Chudler and Rutledge, 2021; Sobel et al., 2021). Such monsoon surges were often caused by and/or enhanced by tropical cyclones (TCs) passing northeast of the study domain, similar to events described in Cayan et al. (2011) and Bagtasa (2017). These were interspersed with tranquil periods of weak trade easterlies. The identification of enhanced QBWO activity during the 2018 boreal summer season is consistent with prior work suggesting a preference for such activity during El Niño years (the late summer of 2018 featured a strengthening El Niño event) and during periods of decreased BSISO activity (Yang et al., 2008; Yan et al., 2019).

## PISTON 2018 Soundings of Zonal Wind



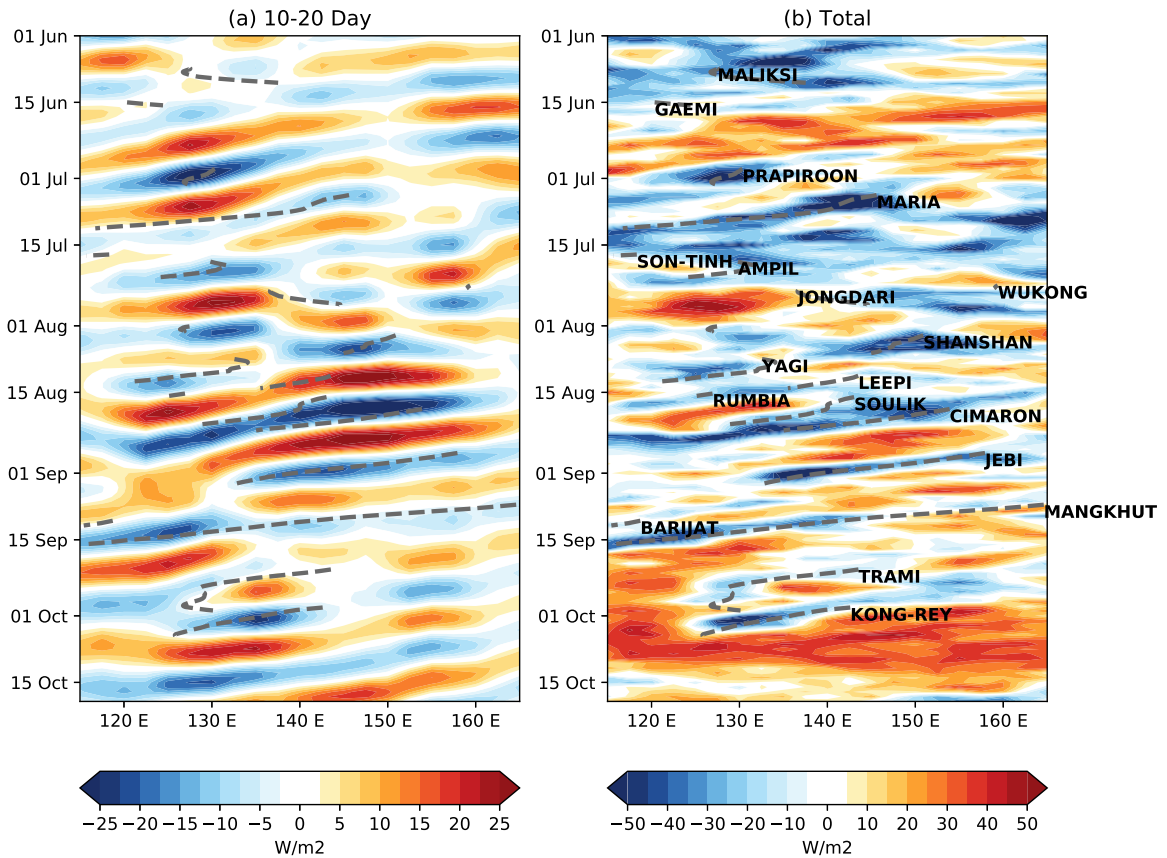
**Figure 2.5:** Time-height diagram of zonal wind from each sounding taken as part of the PISTON field campaign between 14 August 2018 and 13 October 2018. Soundings were taken every 12 hours from the island of Yap (top) and every 3 hours from the R/V Thomas G. Thompson during operational periods (bottom).

Fig. 2.6 shows both the total OLR anomalies from the seasonal cycle averaged from 0-25N, and the anomalies on the 10-20 day time scale (note the difference in color-scale) during the 2018 west Pacific monsoon season and PISTON period. Superimposed on these anomalies are the longitudinal positions of TC storm centers that entered the 0-25N latitude band during the period (Knapp et al., 2018, 2010). It can be seen that the TCs do occasionally project onto this timescale, but the 10-20 day band does include more than just propagating TCs (Ko and Hsu, 2006, 2009). 10-20 day filtered anomalies during this period are generally westward-propagating, and consistently active throughout the monsoon season. This holds true when other years are selected, but only 2018 is shown here. Thus, the 2018 field campaign observed notable 10-20 variability in lower tropospheric winds (Fig. 2.5), which corresponds to westward propagating signals in OLR when filtered to this band (Fig. 2.6).

The evolution of our QBWO index through the field campaign is shown in Figure 2.7. It can be seen that prominent 10-20 day variability consistently projected onto the index during the two month period. QBWO activity generally moved through each of the phases in order, and remained in a single phase for 1-2 days. According to this index, the strongest period of activity that progressed through a complete cycle occurred from roughly 11 September to 23 September, with days at least one day in each phase and an amplitude ( $a = \sqrt{PC1^2 + PC2^2}$ ) greater than 1.0 throughout the period.

CMORPH precipitation estimates averaged across latitude in Box M (Fig. 2.1) over Mindanao are shown for this highlighted 13-day period in Figure 2.8. Fig. 2.8b shows total column water vapor and 850-hPa zonal wind anomalies from the JJAS composite mean diurnal cycle from ERA5 averaged inside box M. Mindanao is shown here rather than Luzon because Typhoon Mangkhut made a direct landfall on 14 September. From 11 Sep to 15 Sep, Mindanao experienced strong westerly winds at 850-hPa with increased moisture. Concurrently, there was relatively little precipitation over the main island, with some heavy precipitation occurring over the Moro Gulf (Box D in Fig. 2.1) to the west. As the QBWO index moved through phases 7-8 on 15-16 September, drier conditions moved over Mindanao, and there was relatively little precipitation anywhere in

## OLR Anomalies on Various Timescales: PISTON 2018



**Figure 2.6:** Hovmöller plot of AVHRR OLR averaged between 0 and 25N at each longitude during 1 June-20 October 2018, bandpass filtered to the 10-20 day timescale using a Lanczos filter with 93 weights in  $W m^{-2}$  (left), and OLR anomalies from the seasonal cycle defined by the average daily climatology smoothed with a 7-day running mean (right). Named tropical cyclone tracks from IBTrACS are superimposed with gray dotted lines when the storm center was inside 0-25N.

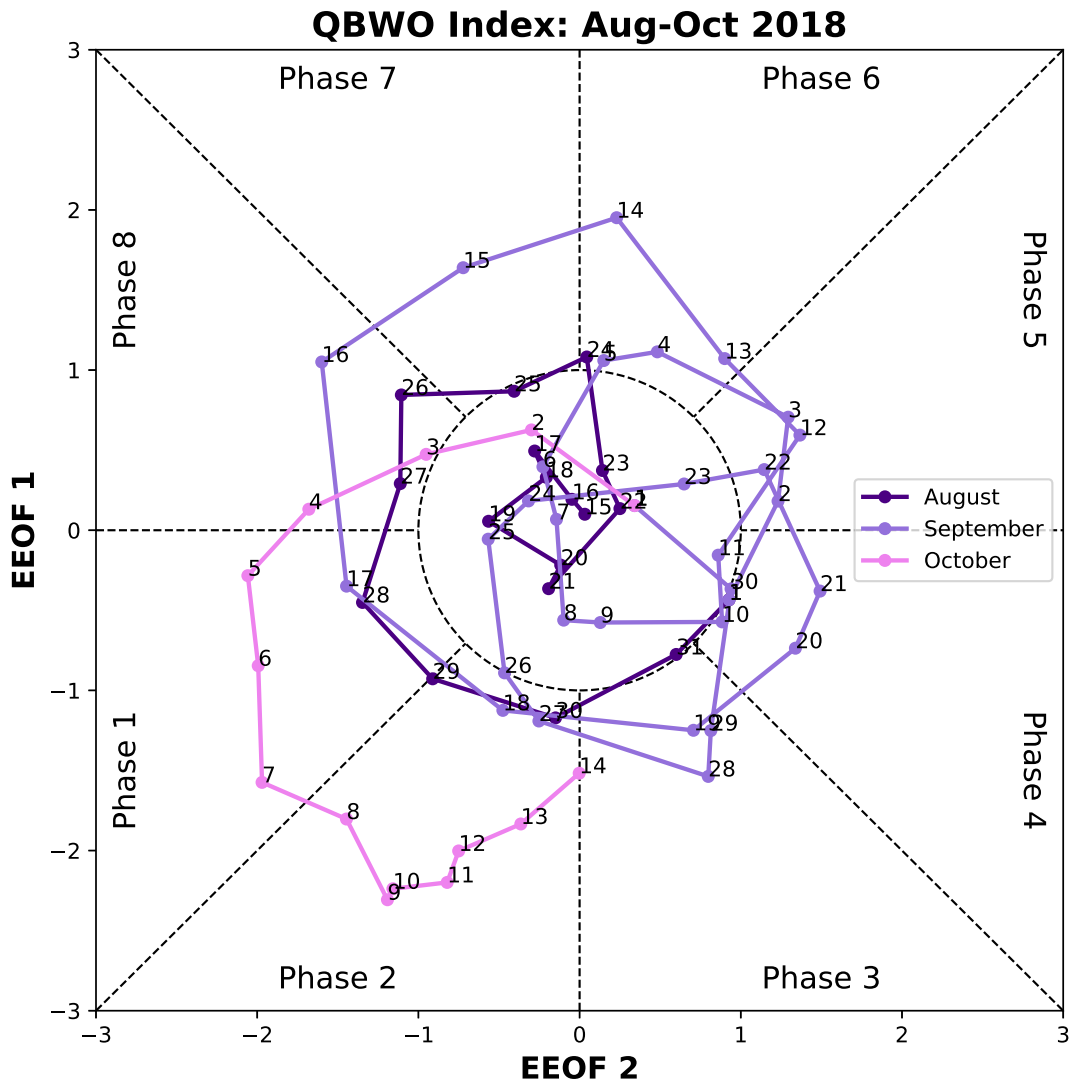


**Figure 2.7:** Phase space diagram of the QBWO index activity from 14 August-14 October 2018 (the PISTON field campaign period), with the first principal component on the y-axis and the second principal component on the x-axis. The split between the 8 phases is denoted with black dotted lines, while days with an amplitude less than 1 (inside the center circle) are considered inactive, and not part of any phase. August is shown in the darkest color, with October in the lightest pink. The corresponding numbers indicate the date of each month.

the domain. Then from 17-20 September, the main island exhibited pronounced diurnal precipitation over the high topography, with westward propagation into the evening and overnight each day (most prominent on 17 Sep). Moisture was slightly higher than normal during this period, while winds started with easterly anomalies and transitioned to westerly anomalies by the 20th.

The end of the cycle from 21-23 September, during phases 4-5 in our index, displayed markedly different diurnal precipitation behavior. With weakly positive moisture anomalies and westerly wind anomalies, the diurnal cycle was relatively inactive over the Moro Gulf and western Mindanao (although there was some nocturnal precipitation on 22 Sep in the Moro Gulf), while the eastern coastline experienced strong evening precipitation each day, with some indication of propagation to the east into the Philippine Sea. Even from a short case study, these results are consistent with other studies pointing to high moisture and offshore lower tropospheric wind as environmental background conditions favoring a strong diurnal cycle, which here is related to 10-20 day variability (Vincent and Lane, 2017; Natoli and Maloney, 2019; Sakaeda et al., 2020; Peatman et al., 2021).

The PISTON period is used in this study to show that 10-20 variability and its impact on the diurnal cycle can show up in raw data during a major field campaign and test our index during a real event. However, a two month period is not sufficient to draw robust conclusions. Thus, we will discuss a composite analysis based on the index described above in the following sections.

### **2.3.2 Large Scale**

Variables are composited by each of the 8 phases of this index, with days on which the index amplitude is less than 1 excluded. The total number of days included in each composite can be found in Fig. 2.4. Figure 2.9 shows the large scale structure of the QBWO as captured by this index, with every other phase shown. Daily unfiltered OLR anomalies with ERA5 850-hPa vector wind anomalies superimposed are shown on the left, with ERA5 total column water vapor anomalies and total wind (not anomalies) on the right. The index captures the northwestward propagation of alternating zones of suppressed and enhanced convection, associated with anti-cyclonic and

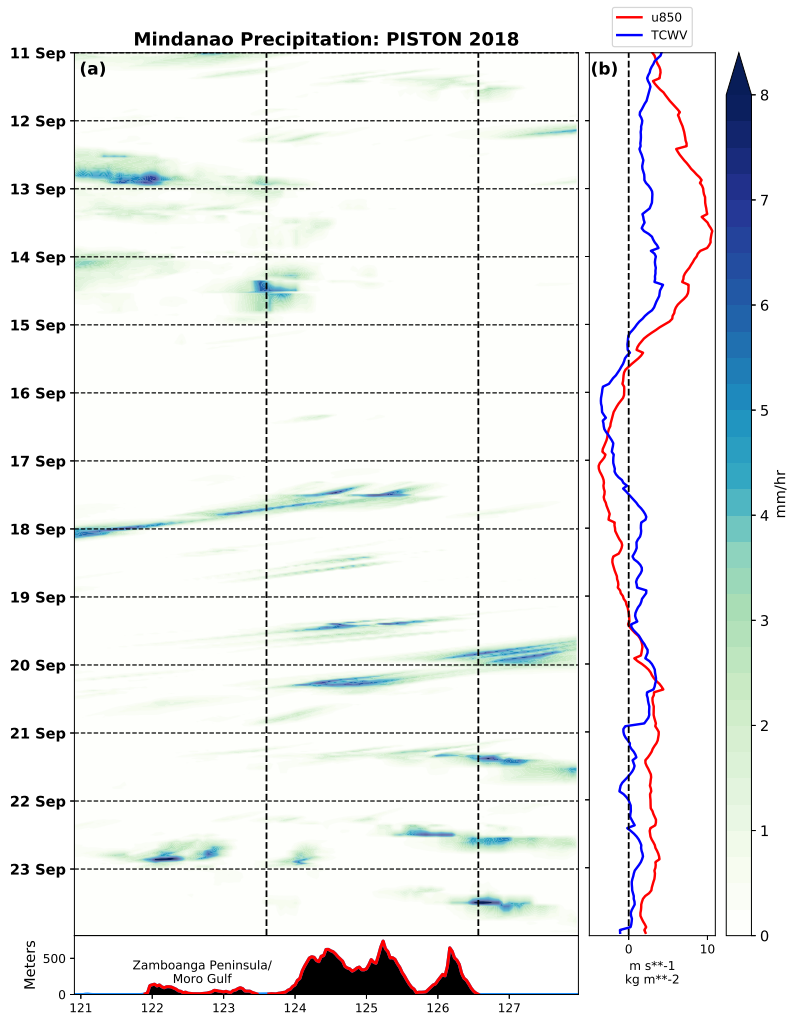


**Figure 2.8:** (a) CMORPH precipitation rate estimates (mm/hr) averaged from 6N-8N across Mindanao (Box M, Fig. 2.1) from 11 September 2018 to 23 September 2018, during one full cycle of the QBWO index. The average topography in this box from NOAA ETOPO2 is shown on the bottom, with the coastlines drawn as vertical dashed black lines. Note that there are some land points west of the western coastline here, part of the Zamboanga Peninsula. The horizontal dashed black lines correspond to 00 UTC, or 0800 local time. (b) Zonal wind at 850-hPa averaged across both latitude and longitude in Box M (red line) and total column water vapor (blue line) from ERA5, with the JJAS composite diurnal cycle removed at each hour.

cyclonic wind anomalies respectively, consistent with QBWO structure observed in prior studies (Chen and Sui, 2010; Qian et al., 2019; Yan et al., 2019).

Suppressed convection dominates much of the tropical western Pacific in phase 1, with anomalous easterly winds and dry air pushing across the region. The remnant of a westerly monsoon surge can be seen with southwesterly winds and moist conditions over the northern South China Sea and Taiwan. By phase 3, the suppressed convection and easterly anomalies are maximized over the northern Philippines, along with a significant dry anomaly. In total wind, this phase is characterized by trade easterlies dominating the entire domain outside of the mid-latitude westerlies on the northern fringes. Some indications of weakly enhanced convection begins to emerge in this phase around 10N, 145E. In phase 5, the enhanced convection becomes much more prominent, with a well defined anomalously cyclonic circulation centered over the Philippine Sea. Monsoon westerly winds start to strengthen over the Philippines and nearby waters, collocated with increasing moisture content. Enhanced convection, total column water, and westerly winds are maximized over the northern Philippines in phase 7, with an obvious monsoon surge penetrating deep into the Pacific. Overall, these structures are very similar to QBWO structures depicted in prior work (Chen and Sui, 2010; Qian et al., 2019).

Figures 2.10 and 2.11 show the impact of the QBWO on precipitation across the Philippine archipelago. Daily mean precipitation anomalies generally follow the anomalies in column moisture shown in Fig. 2.9, consistent with many other studies highlighting the importance of moisture, particularly in the lower to middle free troposphere, for maintaining convection and precipitation (Bretherton et al., 2004; Holloway and Neelin, 2009, 2010; Kuo et al., 2017; Vincent and Lane, 2017). Enhanced precipitation is manifest in a southwest to northeast band that moves to the northwest. The vast majority of these points are statistically significant at the 95% confidence level determined via a bootstrapping method. An interesting exception is Mindanao in the southern Philippines (see Fig. 2.1), which generally does not follow the precipitation pattern of neighboring seas. There is some evidence that surges of the monsoon do not provide as significant a modulation

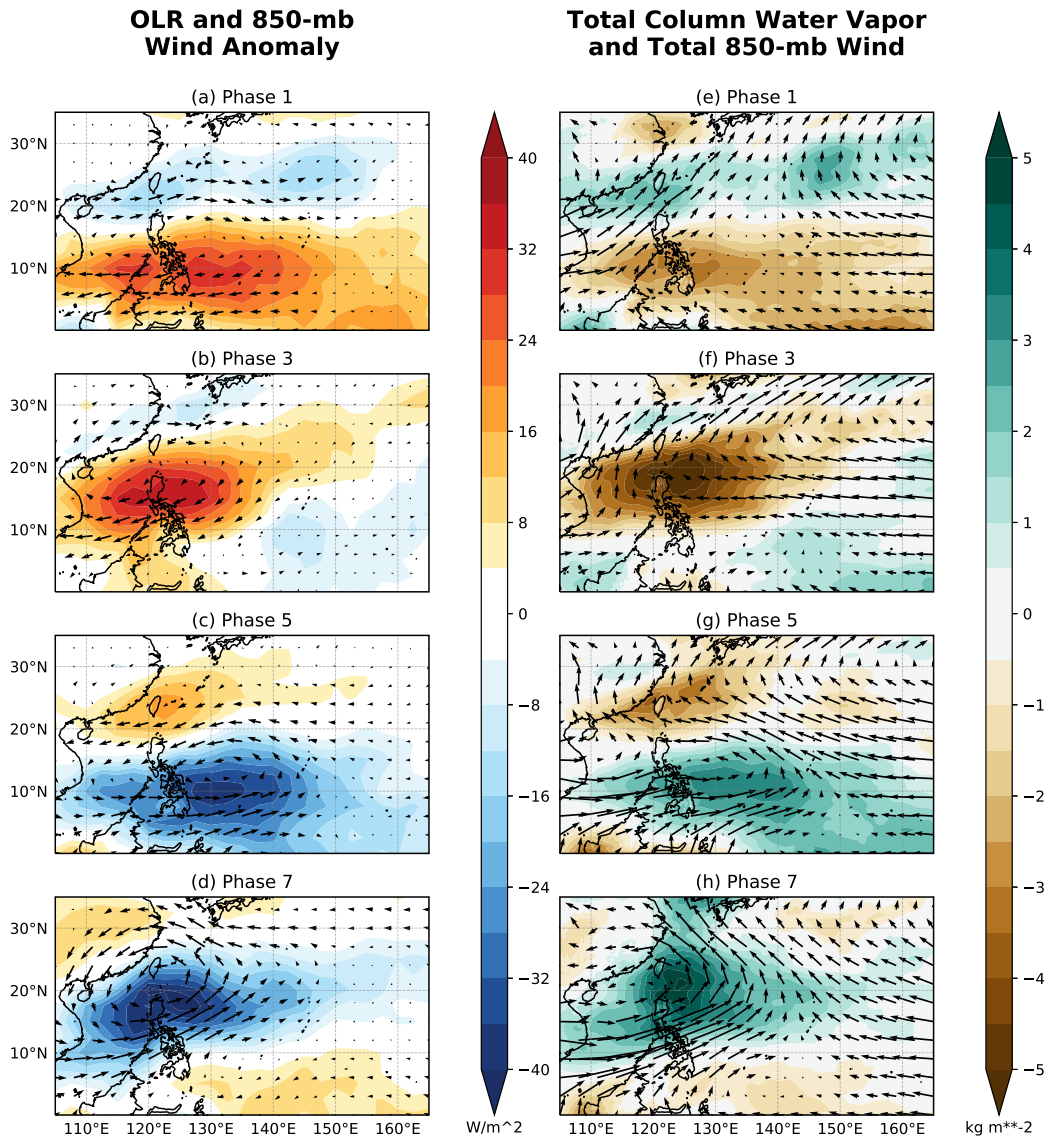


**Figure 2.9:** Composite maps by select QBWO phase over the West Pacific ocean of anomalies of OLR ( $\text{W m}^{-2}$ ) and vector anomalies of 850-mb wind from ERA5 (left column), and anomalies of ERA5 total column water vapor ( $\text{kg m}^{-2}$ ) with total 850-mb vector wind (right column). The total number of days in each composite can be ascertained from Figure 2.4

of oceanic convection near and south of this island when compared to islands further north (Natoli and Maloney, 2019; Xu et al., 2021).

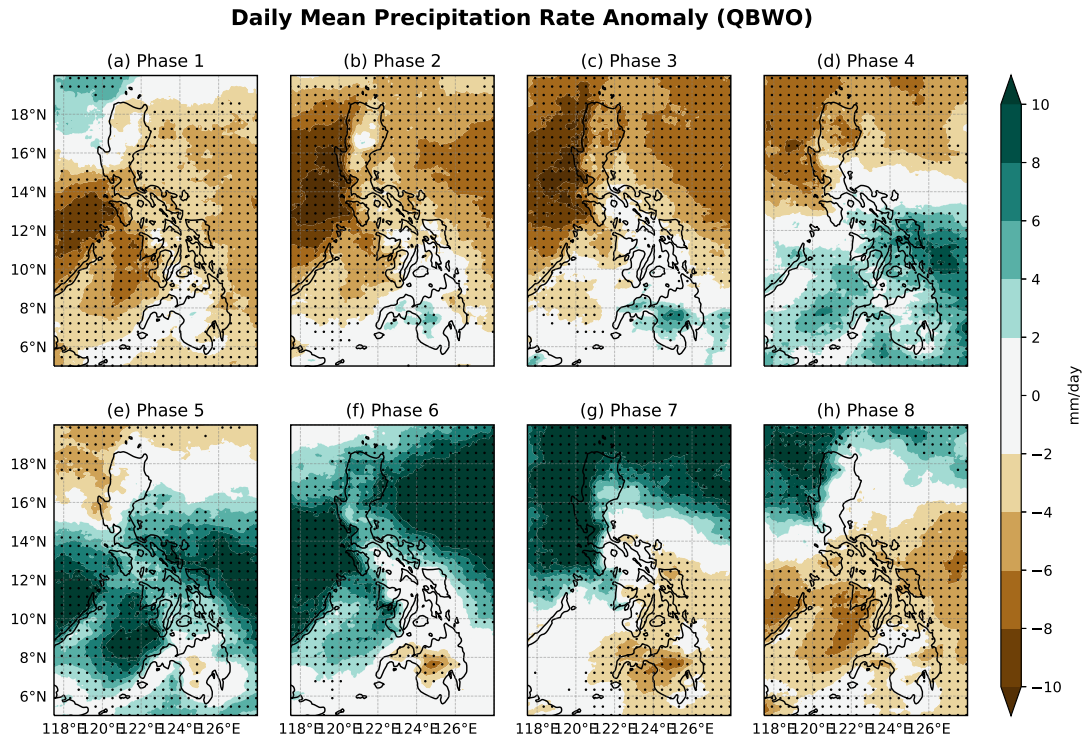


**Figure 2.10:** Anomalies in daily mean CMORPH precipitation rate composited by QBWO phase, with statistical significance at the 95% confidence level shown as dots.

The variability of the amplitude of the diurnal cycle through the QBWO cycle is noted in Fig. 2.11. Diurnal amplitude is defined in this study as the amplitude of the first diurnal harmonic of the composite diurnal cycle. A strong diurnal cycle begins to emerge over Mindanao in phase 2, peaking there in phase 3. This signal is also present in the Moro Gulf, the small body of water to the southwest of Mindanao, likely indicating offshore propagation from land-based convection (Natoli and Maloney, 2019). The central Philippines and Luzon see strong diurnal cycles maximizing in Phases 4 and 5, still about 1/4 cycle ahead of the moisture maximum which occurs around phase 7. As in many prior studies examining the impact of the BSISO on the diurnal cycle in the 8-phase framework, the amplitude of the diurnal cycle over the northern Philippines (Figure 2.11) is not

### Precipitation Diurnal Cycle Amplitude Anomaly (QBWO)

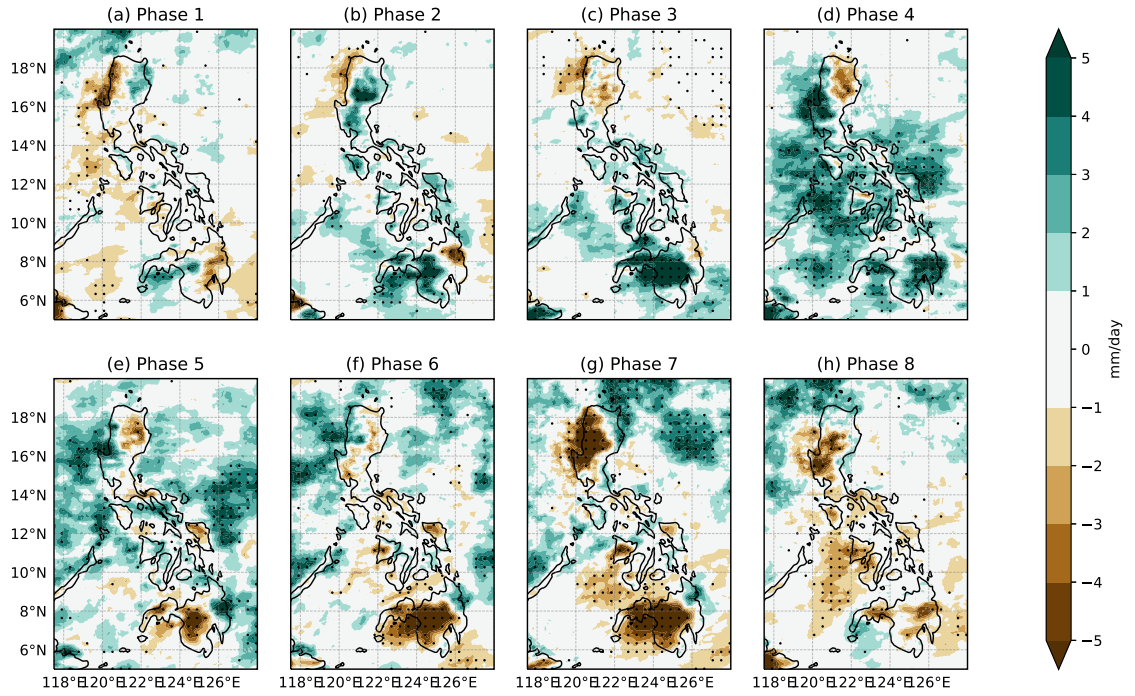


**Figure 2.11:** Anomalies in the amplitude of the CMORPH precipitation rate diurnal cycle by QBWO phase. Anomalies are calculated as the difference in diurnal amplitude between each phase composite, and amplitude of the JJAS composite diurnal cycle. Statistical significance at the 95% confidence level is shown as dots.

in phase with the daily mean precipitation (Peatman et al., 2014; Xu and Rutledge, 2018; Natoli and Maloney, 2019; Chudler et al., 2020). Despite widespread oceanic convection and abundant moisture in phase 7, the amplitude of the diurnal cycle is strongly suppressed over large islands of the Philippines. The strongest diurnal cycle tends to occur several phases before the maximum in daily mean precipitation and column moisture, when winds are still weakly easterly (Fig. 2.9f,g). Generally, this is consistent with the impact of the BSISO on the diurnal cycle. In subsequent sections, the differences between the diurnal cycle behavior associated with the QBWO and the BSISO are examined in detail with the goal of elucidating the mechanisms important to diurnal cycle regulation.

### **2.3.3 Luzon**

Luzon is the largest and most populous island of the Philippines, and presents an excellent case for examining the diurnal cycle due to the north to south orientation of its coastline and mountain ranges (Fig. 2.1). Fig. 2.12 shows Hovmöller plots of composite diurnal cycles from each QBWO phase to better interpret offshore propagation. CMORPH precipitation rate is averaged across latitude inside box L (Fig. 2.1), which covers northern Luzon, and shows a strong diurnal cycle over land peaking in the late afternoon for all phases. While the diurnal cycle is present in all, there is variability in its prominence and behavior. Phase 3, for example, has a weaker precipitation maximum and some initial propagation offshore both east and west, but precipitation dissipates rather quickly. In phases 4 and 5 (which have the strongest diurnal cycle amplitude anomalies in Fig. 2.11), precipitation rate maximizes over the highest topography and then persists much later into the night while propagating offshore, with the westward direction favored. Oceanic precipitation increases further in phase 6, while phases 7-8 shows a constantly elevated precipitation rate offshore (particularly west of Luzon), with lesser diurnal variation. There still some evidence of a diurnal cycle over the highest elevations of the island.

While the diurnal cycle over western Luzon and the South China Sea appears to peak around phase 5, there is a notable asymmetry. The diurnal cycle on the eastern part of the island appears

### Diurnal Propagation by QBWO phase

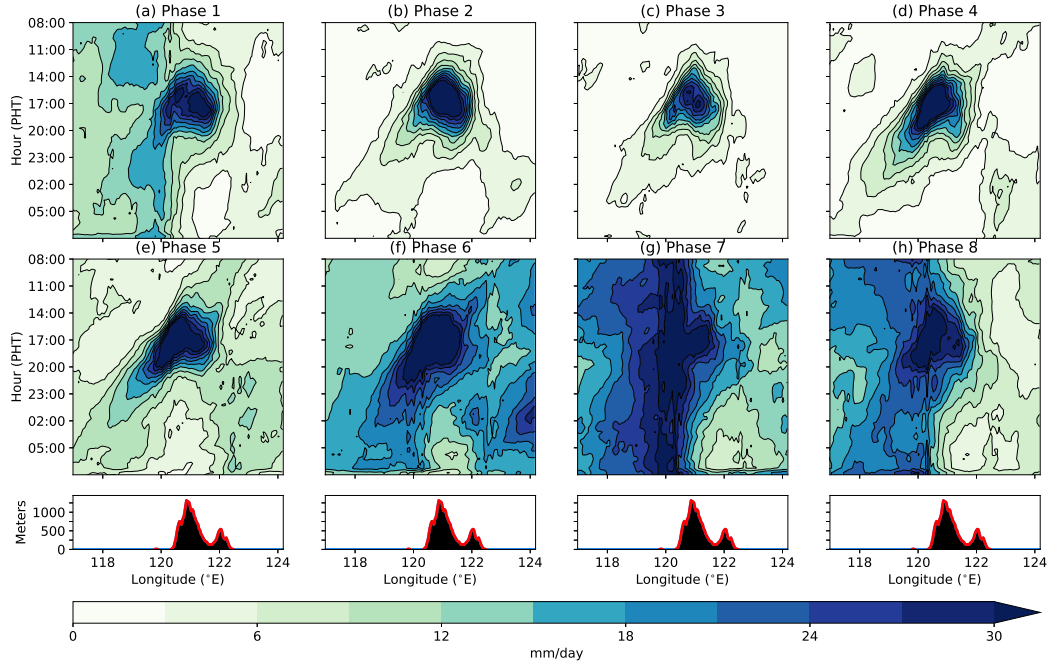


**Figure 2.12:** Hovmöller diagrams of the composite diurnal cycle of CMORPH precipitation rate (mm/day) for select phases of the QBWO index. Precipitation rates are averaged across latitude in box L (Fig. 2.1), with corresponding longitude noted below. The average elevation of topography from NOAA ETOPO2 inside box L is shown at the bottom for reference.

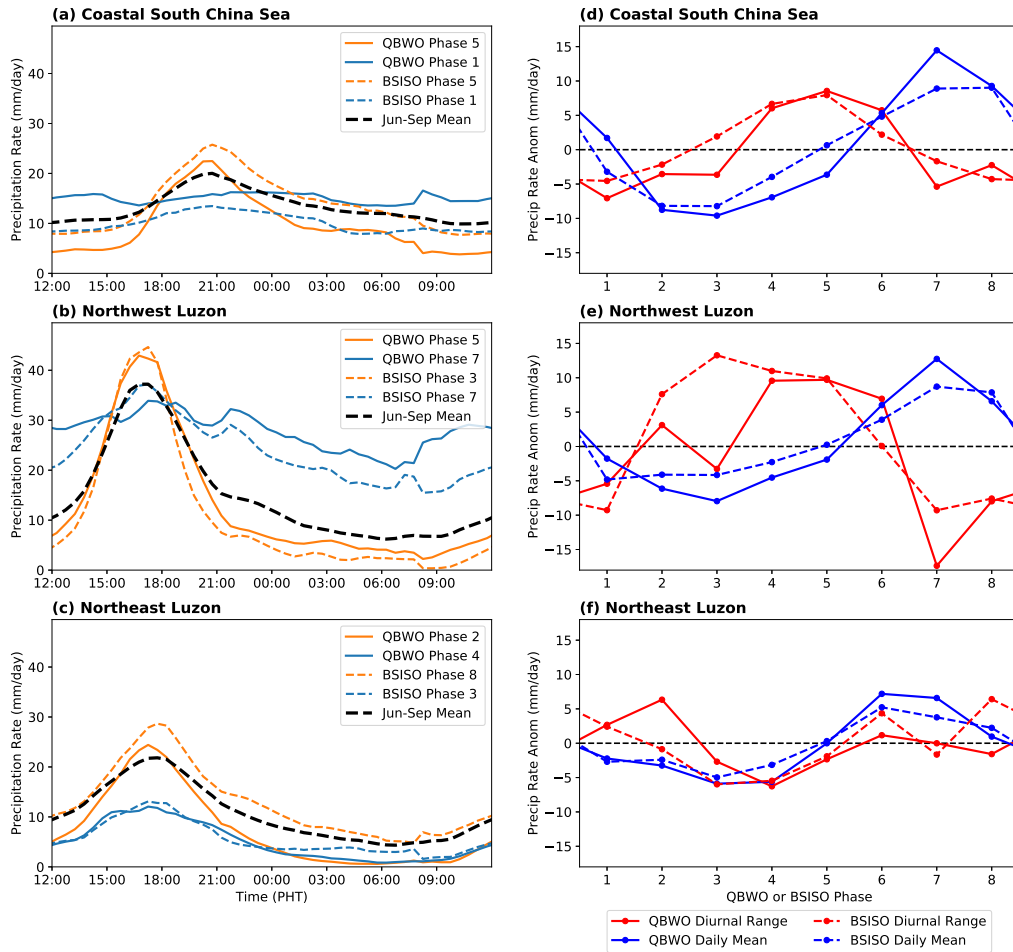
stronger in phase 1, with some weak propagation into the Philippine Sea. This asymmetry has also been noted for the impact of both the BSISO/MJO and some convectively coupled equatorial waves on the diurnal cycle (Ichikawa and Yasunari, 2006, 2008; Sakaeda et al., 2017, 2020; Natoli and Maloney, 2019), and warrants a closer look.

Figure 2.13 shows the diurnal cycle over certain subsets of the island, with boxes of spatial averaging shown in Fig. 2.1. Fig. 2.13a-c show the composite diurnal cycles in these boxes for select phases of the QBWO and the BSISO, according to the Lee et al. (2013) index. The orange lines show the phase with the largest diurnal range (difference between daily maximum and daily minimum precipitation rate) in the composite, while the blue lines show the phase with the smallest. These results were also considered for the diurnal amplitude, and the conclusions are similar. The right column shows the progression of the diurnal range and daily mean precipitation rate through each of the 8 phases of both indices.

The daily mean precipitation rates track together very closely between the BSISO and QBWO in Fig. 2.13d-f for each region. This indicates that the phase numbers are approximately equivalent in terms of proximity to the peak of the large scale convection associated with the feature of interest. Generally, daily mean precipitation varies slightly more strongly with QBWO phase than with BSISO, but the differences are modest. The diurnal range is also remarkably similar. Over northwest Luzon (Fig. 2.13e) and the coastal South China Sea (Fig. 2.13d), the largest range of the diurnal cycle leads the daily mean precipitation by about 1/4 cycle in both the QBWO index and the BSISO index. The magnitude of the change in diurnal range appears similar for both indices despite the slightly stronger modulation of the daily mean precipitation by the QBWO.

The details of the diurnal cycle (Fig. 2.13a-c) look remarkably similar as well. Over land in northwest Luzon (Fig. 2.13b), the highest amplitude phases have a sharply enhanced afternoon peak compared to the JJAS mean, but precipitation is strongly suppressed at all other times of the day. In the smallest diurnal range phases for each index, northwest Luzon sees consistently elevated precipitation rates throughout the day, with a slight bump during the evening peak that doesn't quite reach the JJAS mean precipitation rate at that time. The behavior over the South

### QBWO vs. BSISO Diurnal Cycles



**Figure 2.13:** (a-c) Composites of the spatially averaged diurnal cycle of CMORPH precipitation rate (mm/day) in the QBWO (solid) and Lee et al. (2013) BSISO (dotted) phase with the highest diurnal range (orange), the QBWO/BSISO phase with the smallest diurnal range (blue), and the full JJAS composite (dotted black). Spatial averaging is done over ocean points inside box A (a), and land points inside boxes B (b) and C (c). (d-f) The corresponding daily mean precipitation (blue) and diurnal range (red) in mm/day of each phase's spatially averaged composite diurnal cycle, by QBWO phase (solid) and BSISO phase (dotted). Each box covers a domain near Luzon.

China Sea (Fig. 2.13b) is also similar, with phase 5 in each index exhibiting heavier precipitation during the typical peak of around 2100 when westward propagating precipitation arrives. Phase 1 in each index has a fairly constant precipitation rate all day, indicating that little convection that initiates over land is propagating offshore (as also seen in Fig. 2.12a).

The two modes also exhibit the same east/west asymmetry, with the largest diurnal ranges coming after the convective maximum for each index in the eastern part of the island. Over land in northeast Luzon (Fig. 2.13f), the strongest diurnal cycle occurs after the peak in daily mean precipitation, in phases 8 and 1 for the BSISO, and phases 1 and 2 for the QBWO. Precipitation rate over this region throughout the day (Fig. 2.13c) exhibits similar behavior at the end of the convective maximum (phases 8, 1, 2) compared with northwest Luzon (Fig. 2.13b) in the phases leading up to the convective maximum (phases 3-5) in both indices. This is consistent with conclusions drawn by Sakaeda et al. (2020) on diurnal cycle asymmetry through the passage of a large scale disturbance like the MJO or an R1 wave. Overall, the diurnal cycle behavior over Luzon associated with the QBWO index strongly resembles the results previously seen for the BSISO. This motivates the hypothesis that the impact on the diurnal cycle is not unique to either mode, rather, that each mode impacts the background state near Luzon similarly, leading to congruent diurnal cycle behavior.

### **2.3.4 Mindanao**

In Mindanao, the diurnal cycle contributes much more to variability in daily mean precipitation than it does over Luzon (Natoli and Maloney, 2019). As such, the disconnect between the diurnal range and daily mean precipitation is not as distinct as for Luzon. Figure 2.14 demonstrates that the amplitude of the diurnal cycle is more closely aligned with daily mean precipitation over Mindanao, whereas the diurnal amplitude leads the daily mean by about 1/4 cycle over Luzon. Daily mean precipitation in Mindanao is not in phase with the large-scale convective maximum over surrounding waters, as it is over Luzon. This discrepancy likely results from the fact that there is very little precipitation overnight over Mindanao in any phase, as the island appears to not receive

as much oceanic precipitation during surges of the monsoon (Natoli and Maloney 2019 and their Figures 7 and 9). Xu et al. (2021) and their Figure 1 also shows that the difference between daily mean precipitation in the active BSISO compared to suppressed BSISO is much greater over the waters west of Luzon than near Mindanao.

While explaining the difference in oceanic precipitation is beyond the scope of this dissertation, we offer some hypotheses that the greater modulation of total column water vapor (Fig. 2.9) near Luzon compared to Mindanao may be responsible for this since ambient moisture is a strong control on tropical precipitation (Bretherton et al., 2004; Holloway and Neelin, 2009, 2010). It is further speculated that the location of Borneo upstream of Mindanao during the active southwesterly monsoon flow may inhibit the moisture flux. This idea is consistent with recent work by Tan et al. (2021), who showed a systematic increase in precipitation downwind of an MC island when it was removed in a WRF simulation. Future experiments could follow the methods of Tan et al. (2021) applied to the boreal summer monsoon. The behavior of the diurnal cycle for both Luzon and Mindanao is quite similar, but the diurnal cycle appears to determine daily mean precipitation much more strongly over Mindanao considering its relative lack of nearby oceanic precipitation that could impact the island itself.

One interesting feature in Fig. 2.14 is that the BSISO has a noticeably stronger impact than the QBWO on both the diurnal range and (likely as a consequence) the daily mean precipitation rate in Mindanao. However, beyond the magnitude disparity, the diurnal cycle amplitude varies as a function of each index similarly here as in Luzon. It should be emphasized that due to its location further south, both the active QBWO and BSISO impact Mindanao in an earlier phase than Luzon, thus the phase numbers of an active event do not exactly align between the two islands. Over the central portion of the island (Box E in Fig. 2.1), a strong diurnal cycle is prominent in phase 3 for both modes of intraseasonal variability (ISV) (Fig. 2.14b,e), which is about 1/4 cycle before the large scale convective maximum in QBWO phase 5 (Fig. 2.6c). Fig. 2.14a,d shows that the timing of the strongest diurnal cycle in the Moro Gulf (Box D in Fig. 2.1) with respect to phase of the ISV mode follows that over land on the western shore, indicating likely offshore propagation.

### QBWO vs. BSISO Diurnal Cycles

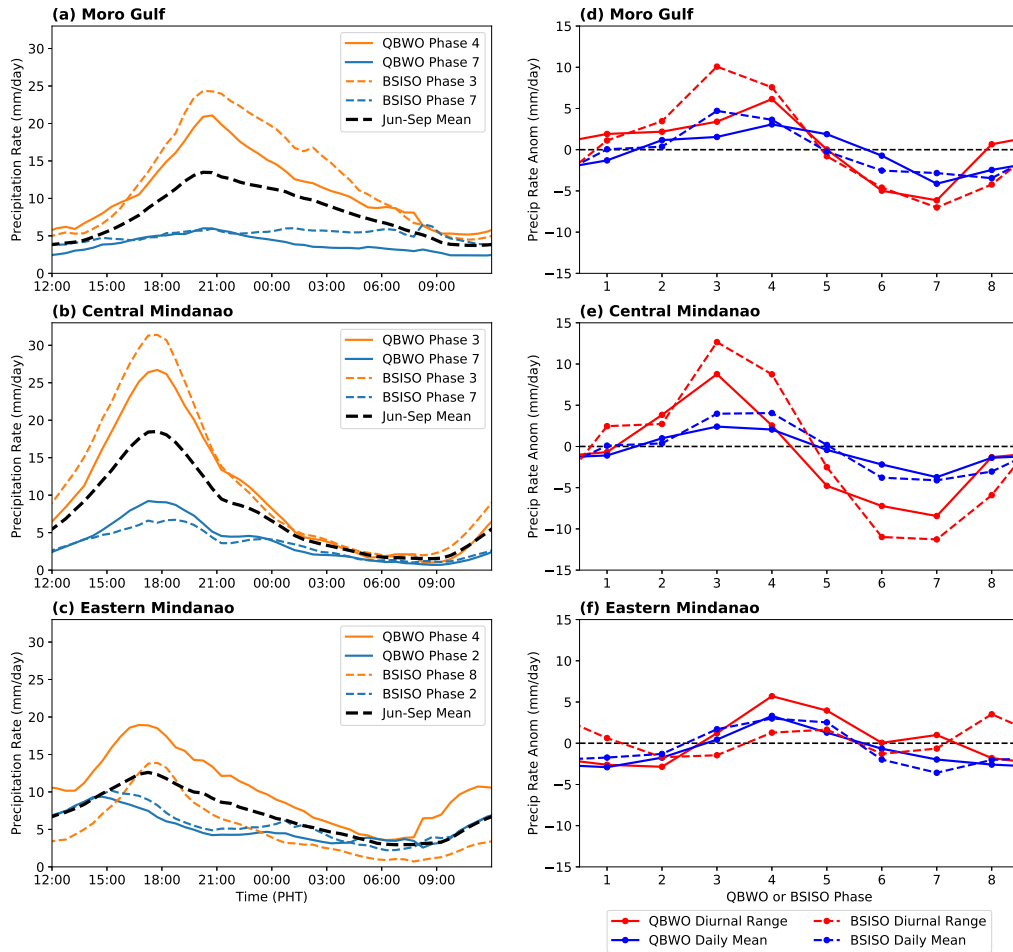


**Figure 2.14:** (a-c) Composites of the spatially averaged diurnal cycle of CMORPH precipitation rate (mm/day) in the QBWO (solid) and Lee et al. (2013) BSISO (dotted) phase with the highest diurnal range (orange), the QBWO/BSISO phase with the smallest diurnal range (blue), and the full JJAS composite (dotted black). Spatial averaging is done over ocean points inside box D (a), and land points inside boxes E (b) and F (c). (d-f) The corresponding daily mean precipitation (blue) and diurnal range (red) in mm/day of each phase's spatially averaged composite diurnal cycle, by QBWO phase (solid) and BSISO phase (dotted). As in Fig. 2.13 but for Mindanao.

The maximum diurnal cycle over eastern Mindanao Fig. 2.14c,f occurs in phases 4-5 for the QBWO and phase 8 for the BSISO, while the minimum occurs in phase 2 for both. BSISO phases 4 and 5 do experience a slight bump in the range of the diurnal cycle, but it is smaller than the QBWO increase in these phases, and smaller than the range in BSISO phase 8. In summary, the diurnal cycle behavior in Mindanao and Luzon progresses qualitatively similarly through a life cycle of both the QBWO and BSISO, with an elevated diurnal range occurring about 1/4 cycle before the large-scale convective maximum on the western side of the archipelago and over neighboring seas.

## 2.4 Discussion

### 2.4.1 Overview

In this section, we will compare and contrast the environmental background conditions associated with the QBWO and the BSISO in an effort to understand the mechanisms through which these large scale features regulate the diurnal cycle. We aim to support a hypothesis that the type of ISV mode itself is of secondary importance, and its impact on the background state through initiation of a monsoon surge is what helps determine the strength of the diurnal cycle. In other words, if two large-scale modes impact the local environmental background conditions in the same way, similar diurnal cycle behavior should be expected.

Figure 2.15 shows three environmental variables from ERA5 averaged in box L (northern Luzon, Fig. 2.1) for the left column, and in box M (Mindanao) for the right column. These variables were cited by (Natoli and Maloney, 2019) to explain much of the variability in the diurnal cycle. Figure 2.16 shows maps for phases 3 and 7 (roughly corresponding to the convective minimum and maximum over Luzon shown in Fig. 2.9) to provide context. Results are composited by QBWO/BSISO phase, with the JJAS mean shown as the dotted black line. As defined by these indices, it is evident that the environmental conditions are modulated similarly by both modes, over both islands.

Environmental moisture, particularly in the lower to middle free troposphere, has been shown to be a primary control the strength and longevity on tropical convection (Bretherton et al., 2004;

## ERA5 Daily Averaged Variables, QBWO vs. BSISO

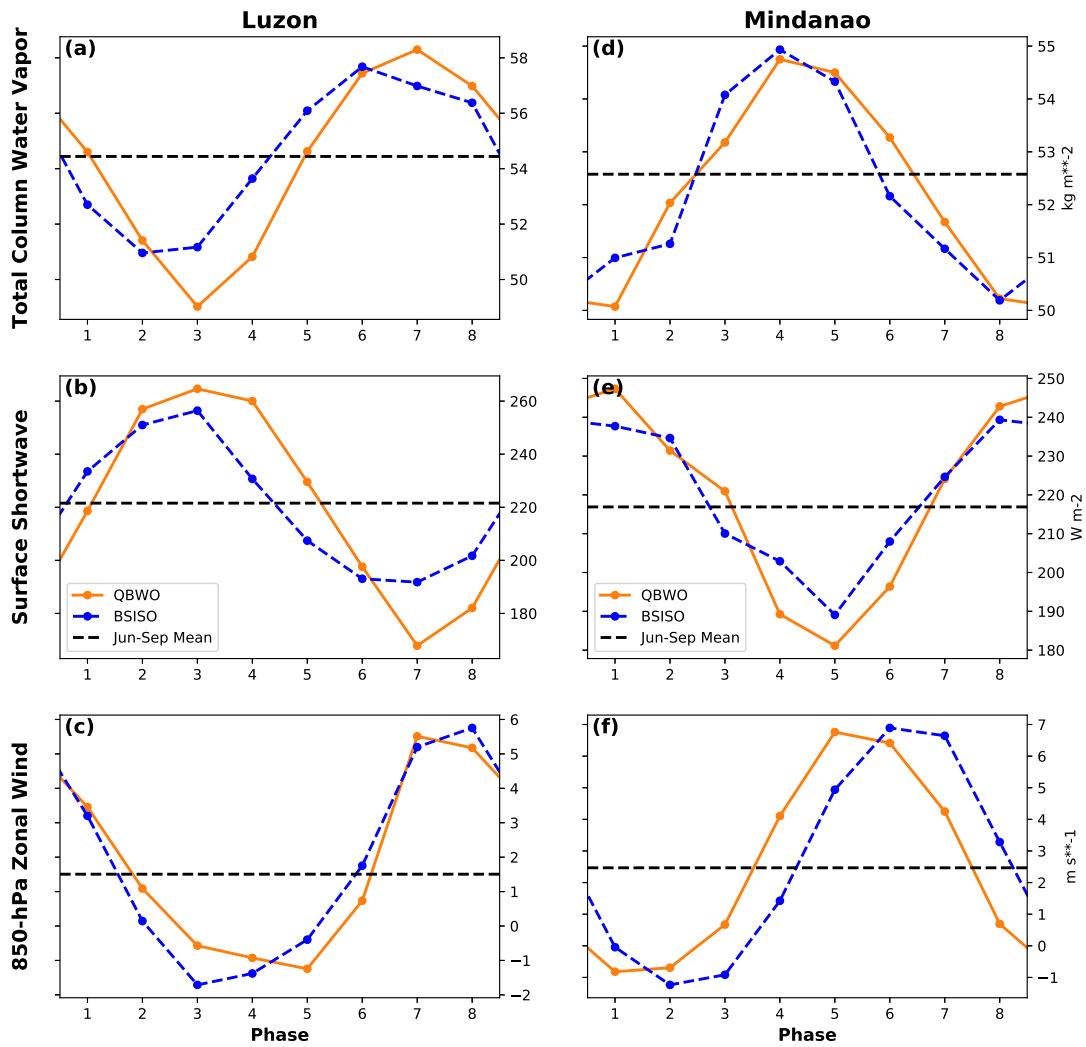


**Figure 2.15:** Daily mean values of select variables from ERA5 composited by QBWO phase (solid, orange) and BSISO phase (dotted, blue), averaged over box L covering Luzon (left) and box M covering Mindanao (right). Total column water vapor ( $\text{kg m}^{-2}$ ) is shown on top (a, d), downwelling shortwave radiation ( $\text{W m}^{-2}$ ) at the surface in the middle row (b, e), and 850-hPa zonal wind ( $\text{m s}^{-2}$ ) at the bottom (c, f). Corresponding JJAS mean values for each variable on each island are shown as a horizontal dotted black line.

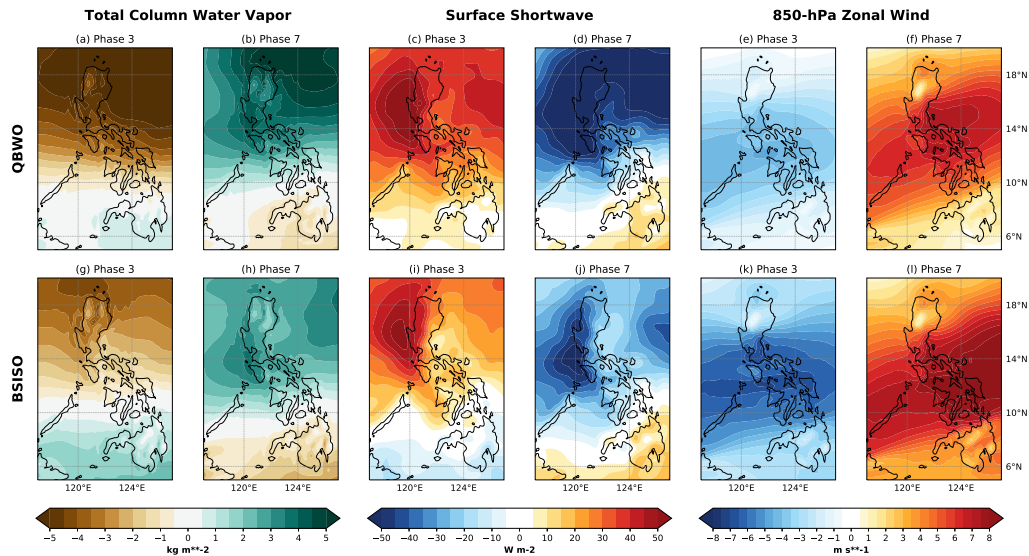


**Figure 2.16:** Daily mean anomalies from JJAS average of select variables from ERA5 composited by QBWO phase (top) and BSISO phase (bottom) over the Philippines. For each variables, phase 3 of each index is shown at the left, and phase 7 at the right. The grouping of 4 panels at the left shows total column water vapor ( $\text{kg m}^{-2}$ ), the middle grouping shows downwelling shortwave radiation ( $\text{W m}^{-2}$ ) at the surface, and the right grouping shows 850-hPa zonal wind ( $\text{m s}^{-2}$ ).

Holloway and Neelin, 2009). A rich supply of moisture in the environment will promote heavy rainfall, and longer-lived convection that propagates further offshore overnight. Dry conditions may weaken convection through entrainment, resulting in weaker rain rates and thus a weaker diurnal cycle that dissipates more rapidly (Kuo et al., 2017). The second variable considered is surface downwelling shortwave radiation, which is primarily modulated by cloud cover. Some studies have identified higher insolation as being responsible for stronger diurnal cycles occurring in the suppressed phase of the MJO (Rauniyar and Walsh, 2011; Peatman et al., 2014; Bergemann et al., 2015; Birch et al., 2016). During large-scale suppressed convection, the sky is relatively clear and the increased insolation promotes a stronger sea-breeze circulation, which then leads to an enhanced diurnal cycle. The last key variable is the lower tropospheric wind, considered in this study at 850-hPa. Onshore wind tends to inhibit the diurnal cycle on the windward side of an MC island, and enhance it on the leeward side, while also promoting leeward offshore propagation (Ichikawa and Yasunari, 2006, 2008; Oh et al., 2012; Yanase et al., 2017; Sakaeda et al., 2020;

Peatman et al., 2021). A sufficiently strong background wind may ventilate the land surface and reduce the land-sea thermal contrast, leading to a weakened diurnal cycle (Shige et al., 2017; Wang and Sobel, 2017; Qian, 2020). Thus, sufficient ambient moisture, increased solar radiation, and weakly offshore winds each are proposed to promote a strong diurnal cycle over land (Vincent and Lane, 2016). Propagation offshore to the west may be more sensitive to moisture content, given that afternoon convection develops over land (Hassim et al., 2016; Coppin and Bellon, 2019).

### **2.4.2 QBWO and BSISO Similarities**

Each mode strongly modulates total column water vapor (TCWV) over the Philippines (Figs. 2.15a,d, 2.16a-b,g-h). This is roughly in line with the large-scale convective maximum tracked by OLR (Figs. 2.9, 2.16c-d,i-j). Surface downwelling solar radiation is anti-correlated with TCWV, maximizing during the large-scale suppressed period, and minimizing on the cloudy days of the active state (Fig. 2.15b,e). The strongest diurnal cycles appear to occur when none of the above variables are strongly unfavorable, which materializes during the transition from suppressed to active large-scale convection for both modes. TCWV and insolation have competing influences, with the active phases of each mode exhibiting high TCWV, which supports diurnal precipitation (Vincent and Lane, 2016), and low insolation, which inhibits the diurnal cycle (Rauniyar and Walsh, 2011; Peatman et al., 2014; Birch et al., 2016). Lower tropospheric wind perpendicular to the coast (zonal wind in this case, since the coastline is oriented north to south), can be invoked to explain why the transition from inactive to active is associated with stronger diurnal cycles than the opposite transition (Figs. 2.15c,f, 2.16e-f,k-l)

Both the QBWO and BSISO strongly modulate low-level wind over the Philippines. Over Luzon, both indices capture easterly wind anomalies at 850-hPa in phases 3-5, and westerly wind anomalies in phases 7, 8, and 1. The phases (4 and 5 in each index) with the strongest diurnal cycles over northwest Luzon are associated with easterly wind anomalies, and weak total easterly offshore winds. In the opposite transition (phase 1 of each index), Luzon experiences near average moisture and near average shortwave radiation, but the diurnal cycle amplitude is much weaker

than phase 5 on the western coast and the SCS, associated with continued westerly wind anomalies (Figs. 2.11a,e, 2.12a,e, and 2.13d,e). Thus, high amplitude diurnal cycles appear to occur on the leeward side of the island when neither moisture or insolation are strongly unfavorable, consistent with other studies exploring the MJO-diurnal cycle relationship (Virts et al., 2013; Qian, 2020).

Offshore propagation is also similarly influenced by each mode. The phase numbers refer to the corresponding conditions for Luzon for both modes, but the mechanism is still valid for Mindanao approximately 2 phases earlier. When large-scale convection is strongly suppressed and winds are slightly anomalously easterly (phases 2-3, Fig. 2.9), precipitation still forms over land during the afternoon, but it dissipates quickly rather than propagating offshore (Figs. 2.12b,c, 2.13e). This section of the cycle is likely too dry for the most robust offshore propagation. The transition from suppressed to active (phases 4-5) exhibits continued strong diurnal cycles over land associated with easterly low-level wind anomalies, neutral insolation anomalies, and increasing moisture content. Offshore propagation to the west is most robust here (Figs. 2.12, 2.13d), as more moist air is entrained into developing convection (Hassim et al., 2016; Coppin and Bellon, 2019). During the large-scale convective maximum (phases 6-7), moisture is plentiful, but strong onshore westerly winds and cloudy conditions inhibit the diurnal cycle despite abundant oceanic precipitation in the SCS. The opposite transition in both modes (phases 8, 1) experiences continuing westerly winds despite insolation becoming more favorable. The onshore wind reduces the diurnal cycle on the west (windward) side, but strong diurnal cycles can still be found on the east (leeward) side with weak leeward propagation into the Philippine Sea (Ichikawa and Yasunari, 2006; Virts et al., 2013).

### **2.4.3 QBWO and BSISO Differences**

There are also some subtle differences in diurnal cycle behavior for the QBWO versus the BSISO life cycles, possibly due to subtle differences in modulation of the environmental background conditions. The diurnal cycle amplitude over Mindanao in phases 3 and 4 of the QBWO is smaller than phases 3 and 4 of the BSISO (Fig. 2.14a-b,d-e) despite rather similar values of environmental moisture and insolation in each (Fig. 2.15d-e). However, the 850-hPa zonal wind appears

to be more precisely in phase with the increase in moisture and cloudiness during a QBWO life cycle, with all three maximizing in phase 5 and minimizing in phase 1. For the BSISO, the increase in low level wind appears to lag the increase in moisture and cloudiness by one phase, resulting in more a more westerly wind in phases 3-5. Mindanao thus experiences more anomalously westerly winds during QBWO phases 3-5, corresponding to a weaker diurnal cycle compared to BSISO phases 3-5, and less anomalously westerly winds during QBWO phases 6-8, corresponding to a stronger (i.e. less suppressed) diurnal cycle compared to BSISO phases 6-8.

Moreover, despite the stronger modulation of moisture and insolation, the QBWO appears to modulate lower tropospheric zonal wind more weakly (Fig. 2.16e-f,k-j) over both islands. Such behavior could hint at a possible stronger diurnal cycle regulation by the low-level wind compared to the other variables, as the diurnal cycle amplitude varies similarly or even slightly less with QBWO phase compared to BSISO phase. It is also worth noting here that the spectral power of 850-hPa wind over Mindanao in the 10-15 day band cannot be statistically distinguished from red noise at the 90% confidence level (Fig. 2.2b). This is consistent with Mindanao observing noticeably greater maximum diurnal amplitude in the BSISO composites compared to the QBWO composites. The subtle difference in the timing and strength of the wind variability with the QBWO life cycle could present a plausible explanation for some of the differences in precipitation behavior. However, more work, particularly model sensitivity tests, would be required to address this more directly.

## **2.5 Conclusions**

This study has examined the variability of the Philippine diurnal cycle on the quasi-biweekly (10-20 day) time scale. To the knowledge of the authors at the time of writing, this is the first study to explore the relationship between the quasi-biweekly oscillation (QBWO), a northwestward propagating mode of variability in tropical convection and wind in the northwest tropical Pacific, and the diurnal cycle of precipitation in this region. While the MJO/BSISO-diurnal cycle relationship has received considerable attention, comparatively little has been dedicated to the quasi-biweekly

mode despite accounting for a similar or even larger slice of the variance in convection (Kikuchi and Wang, 2009; Qian et al., 2019). These findings complement and are generally consistent with that of Sakaeda et al. (2020) who examined the variability in the diurnal cycle associated with several other large-scale modes of tropical variability. This study also extends some of their ideas to the Asian and west Pacific summer monsoon region. The main findings are summarized as follows:

- The Philippines and surrounding waters experience noteworthy variability in convection and wind on the 10-20 day timescale (Figs. 2.2, 2.6, and 2.8), and this was observed in the field during the 2018 campaign Propagation of Intraseasonal Tropical Oscillations (PISTON; Figs. 2.5 and 2.6; Sobel et al. 2021).
- A QBWO index is described that captures a northwestward propagating area of enhanced convection on 10-20 day timescales, associated with increased moisture, cyclonic vorticity, and a surge of southwesterly monsoon winds (Fig. 2.9).
- Daily mean precipitation over the Philippines and coastal waters tracks with the large-scale convective envelope, except over Mindanao (Fig. 2.10). This is similar to results seen for the BSISO (Natoli and Maloney, 2019; Chudler et al., 2020; Xu et al., 2021), but the QBWO appears to have a slightly stronger impact over Luzon.
- The amplitude of the diurnal cycle on the west side of the Philippines is maximized during the late-suppressed stage and transition from suppressed to active convection (Figs. 2.11, 2.13, and 2.14).
- Prominent offshore propagation to the west into the South China Sea occurs when moisture and insolation are sufficiently high, and the low-level wind points offshore, which occurs during the transition to active convection (Figs. 2.12, 2.13a,d, 2.14a,d, 2.15). This is also consistent with findings for the BSISO, but the diurnal modulation by the QBWO appears to be slightly weaker over Mindanao (Fig. 2.14).

- The increase in moisture, cloudiness, and westerly winds arrive more or less in phase for the QBWO, while moisture leads by one phase for the BSISO (Fig. 2.15). This, combined with the slightly weaker modulation of low-level wind by the QBWO (Fig. 2.16) is hypothesized to explain why the QBWO does not modulate the amplitude of the diurnal cycle more strongly than the BSISO, particularly in Mindanao (Fig. 2.14).

These results show that the widely studied impact of the MJO/BSISO on the tropical diurnal cycle (e.g. Peatman et al. 2014; Vincent and Lane 2016, 2017; Sakaeda et al. 2017; Lu et al. 2019) is not unique to this phenomenon, complementing several other studies exploring distinct modes of variability and their impacts on local scale precipitation (Ferrett et al., 2020; Sakaeda et al., 2020). We hypothesize that the large scale mode is rather unimportant beyond its impact on the environmental background conditions to the island of interest, namely, low-level wind, free tropospheric moisture, and insolation.

Heavy daily mean precipitation (Fig. 2.10), unsurprisingly, appears to closely follow total column water vapor (Fig. 2.9; Bretherton et al. 2004; Holloway and Neelin 2009, 2010; Kuo et al. 2017), with some orographic adjustments based on prevailing wind. The amplitude of the diurnal cycle and its longevity when propagating offshore appear to be strongly related to competing the influences of insolation and moisture (which support the diurnal cycle but are out of phase with one another), and onshore wind (which inhibits the diurnal cycle and offshore propagation by decreasing the land-sea thermal contrast and thus the sea-breeze; e.g. Wang and Sobel 2017; Qian 2020). The strongest diurnal cycles with most pronounced offshore propagation generally occur on days with average to above average moisture, sufficient insolation, and weakly offshore prevailing wind. This is found for both the QBWO and the BSISO.

Testing the relative contributions of each of these key variables identified here is the subject of ongoing analysis. While we have hypothesized a possible connection between these key variables and the diurnal cycle behavior based on observations of very similar modulation by both the QBWO and the BSISO, this analysis is insufficient to make more definitive statements and deter-

mine causality. Consequently, we anticipate that our ongoing work isolating the response of the diurnal cycle to these variables in high resolution models will provide additional insight.

## Chapter 3

# The Tropical Diurnal Cycle Under Varying States of the Monsoonal Background Wind<sup>2</sup>

### 3.1 Introduction

In the prior chapter, it was shown that two modes of large-scale tropical convective variability that result in similar modulations of background moisture, wind, and insolation will demonstrate similar influences on the local diurnal cycle in the composite sense. The results of Natoli and Maloney (2019) and those outlined in Chapter 2 hinted that the background wind profile could be particularly crucial in determining this relationship. Here, we will temporarily ignore the timescale of modulation of the background, and more address the question of how the local diurnal cycle will behave given a certain background wind profile possible during the JJAS monsoon season.

To review, the low-level wind lags moisture in an MJO life-cycle by 1/8 to 1/4 cycle, and this could be a primary factor explaining why the diurnal cycle is enhanced during the suppressed-to-active transition, but not the reverse (Natoli and Maloney 2019, Chapter 2). Since MJO moisture leads the westerly wind burst (e.g. Maloney and Hartmann 1998), the suppressed-to-active transition exhibits sufficient moisture, but weak easterly winds, while the reverse has similar moisture and insolation anomalies, but strong westerly winds (Natoli and Maloney, 2019). Shige et al. (2017) showed that periods of strong environmental flow induced heavy total precipitation, but a small diurnal amplitude in India and Myanmar, while the opposite was observed during weak flow. They argued that strong winds can prevent the buildup of a thermal differential between land and sea, and thus weaken the sea-breeze and convection forced by it. Short et al. (2019) used satellite wind measurements over ocean to identify a correlation between a stronger offshore wind component (or weaker onshore wind component) and the amplitude of the diurnal perturbation in

---

<sup>2</sup>This chapter, as well as some text from Chapter 1, has been submitted for publication in *Journal of the Atmospheric Sciences* with minor changes.

wind. An idealized modeling study of a small tropical island by Wang and Sobel (2017) found that the maximum precipitation rates associated with the diurnal cycle occurred with no background wind. Increasing the background wind resulted in more mechanically forced precipitation, but a reduction in the strength of the diurnal cycle.

The background wind has also been shown to influence where on an individual island precipitation forms. For example, while exploring the variability of local precipitation related to the MJO, Qian (2020) noted a tendency for wet anomalies in both the diurnal cycle and daily mean precipitation to occur on the leeward side of large MC islands and mountain ranges. Virts et al. (2013) found that lightning activity is also enhanced on the leeward side of topography, indicative of strong convection. Recently, Riley Dellaripa et al. (2020) examined the diurnal cycle over the Philippines through a high-resolution simulation of a 2016 BSISO event and found that the active phase, associated with strong westerly winds, shifted precipitation to the east (leeward) side of Luzon when topography was removed.

Other studies have examined the influence of the background wind on offshore propagation of diurnally generated convection. Convection that initiates in the afternoon has been observed to propagate offshore in the same direction as the mean lower-tropospheric wind during the evening and overnight hours (Mori et al., 2004; Sakurai et al., 2005; Ichikawa and Yasunari, 2006; Yanase et al., 2017; Ruppert and Zhang, 2019). Recent field data from the Years of the Maritime Continent (YMC) campaign west of Sumatra Island has also addressed this issue. Examining data from the November-December 2015 pre-YMC campaign, Wu et al. (2017) indicated that a strong, westward-propagating diurnal cycle was observed consistently during low-level easterlies prior to the onset of an MJO westerly wind burst. After the onset of the strong westerlies, the amplitude of the diurnal cycle was reduced and offshore propagation to the west ceased. Yokoi et al. (2019) reached interesting conclusions by comparing the December 2017 field data to the pre-YMC campaign. They noted that during the 2017 campaign, offshore propagation of diurnally generated convection was only observed on about half of the days, while it was nearly ubiquitous in 2015. They noted that the presence of a strong El Niño event in 2015 favored consistent easterly (off-

shore) wind anomalies, while the La Niña background in 2017 led to much more frequent westerly (onshore) winds. Additionally, they noted that the cooling in the lower free-troposphere attributed to convectively generated gravity wave propagation on diurnal timescales (e.g. Love et al. 2011; Hassim et al. 2016; Yokoi et al. 2017) was present on most days, regardless of whether convection propagated offshore. They concluded that gravity wave destabilization of the offshore environment may not be a sufficient condition for offshore propagation, and instead highlighted an important role for the low-level background wind.

The work in this chapter aims to isolate the impact of the low-level background wind on the diurnal cycle of precipitation over large tropical islands in observations and an idealized model. We consider the background wind to be any wind variability on timescales longer than the diurnal cycle. The idealized simulations here are inspired by previous results focusing on Luzon island during boreal summer (e.g. Natoli and Maloney 2019, Chapter 2), but the conclusions are not meant to be exclusive to this island. Our results are also designed to be agnostic to the reasons for variability in the background wind, but we anticipate the conclusions of this study will facilitate a better understanding of the relationship between large-scale modes such as the MJO and the diurnal cycle. It will be shown that much of the variability in the diurnal cycle can be attributed to variability in the environmental background wind.

In the next section, a summary of the observational datasets and methods used will be described, followed by a description of the idealized model used to test the diurnal cycle under varying background wind conditions. Section 3 includes a discussion of observational results in which composites of the diurnal cycle near Luzon island in the Philippines are created based on the background wind profile. Section 4 describes the model simulations forced with the background wind profiles described in Section 3, examining variability in land-sea-breeze strength, offshore propagation, and gravity waves. Additionally, a series of sensitivity experiments that aim to improve understanding of the primary factors determining propagation direction are explored. Lastly, a summary of the main conclusions of this chapter is given in Section 5.

## 3.2 Data and Methods

### 3.2.1 Observations

Satellite observations and reanalysis are used for the period June-September (JJAS) 1998-2020 in this study to examine the diurnal cycle as a function of the background wind, as well as set up and verify our model experiments. Vertical profiles of wind, temperature, geopotential height, and moisture on pressure levels ranging from 1000-hPa to 100-hPa from the 5th Generation Reanalysis by the European Centre for Medium-Range Weather Forecasting (ERA5) are employed at  $0.25^\circ$  spatial resolution and hourly temporal resolution (Copernicus Climate Change Service (C3S), 2017; Hersbach et al., 2020). ERA5 single-level fields of mean sea level pressure (MSLP) and 2-m temperature (T2m) are also used at the same resolution. Satellite-derived precipitation estimates come from version 1.0 of the bias-corrected Climate Prediction Center Morphing Technique (CMORPH; Joyce et al. 2004; Xie et al. 2017). CMORPH data is examined at 8-km spatial resolution and 30-minute temporal resolution. Tropical cyclone (TC) track data from IBTrACS (Knapp et al., 2018, 2010) also provide context on the TC impact frequency in the observational results. Lastly, topography data from NOAA ETOPO2 (National Geophysical Data Center, 2006) is included as a reference for the local geography.

### 3.2.2 Binning Method

In order to stratify the period of record by vertical wind profile, a localized index is created to best represent flow on the west side of Luzon Island in the northern Philippines. Vertical profiles of zonal wind are averaged across all hours of the day, and spatially inside box A (Figure 3.1a) to create a single profile per day. Results are qualitatively insensitive to changes in the size of the box (up to covering the entire Philippines). Only ocean points were included to avoid capturing interference from the high topography of Luzon. The choice to place the box on the west side was guided by the preference for westward propagation of diurnally generated convection in this region during JJAS (Ho et al., 2008; Natoli and Maloney, 2019; Lee et al., 2021; Xu et al., 2021).

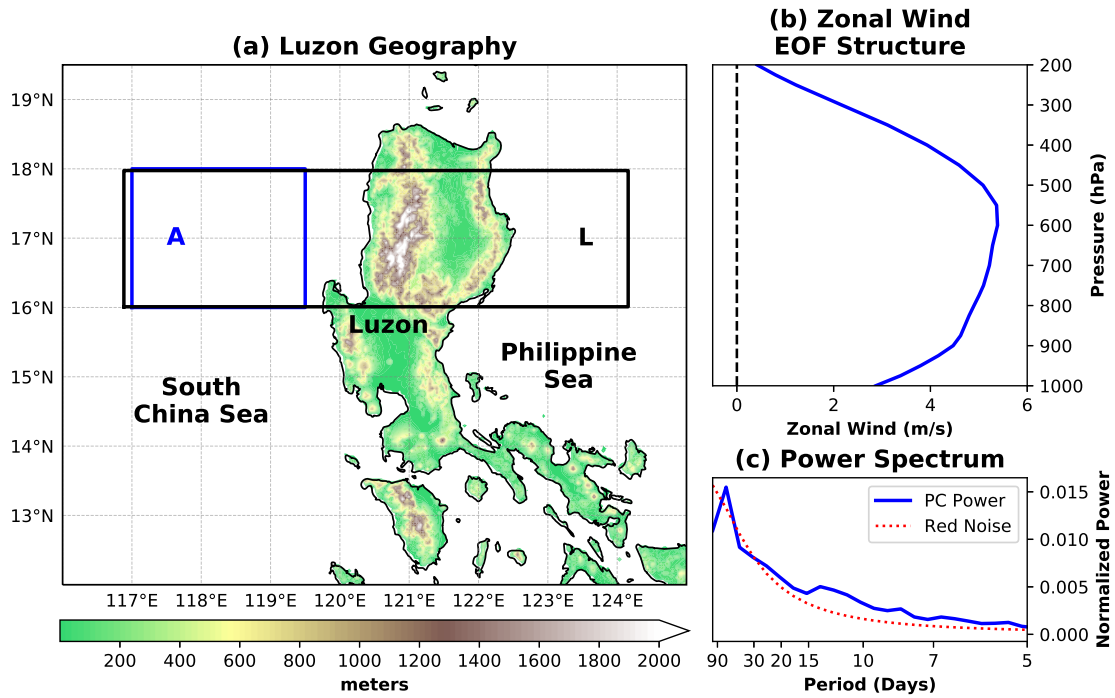


**Figure 3.1:** (a) NOAA ETOPO2 Topography (in meters) over the northern Philippines, with boxes of spatial averaging and important geographic features noted. (b) Structure of the first EOF of ERA5 zonal wind averaged in JJAS 1979-2020 inside Box A of (a), in m/s, by pressure level (hPa). (c) Normalized power spectrum of the principal component (PC) time series corresponding to the EOF in (b) in blue, with a theoretical red noise spectrum based on a time series with the same autocorrelation as the PC time series shown in dotted red.

Next, the first EOF of the vertical profile of daily averaged zonal wind was calculated for the study period (JJAS, 1998-2020) from 1000-hPa to 200-hPa. Data was first spatially averaged and then standardized about the JJAS mean and standard deviation for each vertical level. The structure of the first EOF, which explains 73.7% of the variance, is shown in Figure 3.1b retained in physical units by projecting the unprocessed data onto the standardized principal component (PC) time series. The primary mode of variability is characterized by deep westerly (or easterly, since the sign is arbitrary) flow that maximizes in the mid-troposphere, but with similar amplitude to 900 hPa. This structure and its corresponding PC time series is then used as a proxy for daily mean flow impinging on Luzon. While this is not the main subject of this study, the power spectrum for the PC is shown in Fig. 3.1c. Peaks above a theoretical red noise power spectrum with the same autocorrelation as the PC (Gilman et al., 1963) are apparent at roughly the Madden-Julian Oscillation timescale (e.g. 30-90 days), the quasi-biweekly oscillation timescale (e.g. 10-15 days), and the synoptic timescale (e.g. less than 10 days), although none are statistically significant according to an F test at the 95% confidence level. However, this does highlight some variability in this index that may be modulated by various large-scale drivers.

Observational data is then binned by the Luzon zonal wind EOF index. Nine bins are selected, centered at  $0.0\sigma$ ,  $\pm 0.5\sigma$ ,  $\pm 1.0\sigma$ ,  $\pm 1.5\sigma$ , and  $\pm 2.0\sigma$  based on the value of the PC time series on a given day. Each bin includes days with PC values within  $\pm 0.25\sigma$  of the midpoint stated above, and are inclusive on the top end. The  $\pm 2.0\sigma$  bins include days with PC values from  $\pm 1.75\sigma$  to the minimum of  $-3.58\sigma$  or maximum of  $3.92\sigma$ . ERA5 profiles of zonal wind, specific humidity, geopotential height, and temperature as well as the single-level values of MSLP and T2m are composited based on these bins. Additionally, a composite diurnal cycle of CMORPH data is generated for each of the nine bins, by averaging precipitation rates at the same times of day for all days in the bin. The number of days in each bin is indicated in Figure 3.2c, with the number of days in which a tropical cyclone (TC) center was located near Luzon (defined as inside  $10\text{-}22^\circ\text{N}$  and  $115\text{-}127^\circ\text{E}$ ) also indicated. While the  $\pm 2.0\sigma$  bins were excluded from the observational analysis

due to heavy TC influence, the TC days are still retained in the other bins. Removing them was tested and found not to qualitatively change the results.

### 3.2.3 CM1 Setup

Idealized experiments using version 20.2 of Cloud Model 1 (CM1; Bryan and Fritsch 2002) are performed to examine the sensitivity of the tropical diurnal cycle to the monsoonal background flow. One goal of this study is to realistically simulate aspects of the diurnal cycle in an idealized framework, which led to the decision to use CM1. This model has a fairly low computational cost and lends itself well to numerous sensitivity tests, some of which will be discussed in this manuscript, with work ongoing to analyze several others. The model is run in two-dimensions, with an 800-km domain in the x-direction at 1-km grid spacing, and a stretched vertical grid that begins at 50-m resolution in the boundary layer and increases to 1150-m at the domain top, which is at 20-km. This high-resolution allows for explicitly resolved convection. A 2D framework aims to further simplify our analysis. This is suitable for qualitative comparison between model runs concerning convective initiation and propagation, but may fall short on quantitative aspects compared to reality (Rotunno et al., 1988; Grant and van den Heever, 2016; Wang and Sobel, 2017). Two of the simulations were examined in 3D and the conclusions were found to be unchanged. Another sensitivity test examined a higher model top and again found little change.

The parameterizations used include the Morrison double-moment microphysics scheme (Bryan and Morrison, 2012), the NASA-Goddard radiation scheme adapted from the Advanced Regional Prediction System model, a revised surface scheme from WRF based on Monin-Obukhov similarity theory (Jiménez et al., 2012), and the Yonsei University planetary boundary layer scheme (Hong et al., 2006). The boundary conditions are open radiative at the lateral boundaries (Durran and Klemp, 1983), partial-slip at the bottom, and free-slip at the top. The inflow boundary is nudged to the base state with a time scale of 60 seconds. A Rayleigh damping layer is applied above 15-km with an e-folding timescale of 300 seconds. In addition, a large-scale nudging technique is implemented to the zonal wind, potential temperature, and water vapor mixing ratio to

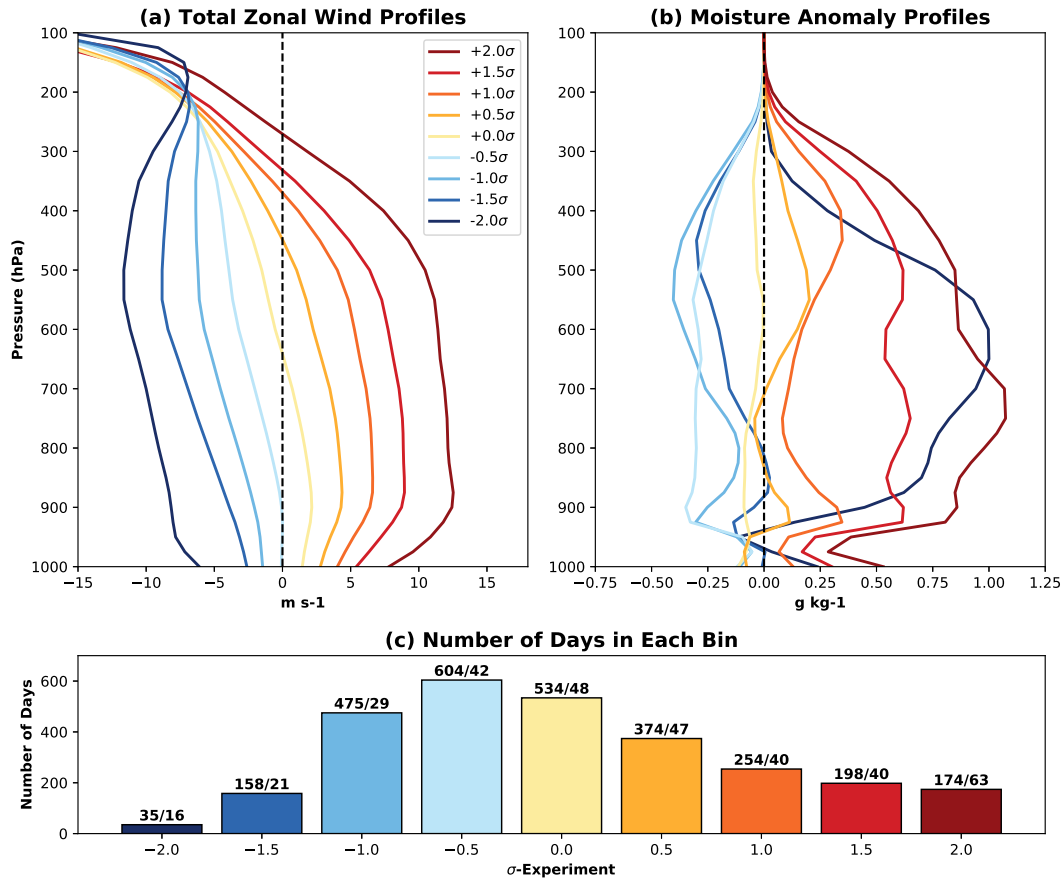


**Figure 3.2:** (a) Composite ERA5 zonal wind profiles (m/s) for all JJAS 1998-2020 days that fall in a certain bin of the PC time series of the EOF in Fig. 3.1b. Values are averaged inside Box A (Fig. 3.1a). Bins include  $0.25\sigma$  on either side of the value noted. That is,  $+0.5\sigma$  days include any day between  $0.25$  and  $0.75\sigma$ . The minimum and maximum bins are unbounded. (b) Anomalous moisture profiles in g/kg for the same bins noted in (a). (c) The number of JJAS 1998-2020 days that fall into each bin is shown as bars, with this number noted on top. The second number after the slash indicates the number of days in which a tropical cyclone center was near Luzon (inside  $10$ - $22$ N,  $115$ - $127$ E). Color coding is based on zonal wind, with easterly low-level wind bins shown in blues, and westerly bins shown in reds.

improve conservation and maintenance of the background wind. This term is applied uniformly across the domain at each time-step and vertical level, nudging the domain mean of each field back to the base-state with a timescale of 3 hours. Other timescales were tested, and 3 hours seemed to strike a good balance between maintaining base-state through the entire simulation, while also allowing the model to evolve its own diurnal cycle.

To simulate the coastal diurnal cycle, a 200-km island is placed at the center of the domain. This size is roughly the zonal extent of Luzon between 16-18°N. The model does not include topography, which is motivated by the results of Riley Dellaripa et al. (2020), who showed relatively minor differences in diurnal cycle behavior between runs with and without topography in their simulations of a BSISO event near Luzon. We acknowledge that lack of topography may affect interpretation of some of our results below, although we intend our results to be generalizable to a generic tropical island and not only Luzon. The land surface is defined as using parameters for a cropland/woodland mosaic land use, which again is representative of the lower elevations of Luzon. The base-state comes from ERA5. Initial surface temperatures come from the average SST inside Box A (Fig. 3.1a) for the ocean, and the average skin-temperature on land points below 400-m in elevation inside Box L. While the SST is fixed at 302.5K for all simulations, the soil temperature over land evolves freely.

Initial surface conditions and the base-state sounding come from averages of the surface conditions and profiles in each of the bins of the zonal wind EOF index described in the prior section. This yields 9 different simulations, each with a different temperature, moisture, and wind profile (the latter two are shown in Fig. 3.2a-b), and different surface conditions. No initial perturbations are included, and the radiation is allowed to evolve the sea-breeze circulation and diurnal cycle naturally. The model is run with a solar cycle corresponding to 17°N, and initialized at 05:00 local time on 1 August (roughly the middle of the monsoon season for Luzon; Matsumoto et al. 2020). Each simulation is 14-days in length in order to capture internal day-to-day variability for each base state, and then diurnal composites are generated. Output is saved every 15 minutes. An additional set of 24 sensitivity tests was run for 7 days each with the same model configuration,

with the goal of elucidating controls on the direction and speed of nocturnal offshore propagation. A detailed description of these experiments is left to Section 5, as presentation of the results from the main set of experiments is necessary to understand the motivation behind each set.

## 3.3 Observations

### 3.3.1 Daily Mean

Composites of CMORPH precipitation data based on bins of the zonal wind EOF index described above will be considered first to establish the importance of the background wind to the diurnal cycle in the real atmosphere and compare to prior studies near Luzon (e.g. Natoli and Maloney 2019, Chapter 2). These results will be referenced in Section 4 to demonstrate that several realistic aspects of the diurnal cycle can be simulated in CM1. The average profiles in Box A (Fig. 3.1a) for each bin are shown in Fig. 3.2a-b. The bins well-stratify zonal wind, and are slightly skewed towards low level westerlies since the JJAS mean profile is westerly in the low levels (not shown). The more westerly bins tend to be more moist than the easterly bins, consistent with the general behavior of monsoon season in the Philippines in which periods of moist, westerly monsoon activity are interspersed with drier easterly trade winds (Park et al., 2011; Chudler et al., 2020). One exception is the  $-2.0\sigma$  bin, which is from a very small sample of 35 days (Fig. 3.2c), nearly half of which had a tropical cyclone storm center near Luzon. The significant tropical cyclone influence explains why its corresponding humidity profile is much more moist than average. Due to the small sample size, this bin is excluded from the observational discussion below. The results from the  $+2.0\sigma$  bin are generally a more extreme depiction of the results from the  $+1.5\sigma$  bin, and are also excluded from the discussion below for the sake of brevity. Both bins are retained for the model experiments to test more extreme conditions.

The daily mean precipitation from CMORPH composited for each wind bin is shown in Figure 3.3. Statistical significance at the 95% confidence is shown as dots. This was calculated via a bootstrap method in which each composite was compared to the daily mean precipitation rate from 1000 random composites with the same number of days as each bin shown in Fig. 3.2c. Days

with stronger westerly winds (e.g.  $+1.5$ ,  $+1.0\sigma$ ) experience elevated precipitation over the SCS, windward of the highest topography of Luzon. Similarly, the strongest easterly bins tend to exhibit reduced precipitation on the west (leeward) side of the island, but enhanced precipitation on the east (windward) side. Some counter-intuitive features are apparent in the middle three bins. For example, there is elevated precipitation on the east side of Luzon in the  $+0.5\sigma$  simulation despite being on the leeward side of the island. As will be detailed in the next subsection, this may be explained by variability in the diurnal cycle that is enhanced on the leeward side of topography (Virts et al. 2013; Natoli and Maloney 2019; Qian 2020, Chapter 2). This effect can be substantial enough to dominate the daily mean precipitation anomalies when the background is light.

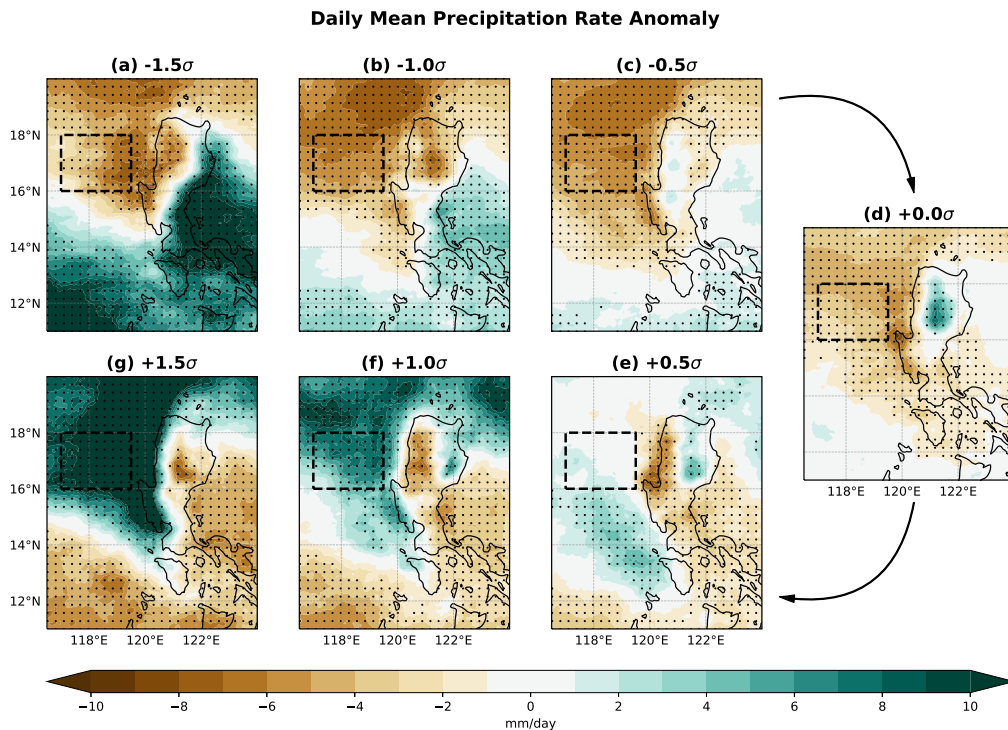


**Figure 3.3:** Daily mean precipitation anomaly (mm/day) from CMORPH (JJAS, 1998-2020) averaged by bins of zonal wind EOF index. Anomalies are from the average precipitation rate on all JJAS days. Increasing zonal wind rotates clockwise around the figure. The  $\pm 2\sigma$  bins are not shown due to heavy tropical cyclone influence.

### 3.3.2 Diurnal Cycle

Many important aspects of diurnal precipitation variability in Luzon can be captured by compositing days according to the environmental wind alone. While the focus here is on the wind, ongoing research will attempt to address the relative importance of wind compared to other aspects of the environment that may co-vary with wind, such as moisture and insolation. In this study, the amplitude of the diurnal cycle is defined as the amplitude of the first harmonic of a composite diurnal cycle, as in Natoli and Maloney (2019). Figure 3.4 shows the difference between the diurnal amplitude in the composite of days in each environmental wind bin, and the diurnal amplitude in the composite of all JJAS days. Statistical significance at the 95% level is again shown after the amplitude of the bin composite diurnal cycle is compared to the amplitude of the composite diurnal cycle in the 1000 random composites made for each bin. Details on the mean state of the boreal summer precipitation patterns near Luzon can be found in Natoli and Maloney (2019). The anomalies in diurnal amplitude binned by environmental wind alone are generally stronger over portions of Luzon than was found to be associated with large-scale modes like the BSISO (e.g. Figure 6 of Natoli and Maloney 2019).

Over land, the diurnal cycle is generally strong when the low-level zonal wind is weak (e.g.  $-0.5\sigma$ ,  $0.0\sigma$ , and  $+0.5\sigma$  bins), and weak when the low-level wind is strong (e.g.  $-1.5\sigma$  and  $+1.5\sigma$ ), consistent with Shige et al. (2017). In addition, there is a noticeable preference for a strong diurnal cycle in the lee of the island. For example, days in the  $-1.0\sigma$  and  $-0.5\sigma$  bins (which have low-level easterly winds) tend to have a strong diurnal cycle on the west side of the island, and a weak diurnal cycle on the east side. The opposite behavior is apparent in the  $+1.0\sigma$  and  $+0.5\sigma$  composites. This is consistent with prior studies examining other MC islands with observations (e.g. Virts et al. 2013; Liang and Wang 2017; Qian 2020; Sakaeda et al. 2020). A clear shift is seen as westerly wind increases, starting with a weak diurnal cycle across all of Luzon during strong easterlies (e.g.  $-1.5\sigma$ ), followed by a stronger diurnal cycle progressing across the island from west to east as weak to moderate easterlies transition to weak to moderate westerlies (e.g.  $-1.0\sigma$  to  $+1.0\sigma$ ), leading to a strong suppression during strong westerlies (e.g.  $+1.5\sigma$ ).

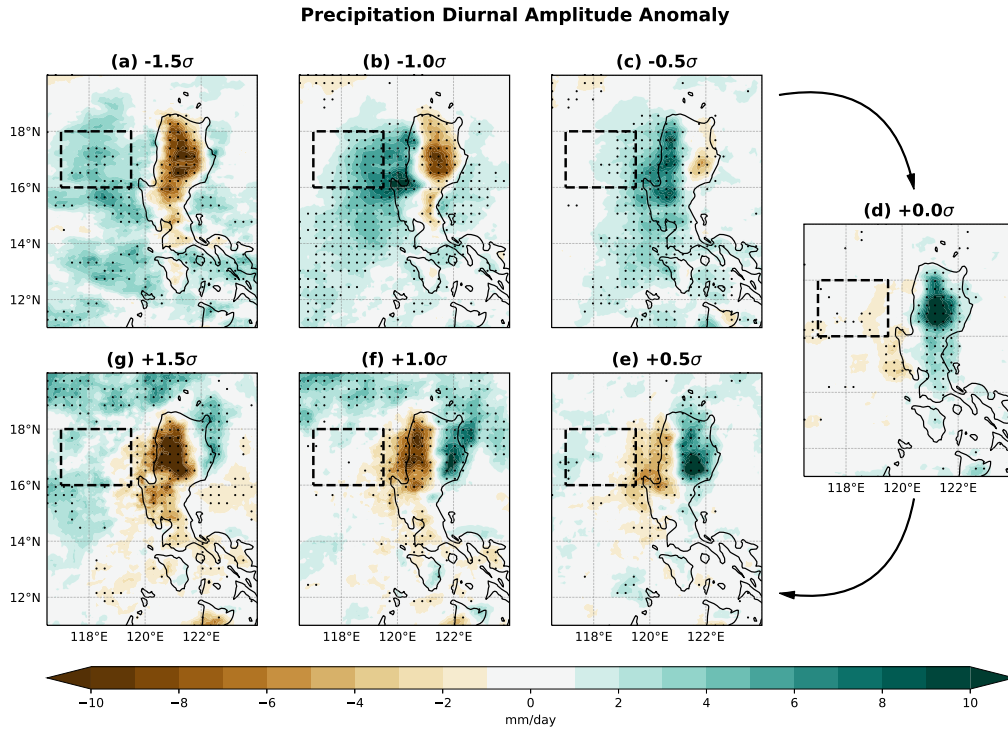


**Figure 3.4:** Anomaly in the diurnal cycle amplitude (defined by the first harmonic of the composite diurnal cycle) composited by bin of the zonal wind EOF index for JJAS 1998-2020. Anomalies are from the amplitude of the full JJAS composite diurnal cycle. Increasing zonal wind rotates clockwise around the figure. The  $\pm 2\sigma$  bins are not shown due to heavy tropical cyclone influence.

The offshore propagation of the diurnal cycle is also strongly associated with the vertical profile of zonal wind. Figure 3.5 shows Hovmöller diagrams of the composite diurnal cycle for each bin, latitudinally averaged from 16-18° in Box L (Fig. 3.1). The black line superimposed estimates the average propagation speed by finding a line of best fit between the longitudes of maximum precipitation rate at each 30-minute time step between 16:00 and 01:00 local time.

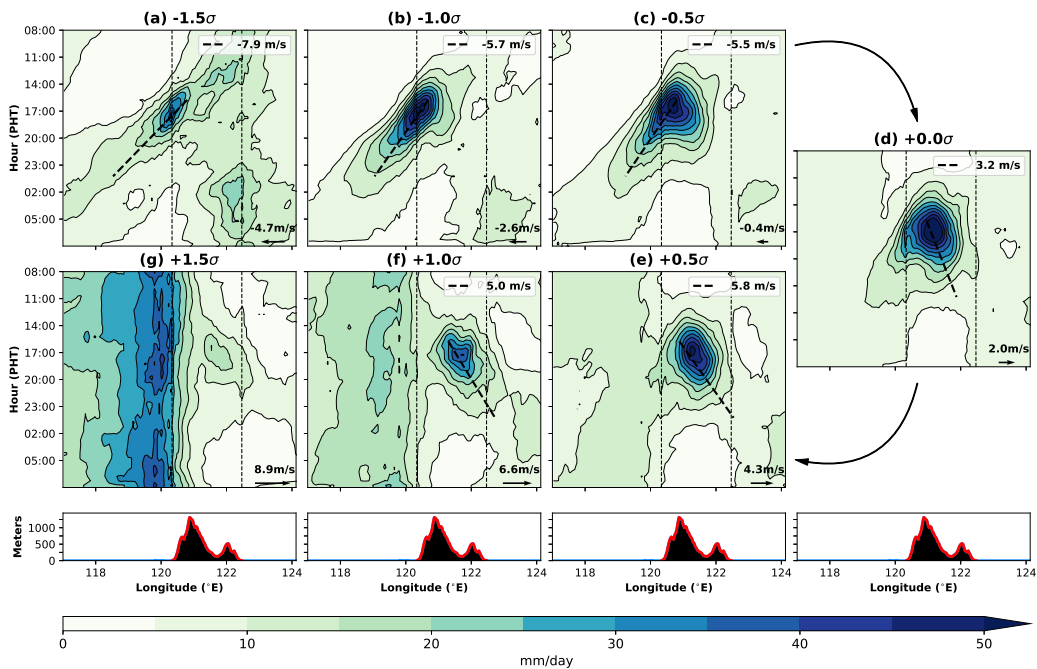


**Figure 3.5:** Hovmöller diagrams of CMORPH composite precipitation rate (mm/day) on days binned by zonal wind EOF index averaged across latitude inside Box L (Fig. 3.1a). Time starts at 08:00 local time in each panel, and increases downward. Dotted lines are estimates for a line of best fit between 16:00 and 01:00 of the longitude with the maximum precipitation rate at each time. This calculation only includes longitudes on the side of the island (east or west) that contains the maximum precipitation rate at 16:00. The estimated speed of propagation following this line of best fit is noted in the legend for each panel. This is not shown for the  $+1.5\sigma$  bin since little offshore propagation can be discerned. Increasing zonal wind rotates clockwise around the figure, with the composite 850-hPa zonal wind shown as a vector in each panel. The  $\pm 2\sigma$  bins are not shown due to heavy tropical cyclone influence.

Fig. 3.5 clearly shows that while westward propagation of convection is prominent during the westerly monsoon season (e.g. Aves and Johnson 2008), this occurs largely on days in which the

wind is more easterly than average (e.g.  $-1.5\sigma$ ,  $-1.0\sigma$ , and  $-0.5\sigma$  days). In fact, days with near average or westerly zonal wind exhibit little westward propagation, but do display some preference for eastward propagation. On strong easterly days ( $-1.5\sigma$ ), a weak enhancement of precipitation occurs on the western coastline in the late afternoon, that then propagates offshore overnight. This behavior is more obvious on weak to moderate easterly days ( $-1.0$  and  $-0.5\sigma$ ), where heavy precipitation forms over the high topography during the late afternoon, and then migrates predominantly to the west during the evening and overnight, propagating at roughly 5-6 m/s. When the wind is near the JJAS mean ( $0.0\sigma$ ), strong precipitation is observed closer to the center of the island, with weak evening propagation in both directions. Observations in two field campaigns near Sumatra indicated similar dependence of offshore diurnal propagation on the wind profile normal to the coastline (Yokoi et al., 2017, 2019).

The westward branch disappears in weak to moderate westerlies ( $+0.5$  and  $+1.0\sigma$ ). Precipitation develops over the east side of the highest topography (near the center of the island), and then propagates to the east in the evening at roughly 5-6 m/s. However, convection moving to the east on these days does not tend to last as long or propagate as far when compared to westward propagating convection in the  $-1.0\sigma$  and  $-0.5\sigma$  bins. We speculate this may be due to the secondary mountain range on the eastern coast interfering with land-breeze and cold pool propagation, but this is beyond the scope of this study and could be a caveat of the modeling results below. During strong westerlies ( $+1.5\sigma$ ), little precipitation is observed over the central and eastern part of Luzon, but very heavy rainfall is apparent over the SCS and western slope of the highest mountains throughout the day. These results are consistent with Ho et al. (2008), who also examined the Philippines, and an analysis of Sumatra island by Yanase et al. (2017). This behavior is also consistent with what many prior studies have shown regarding the relationship between large-scale modes of variability like the MJO (which impacts the wind profile) and the local diurnal cycle (e.g. Ichikawa and Yasunari 2006, 2008; Vincent and Lane 2016; Wu et al. 2017, Chapter 2). These observational results will be used as a benchmark against which to evaluate the successive model experiments.

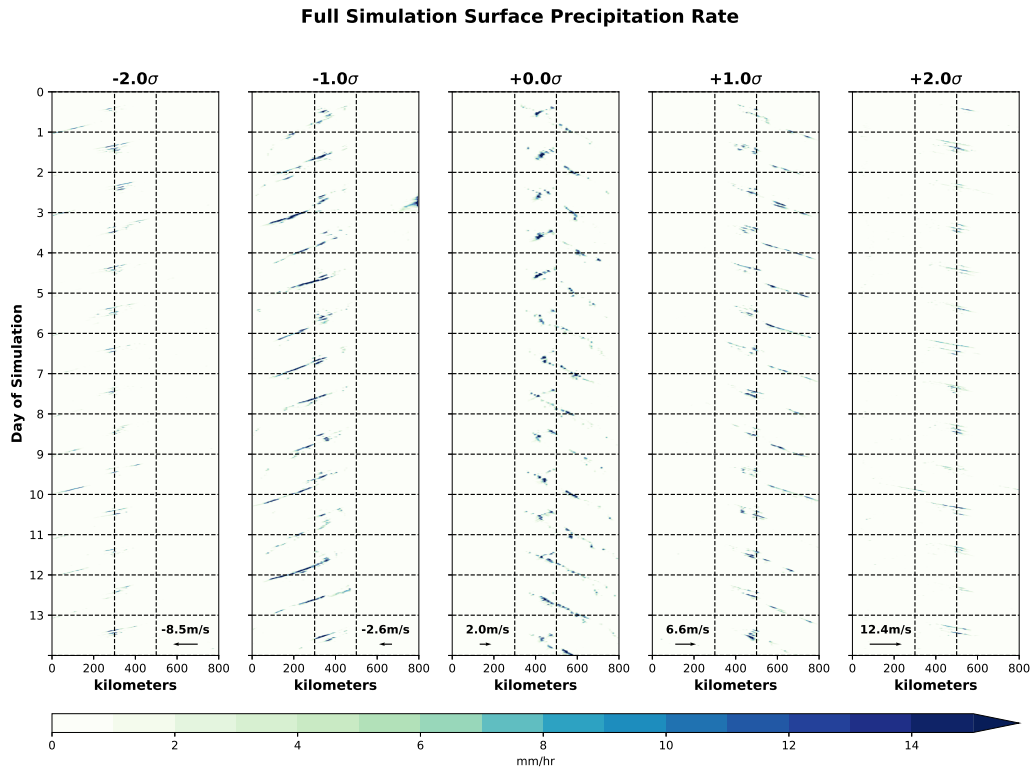
## 3.4 CM1 Experiments

The CM1 simulations will be described in detail in this section. First, the general behavior of precipitation in each experiment will be discussed. Then in Section 4b, the sea-breeze circulation will be explored in more detail in order to explain why the diurnal cycle is stronger in the weak wind simulations. Section 4c will evaluate the extent to which gravity waves are important for determining the existence and speed of offshore propagation. Lastly, this section will conclude with a discussion of the sensitivity experiments that are designed to elucidate more information about the controls on propagation direction in the model.

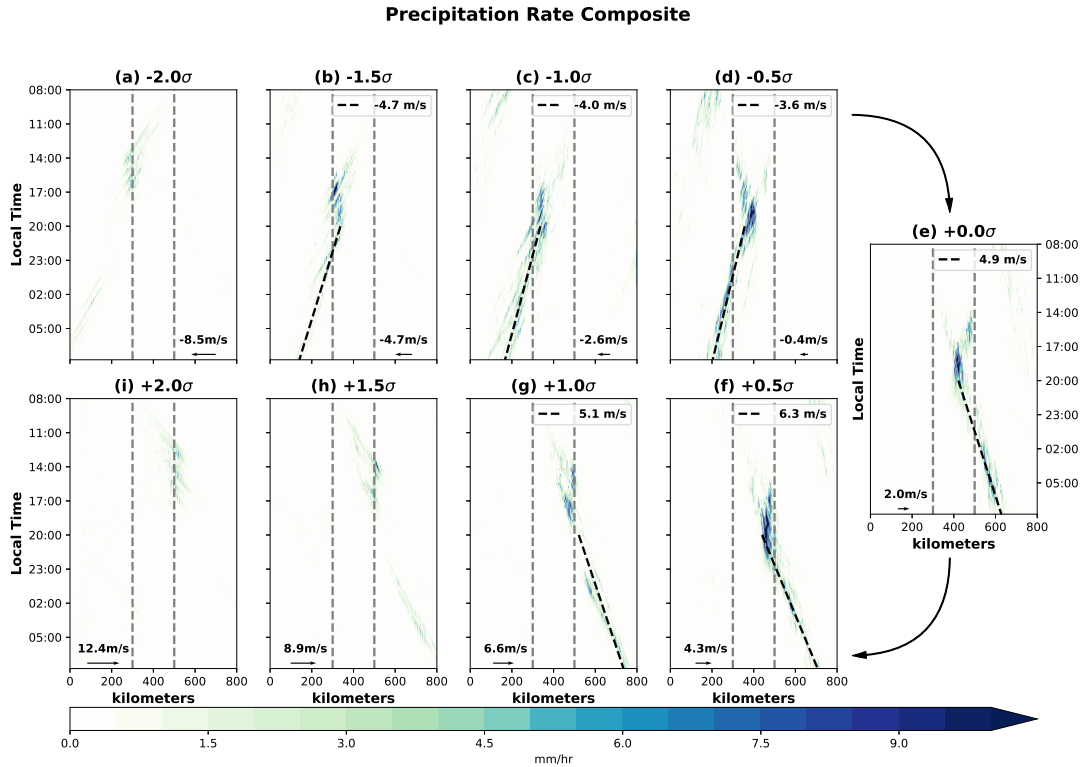
### 3.4.1 Simulation Overview

Figure 3.6 shows the modeled precipitation rate for the full 14-days of the CM1 simulations (showing every other experiment for brevity). Precipitation develops nearly every day in all simulations, and relatively consistent behavior is seen from one day to the next. Notably, convection that develops over land (marked by the vertical dotted lines) propagates in the same direction on every day in the same simulation. This justifies our use of a composite of all 14 days for the remainder of this study, as some internal day-to-day variability in the diurnal cycle may be smoothed over, while highlighting signals present every day. Figure 3.7 shows the daily composite surface precipitation rate, found by averaging across all 14-days for every time step (i.e. 96 time steps at 15 minute intervals). For experiments that exhibit coherent offshore propagation, the best fit line connecting the longitude of maximum smoothed (to a 5-km grid) precipitation rate at each time step between 20:00 and 08:00 local time is shown as a dotted black line with its average propagation speed noted in the panel legend.

Remarkably, the idealized 2D simulation can capture several important aspects of the diurnal cycle in observations shown in Fig. 3.5. The easterly experiments (e.g.  $-1.5\sigma$ ,  $-1.0\sigma$ ,  $-0.5\sigma$ ) demonstrate mainly westward propagation, consistent with CMORPH observations. Similarly, the weak to moderate westerly experiments (e.g.  $+0.0\sigma$ ,  $+0.5\sigma$ ,  $+1.0\sigma$ ) all exhibit eastward nocturnal propagation. The model propagates convection offshore at around 4-7 m/s, with some variability



**Figure 3.6:** Precipitation rate (mm/hr) for the full 14-day simulation of select Cloud Model 1 (CM1) experiments. The x-axis in each is in km, with the coastlines marked as vertical dotted black lines. 05:00 on each day is noted as a horizontal dotted black line. The base-state 850-hPa zonal wind is shown as a labelled vector in each panel.



**Figure 3.7:** Daily composite of the 14-day CM1 simulations showing precipitation rate by longitude at 1-km resolution. Each simulation varies the base state with the wind and moisture profile bins shown in Fig. 3.2 (as well as surface variables and thermal profiles, which are not shown). Dotted gray lines note the coastlines, and the dotted black line follows a line of best fit connecting the longitude of maximum precipitation rate at each time between 20:00 and 08:00. This is calculated based on precipitation rate smoothed to 8-km resolution. Increasing zonal wind in the base state rotates clockwise around the figure, with the base-state 850-hPa zonal wind shown as a labelled vector in each panel.

between the experiments. These speeds are consistent with land-breeze or cold pool propagation speeds (Finkele, 1998; Vincent and Lane, 2016; Hassim et al., 2016). The easterly experiments tend to initiate deep convection in the late afternoon over the west (leeward) side of the island, as in observations. The opposite is evident in the westerly experiments. These results complement prior modeling studies showing similar diurnal cycle behavior (Saito et al., 2001; Liang et al., 2017). Very strong background winds (e.g. the  $\pm 2.0\sigma$  experiments) suppress the diurnal cycle, as was also seen in observations. Precipitation tends to develop earlier in the day, reaches a weaker maximum, and dissipates faster in the strong wind experiments, consistent with other modeling studies (Zhong and Takle, 1993; Chen et al., 2017; Wang and Sobel, 2017).

Deep convection appears to develop closer to the eastern coastline in the  $+0.5\sigma$  and  $+1.0\sigma$  simulations than in the corresponding observations. In addition, storm longevity is symmetric between eastward and westward observations in the model, unlike observations, possibly because of the lack of topography in the model. This can be explained by invoking the results of Riley Dellaripa et al. (2020), who showed that the presence of topography in a simulated diurnal cycle over Luzon focused precipitation over the mountains in suppressed BSISO conditions (analogous to our easterly experiments). However, it is worth noting that Riley Dellaripa et al. (2020) found a relatively modest change in diurnal cycle behavior without topography, which was partial motivation for incorporating the simplification of flat topography in our simulations. The asymmetry in observations that is not present in the flat model may be explained by the concentration of the highest peaks near the western coast (Fig. 3.1) and the lower mountains near the east coast interfering with eastward propagation.

### 3.4.2 Land-Sea-Breeze Circulation

Figure 3.8 shows composite zonal wind at the lowest model level (25m) for every other simulation. The top row (a-e) shows the total wind, while the bottom row (f-j) shows the perturbation from the base state. In the simulations with a weaker wind speed (e.g.  $-1.0\sigma$  and  $0.0\sigma$ , Fig. 3.8b-c, g-h), a roughly symmetric sea-breeze begins to develop around 08:00, and then expands offshore

and propagates inland from both coastlines. In the  $0.0\sigma$  experiment, some weak precipitation is visible between about 11:00 and 17:00 along each sea-breeze front, but strong convection doesn't develop until the two sea-breeze fronts converge, at around 17:00 (Fig. 3.7). At night, a weak land-breeze develops and only propagates offshore in the leeward direction with the precipitation signal. It is unclear if convection is being driven by the land-breeze, or if the apparent land-breeze is simply the low-level wind contributed by cold pool dynamics. The asymmetry in which side of the island experiences stronger convection is also illustrated in the sea-breeze front. The sea-breeze front appears to propagate inland faster on the windward side (e.g. towards the lee), leading to initial convergence between the two fronts on the leeward side (e.g. Saito et al. 2001).

In the strong wind experiments, the sea-breeze is much weaker, with little diurnal change in the wind on the windward side, and anomalous onshore flow in the afternoon on the leeward side that temporarily cancels the prevailing offshore flow (Fig. 3.8a,e,f,j). Interestingly, the strong wind experiments exhibit nocturnal leeward propagation of low-level offshore winds that are stronger than the background wind (i.e. negative perturbation moving westward overnight in Fig. 3.8f and positive perturbation moving eastward overnight in Fig. 3.8j). This signal is mostly uncoupled from convection, although precipitation does form on this boundary on a few days in the simulation (Fig. 3.6a). We speculate that this is related to the timing of precipitation. Convection has already largely dissipated in the strong wind experiments by the time the land-breeze initiates.

Figure 3.9 demonstrates the impact of the prevailing wind on the thermal properties of the land surface. Marked variability can be discerned depending on the background wind. On the western half of the island in the strong westerly experiments, the amplitude of the diagnosed 2-m temperature ( $T_{2m}$ ) perturbation is much smaller than in the weak to moderate easterly experiments (Fig. 3.9a). The  $+2.0\sigma$  simulation, for example, has a nocturnal minimum temperature of around  $25.5^{\circ}\text{C}$ , and a daily maximum of around  $31^{\circ}\text{C}$ . The  $-1.0\sigma$  experiment conversely drops to  $24.5^{\circ}\text{C}$  at night, and warms to nearly  $34^{\circ}$  during the day. Inverse behavior is seen over the eastern half of the island, with weak thermal contrast in  $-2.0\sigma$  and the strongest  $T_{2m}$  diurnal cycle in  $0.0\sigma$  (Fig. 3.9b). The strongest wind experiments reduce the afternoon maximum temperature even on the

Lowest Model Level Zonal Wind Composite

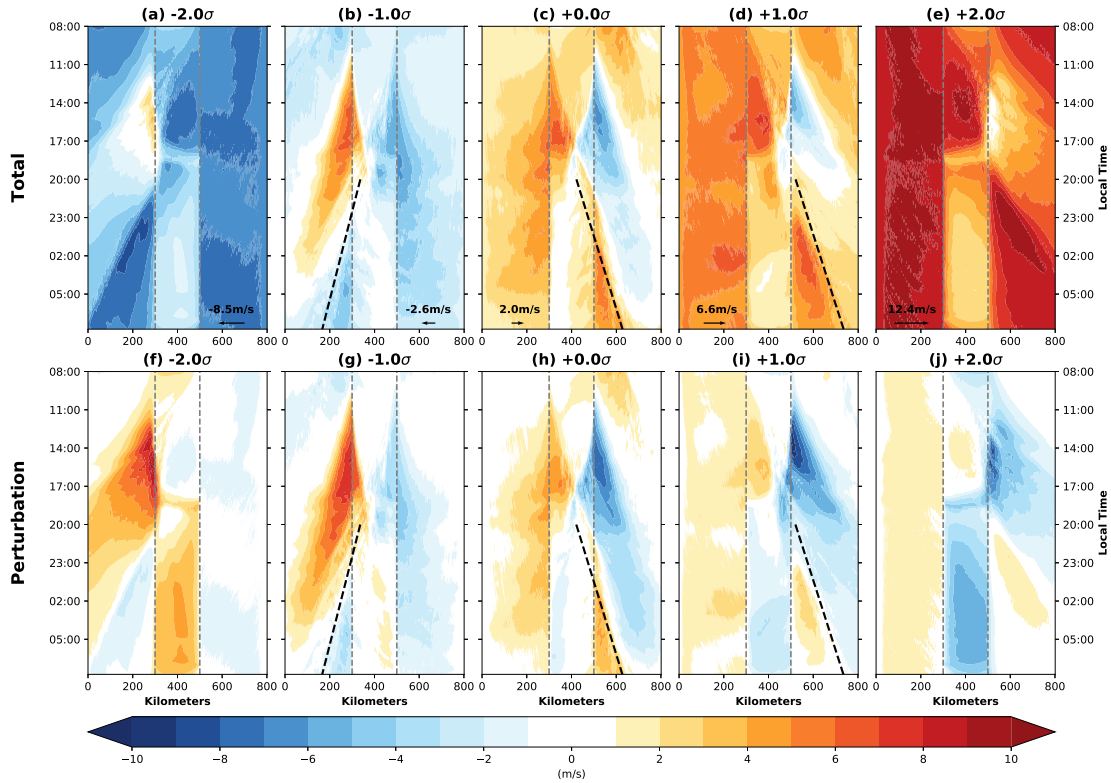


**Figure 3.8:** Lowest model level zonal wind (in m/s) Hovmöller diagrams for select experiments. The total zonal wind is shown on the top, and the perturbation from the base-state is shown on the bottom. The line of best fit for the maximum precipitation rate shown in Fig. 3.7 for the corresponding experiment is shown as a dotted black line. Coastlines are denoted with dotted gray lines. The base-state 850-hPa zonal wind is shown as a labelled vector in each panel in the top row.

leeward side. This is more obvious on the west half of the island, likely due to the asymmetry in wind speeds through all simulations (e.g. the magnitude of the wind in the  $+2.0\sigma$  experiment is greater than the  $-2.0\sigma$  experiment). Thus, the amplitude of the T2m diurnal cycle appears to maximize during weak to moderate offshore prevailing winds.

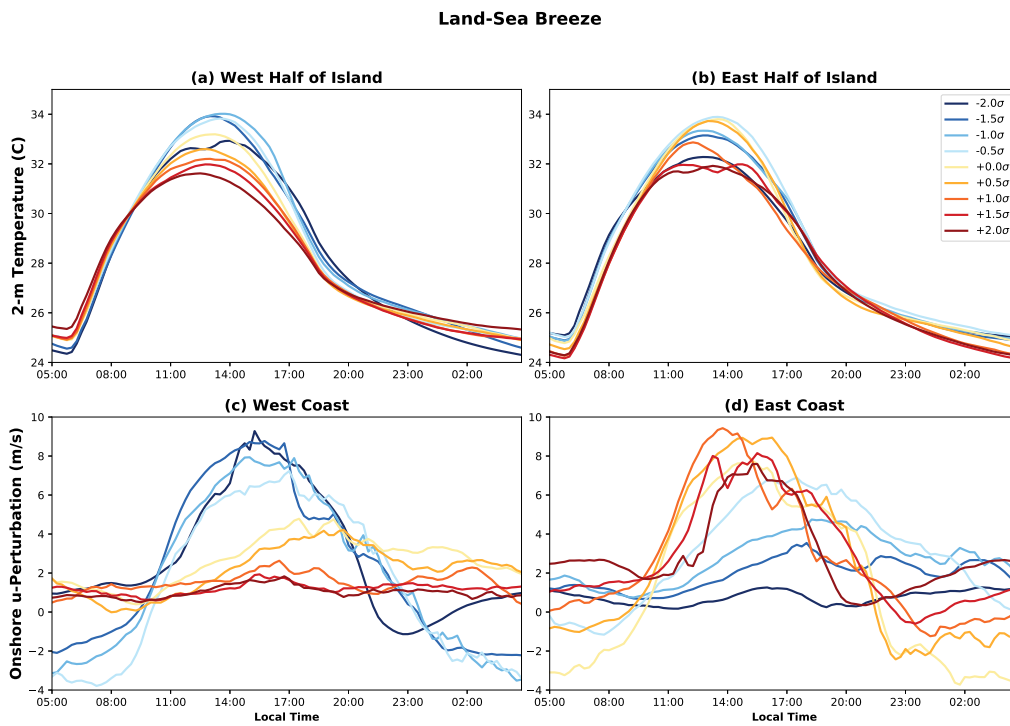


**Figure 3.9:** (a) Diagnosed 2-m temperature (C) for each experiment averaged for each time across the western half of the island. (b) As in (a), except averaged over the eastern half of the island. (c) Onshore (i.e. westerly positive) perturbation zonal wind (m/s) at the lowest model level (25m) for each experiment averaged for each time between the western coast and 25-km offshore. (d) As in (c), except with easterly winds defined as positive, averaged between the eastern coast and 25-km offshore.

The alterations in surface thermal contrast also affect the coastal low-level wind (Fig. 3.9c-d). The onshore perturbation- $u$  ( $u'$ ) is dramatically stronger on the leeward side on both coasts.  $u'$  is around 6-9 m/s during the afternoon hours on the leeward coast, but generally much weaker (0-5 m/s) with a peak later in the afternoon on the windward coast. Overnight, onshore prevailing wind leads to essentially no development of a land-breeze offshore (note that the spatial average in Fig. 3.9c-d only includes ocean points within 25-km of the coast). Weak offshore flow develops in

the late evening on the lee-side, supporting enhanced convergence and thus nocturnal precipitation compared to the windward coast. These results support the hypotheses of many prior observational studies arguing that a strong prevailing wind can alter the diurnal cycle by ventilating the land surface, reducing the land-sea thermal contrast, and thus the sea-breeze circulation on the windward coast (e.g. Shige et al. 2017; Natoli and Maloney 2019; Qian 2020, Chapter 2).

To summarize, a stronger background wind in our simulations leads to a weaker land-sea breeze circulation especially on the windward coast, which is attributed to the reduction in the thermal contrast. The sea breeze fronts propagate inland from both shores with weak to moderate wind, but tend to converge and initiate convection on the leeward side of the island due to the windward front propagating faster. A signal resembling a land breeze can be seen propagating off the leeward coast in all simulations, but this has a stronger coupling to precipitation in the weaker wind simulations. These results add support to the hypothesis that surges of the monsoon lead to a reduced land-sea temperature contrast, and thus a weaker sea-breeze and precipitation diurnal cycle.

### 3.4.3 Gravity Waves

In this section, the offshore propagation of convection and its relationship to convectively generated gravity waves in this model will be explored. Gravity waves have frequently been shown to be important for the propagation of diurnally generated tropical convection (Grant et al., 2018), either through direct coupling of convection to propagating gravity waves (e.g. Mapes et al. 2003; Lane and Zhang 2011), or by destabilizing the offshore environment in advance of convection propagating with the land breeze or cold pool (e.g. Love et al. 2011; Hassim et al. 2016; Yokoi et al. 2017; Vincent and Lane 2018).

Figure 3.10 shows a composite vertical profile of perturbation- $\theta$  (which is assumed to reflect heating profiles) and total cloud mixing ratio averaged over the half of the island on which convection develops in select experiments. Strong warm anomalies through the depth of the troposphere resulting from deep convective heating are observed during the afternoon hours, especially in the 0.0 and 1.0 $\sigma$  experiments. Deep convection initiates between 14:00 and 17:00, as indicated by the

cloud mixing ratio contours stretching up to the tropopause. After about 20:00, a transition to a more stratiform heating profile can be seen, as indicated by warm anomalies in the 8-12-km layer and cool anomalies below. This could be described as an  $n=3$  mode, since it features heating over cooling, but only fills about  $2/3$  of the depth of the troposphere (Lane and Reeder, 2001; Lane and Zhang, 2011). The  $-1.0\sigma$  simulation has a less clear transition from convective to stratiform heating profiles, as neither stands out strongly in Fig. 3.10a. During the overnight hours, it is difficult to determine the dominant heating profile, but numerous higher-order heating modes are seen over land, although the precipitating system has moved out of the averaging domain of Fig. 3.10 by this time. This figure demonstrates that our simulations produce heating profiles (reflected in the perturbation- $\theta$ ) capable of initiating numerous gravity wave modes, including the higher order modes often discussed as important for propagating tropical convection (Tulich and Mapes, 2008; Love et al., 2011).

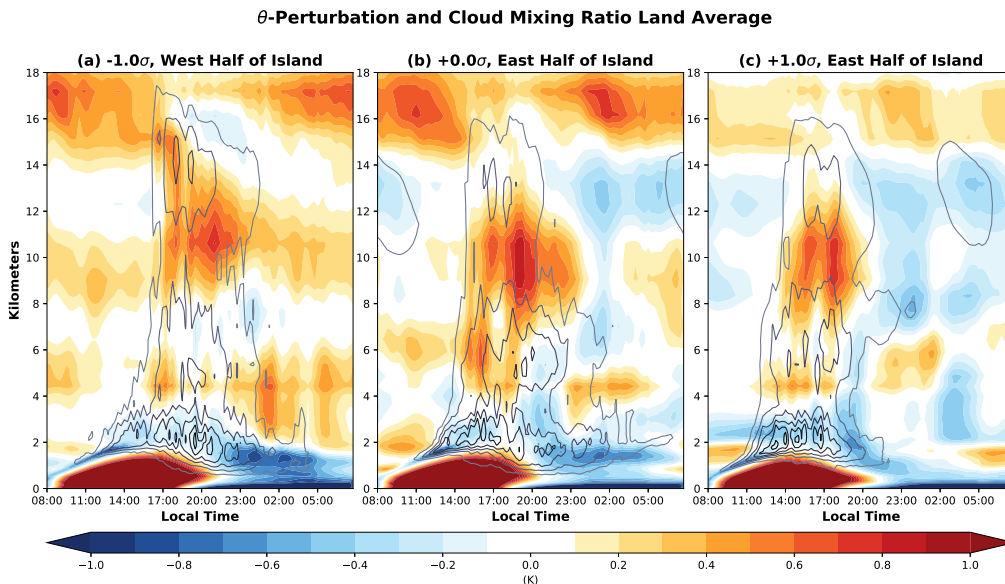


**Figure 3.10:** 14-Day composite of perturbation potential temperature in colors, and total cloud mixing ratio (liquid+ice) contoured starting at 0.005 g/kg, then 0.02 g/kg and every 0.02 g/kg thereafter to 0.1 g/kg. Each variable is averaged over (a) the western half of the island for the  $-1.0\sigma$  experiment, (b) the eastern half of the island for the  $+0.0\sigma$  experiment, and (c) the eastern half of the island for the  $-1.0\sigma$  experiment. Local time starts at 08:00 and increases to the right, with height in kilometers on the y-axis.

Figure 3.11 shows Hovmöller plots of perturbation- $\theta$  at certain levels for the  $0.0\sigma$  experiment. Only day 2 is displayed here, since the composite blurs the propagating gravity waves that happen at slightly different times each day across simulations. The other experiments are not shown here for the sake of brevity, but are qualitatively similar. The propagating gravity wave signal associated with deep convective heating initiated shortly after 17:00 in Fig. 3.10b can be seen as a warm anomaly rapidly propagating outward in both directions. The propagation speed is estimated at 30-40 m/s, which is consistent with speeds attributed to the deep convective mode in past studies (Tulich et al., 2007; Love et al., 2011; Coppin and Bellon, 2019). Slower propagating signals (e.g. roughly 10-20 m/s) emanating from the location of precipitation are also evident in this figure around 20:00, coinciding with the development low-level cooling in Fig. 3.10b. These are likely related to higher order gravity wave modes, and some lead to cooling in the lower free troposphere, and thus destabilization.

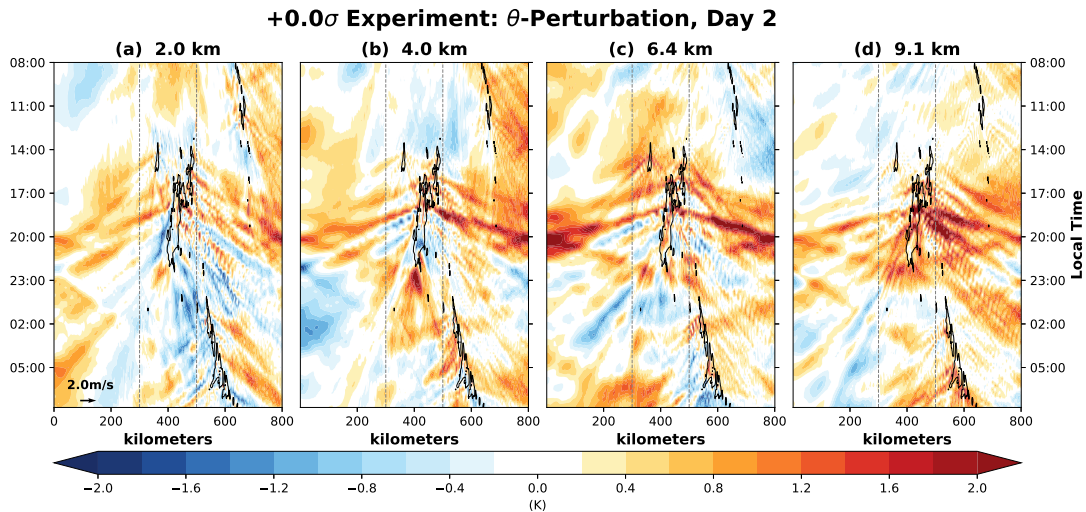
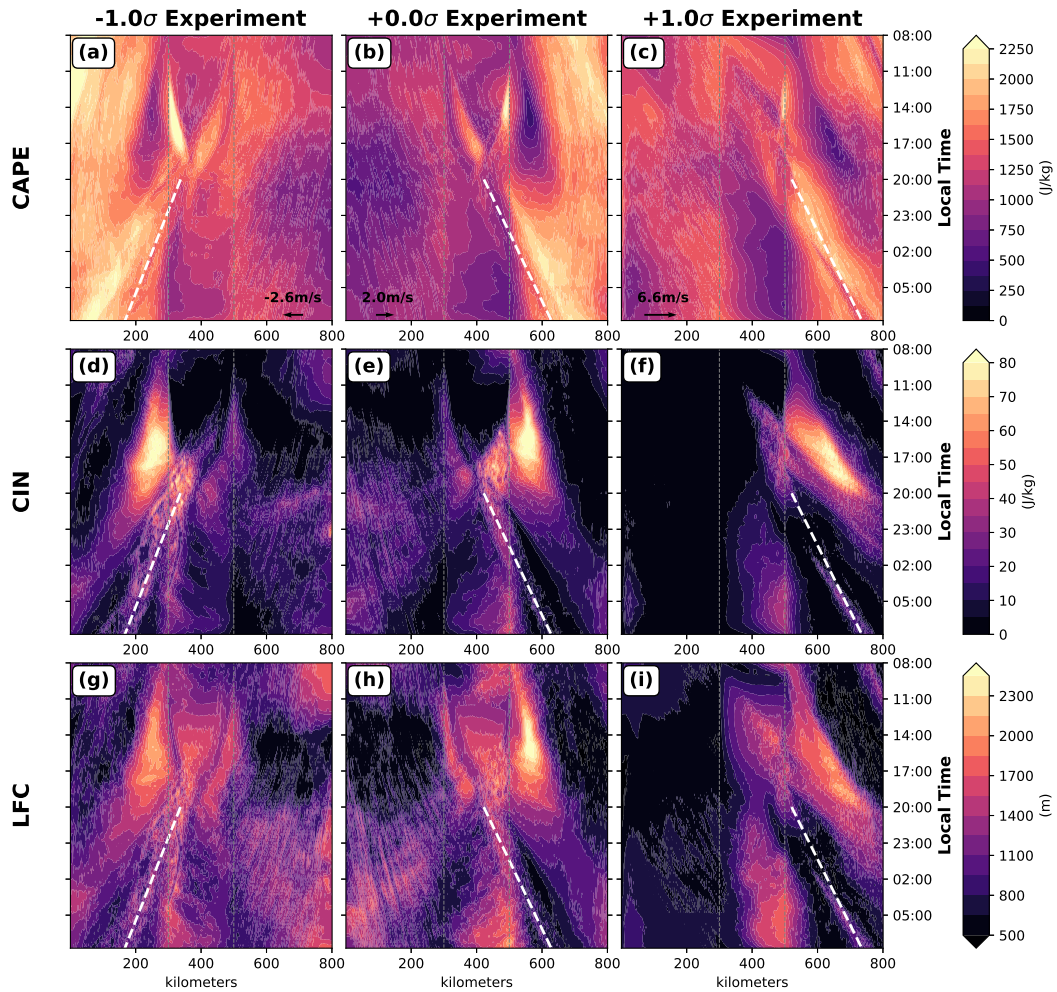


**Figure 3.11:** Perturbation potential temperature (K) for the second day of the  $0.0\sigma$  experiment in color at (a) 2.0-km, (b) 4.0-km, (c) 6.4-km, and (d) 9.1-km. The black contour indicates 2 mm/hr precipitation rate on Day 2 and is the same in all panels. The base-state 850-hPa zonal wind is shown as a labelled vector in (a).

Since the higher order modes are difficult to see in the composites (not shown), we next discuss the evolution of some convective parameters that may be impacted by destabilizing gravity waves.

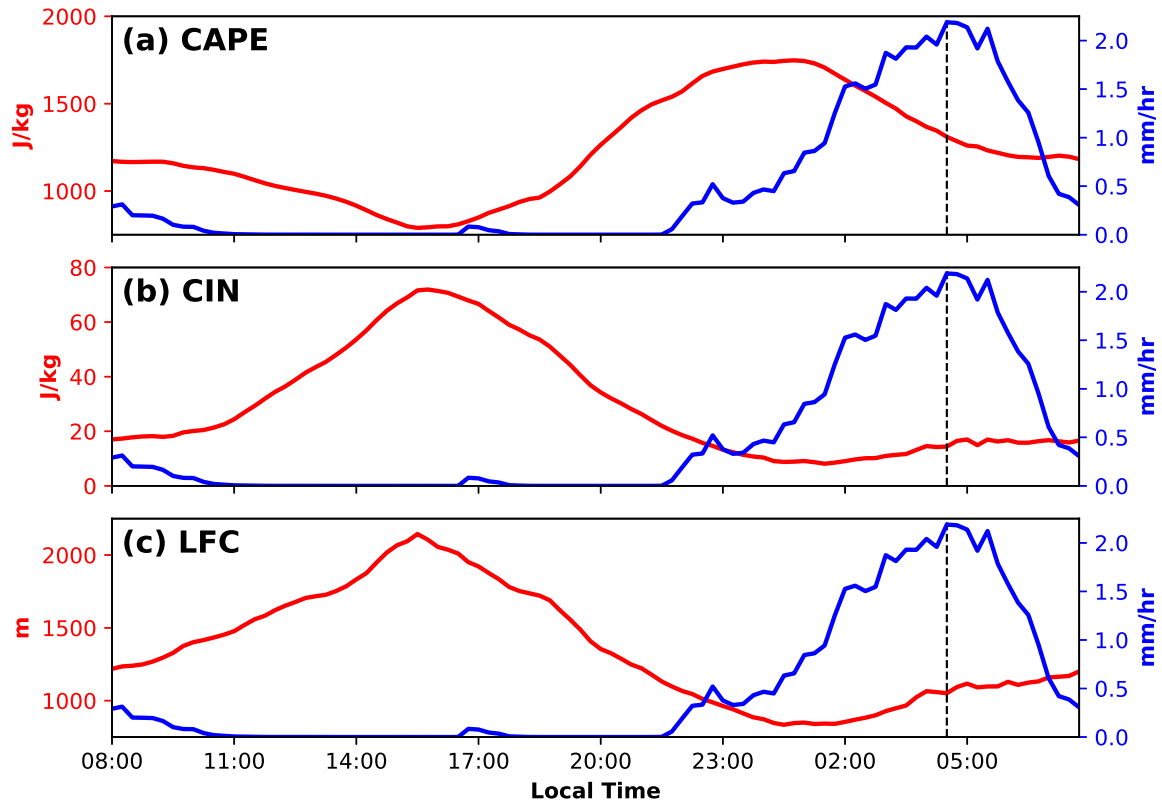
These parameters can better show the integrated effects of higher order modes that are difficult to see individually. Figure 3.12 shows 14-day composite convective available potential energy (CAPE), convective inhibition (CIN), and the level of free convection (LFC) for the  $-1.0\sigma$ ,  $0.0$ , and  $+1.0\sigma$  experiments. Destabilization, as indicated by an increase in CAPE, decrease in CIN, and decrease in the LFC is seen in the offshore environment in advance of the propagating convection (which is tracked roughly by the dotted white line). This behavior is visible on both sides of the island in all experiments, though more prominent on the side to which convection propagates. It is difficult to identify a single propagation speed associated with this destabilization, but there is gradual erosion of the stable offshore environment from about 20:00 through the time at which precipitation arrives.

Figure 3.13 captures this more directly by showing the thermodynamic parameters averaged from 500-600 km, or the nearest 100-km of ocean to the simulated east coast. The coastal environment is most stable in the late afternoon, with a minimum in CAPE and maximums in CIN and the LFC occurring around 15:00-17:00. After that, stability gradually decreases, with a subtle more rapid rate of change in each parameter visible around 20:00 when the convective to stratiform transition was observed (Fig. 3.10b). This region is at its most unstable around 23:00 to 02:00, just as precipitation rate starts to increase. We hypothesize that the integrated effects of higher order gravity wave modes contribute to this destabilization signal. However, gravity waves are initiated at different times each day and may vary in which heating mode triggers them (and thus vary in propagation speed). A direct coupling between a certain gravity wave mode and offshore propagating deep convection cannot be identified. In other words, gravity waves do not determine the direction or speed of propagation in this model, but do appear to be important for destabilizing the offshore environment. The propagation speed of precipitation (roughly 3-6 m/s; Fig. 3.7) is more consistent with a that of density current (Hassim et al., 2016; Ruppert and Zhang, 2019).



**Figure 3.12:** 14-Day composites from the  $-1.0\sigma$  experiment (left), the  $0.0\sigma$  experiment (middle), and the  $+1.0\sigma$  experiment (right) showing Hovmöller diagrams of convective available potential energy (CAPE, J/kg; top), convective inhibition (CIN, J/kg; middle), and the level of free convection (LFC, m; bottom), with local time starting at 08:00 increasing downwards. The line of best fit for the maximum precipitation rate shown in Fig. 3.7 for the corresponding experiment is shown as a dotted white line. The base-state 850-hPa zonal wind is shown as a labelled vector in each panel in the top row.

### +0.0 $\sigma$ Experiment: East Side Coastal Waters



**Figure 3.13:** 14-day composite CAPE (a; J/kg), CIN (b; J/kg), and LFC (c; m) averaged across the nearest 100-km of coastal waters on the eastern side of the simulated island in red, with composite precipitation rate (mm/hr) averaged in the same region in blue.

### 3.4.4 Direction of Propagation Sensitivity Experiments

In this section, the sensitivity of the direction of precipitation propagation to the details of the zonal wind profile will be considered. Fig. 3.7 shows that modeled precipitation exhibits clear westward propagation in  $-0.5\sigma$ , but clear eastward propagation in  $0.0\sigma$ . While the numerical difference between  $0.0\sigma$  and  $-0.5\sigma$  seems small, notable zonal wind profile differences between these two simulations exist (Fig. 3.2). Weak easterlies cover the entire profile in the  $-0.5\sigma$  base-state, while weak westerlies reach up to nearly 600-hPa in the  $0.0\sigma$  base-state. Thus, we considered several sensitivity experiments, each run for 7 days with the moisture and thermodynamics of the  $0.0\sigma$  experiment, but with adjustments made to the vertical structure of the zonal wind profile to assess the importance of flow at different levels to propagation of precipitation. Figure 3.14 shows the base-state zonal wind profiles for each of these experiments.

The zonal wind profile for the first set of 8 experiments is a linear interpolation between the wind profile in the  $-0.5\sigma$  experiment and the  $+0.0\sigma$  experiment, designed to test the depth of westerlies necessary to force eastward propagation. This set is labeled as sensitivity tests 1.1, 1.2, ..., 1.8 (where 1.1 is identical to the  $-0.5\sigma$  experiment and 1.8 is identical to the  $+0.0\sigma$  experiment). A second set of 8 experiments tests propagation with low-level westerly shear and an elevated layer of westerlies of varying depth. The goal of this set is to determine if eastward propagation can still occur with boundary layer background easterlies and elevated westerlies. If the set 1 profile is more westerly than extrapolation of a line connecting a 1000-hPa wind of  $-1$  m/s and an 900-hPa wind of  $0$  m/s the wind is set to the value of the extrapolated line instead. This new profile is labeled as 2.1, 2.2, ..., 2.8 and is shown in Fig. 3.14b. A third set is based on profiles interpolated between the  $-1.0\sigma$  and  $0.0\sigma$ , but requires easterly shear in the lowest levels by extending the average shear between 800-hPa and 850-hPa of the original profile to the surface. This set is labeled as 3.1, 3.2, ..., 3.8 and is intended to test the importance of weak easterly shear in the boundary layer.

The color-coding of each profile in Fig. 3.14 indicates the propagation velocity of maximum precipitation in the sensitivity tests, with red colors indicating eastward propagation, and blue colors indicating westward. The gray profiles either had visible propagation in both directions, or

**Propagation Direction Sensitivity Experiments:  
Base-State Zonal Wind Profiles**

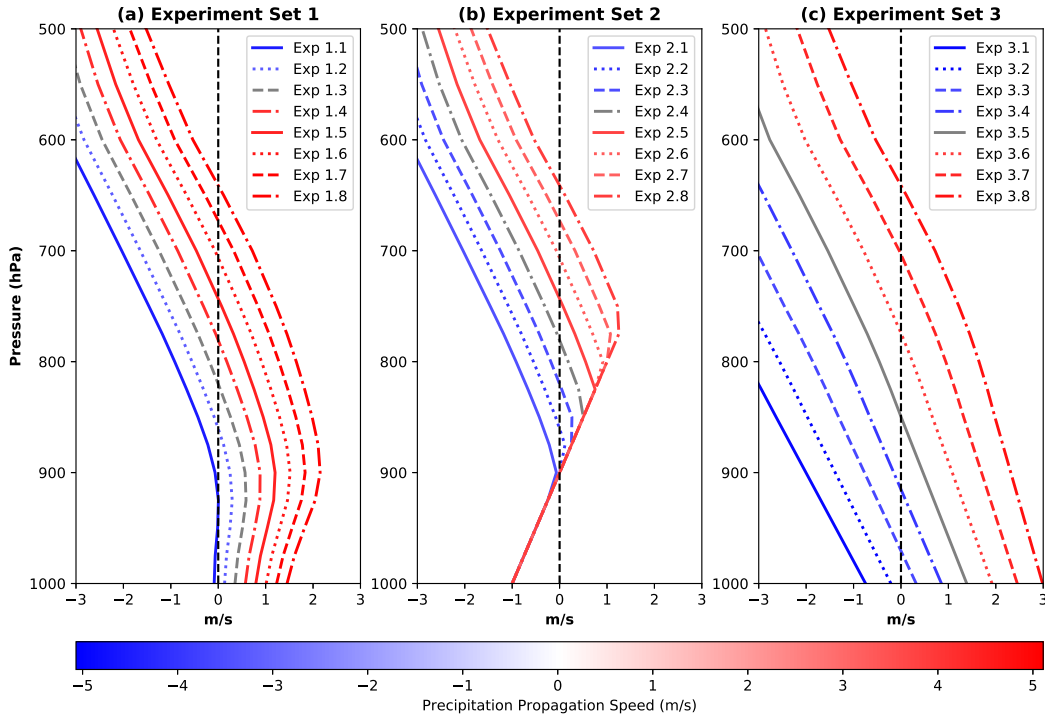


**Figure 3.14:** (a) Idealized base-state zonal wind profiles in the lower troposphere for sensitivity experiments set 1, based on linear interpolation between the  $-0.5\sigma$  and  $+0.0\sigma$  experiments shown in Fig. 3.2a. (b) As in (a) but for sensitivity experiments set 2, which are taken from set 1, but forced to a line (in pressure-wind coordinates) connecting a wind of  $-1$  m/s at 1000-hPa and  $0$  m/s at 900-hPa if the set 1 profile is more westerly than the ideal line profile at a given height. (c) As in (a) but for sensitivity experiments set 3, which are interpolated between the  $-1.0\sigma$  and  $0.0\sigma$  experiments, with the shear profile between 800-hPa and 850-hPa extended to the surface. Profiles are color coded by the propagation velocity of the smoothed (to 5-km spacing) maximum precipitation rate between 20:00 and 08:00 in each experiment, with red indicating eastward propagation, and blue indicating westward propagation. The gray profiles are chosen subjectively as experiments with weak or inconsistent offshore propagation in which the objective algorithm to calculate propagation speed failed.

unclear propagation that caused the objective algorithm to fail. In each set, the system propagates to the east once westerlies extend deeper than about 800-hPa, regardless of the low-level shear. It is worth noting that the shear used here is significantly weaker than many studies that specifically examine the impact of shear on convective organization and propagation (e.g. Rotunno et al. 1988; Nicholls et al. 1988; Liu and Moncrieff 1996; Carbone et al. 2000). Since the shear is weak, other processes are likely more important for determining propagation (Grant et al., 2020). Moreover, the speed of propagation is generally between 3 and 5 m/s in either direction for all simulations, although the environmental wind is only greater than 3 m/s below 600-hPa in a handful. Westerly environmental winds of greater than 3 m/s are found nowhere in any profile. Thus, it is unlikely that the precipitation propagation seen in the model is simply advection by the wind. Rather, these are propagating disturbances that move faster than the environmental wind (Lafore and Moncrieff, 1989).

Figure 3.15, which shows the zonal wind averaged within 25-km of the smoothed precipitation maximum between 17:00 and 20:00, indicates that eastward propagating experiments have fairly well-mixed westerly winds between 900-hPa and 700-hPa, with the converse in the westward propagating experiments. Winds in the PBL appear to not strongly influence propagation. We hypothesize that convective mixing distributes horizontal momentum through roughly the 700-900hPa layer, which then determines the propagation direction. Prior observational and modeling results add support to this hypothesis. LeMone et al. (1984) used aircraft and radiosonde data to show that tropical convective lines increase the rear-to-front momentum in the lower troposphere through vertical mixing. Fig. 3.15 shows that the uniformly distributed 700-900hPa momentum is generally rear-to-front. Observations by Keenan and Carbone (1992) indicated that monsoon-break season squall lines appeared to propagate in the direction of the 700-hPa winds. Peters and Hohenegger (2017) noted that convection initially propagates in the direction of the background wind (vertically unidirectional in their experiments), but the speed can be attributed to density current dynamics, which may explain why the propagation speed is relatively consistent in our experiments.

**Zonal Wind Profiles averaged from 17:00-20:00  
within 25-km of Precipitation Maximum**

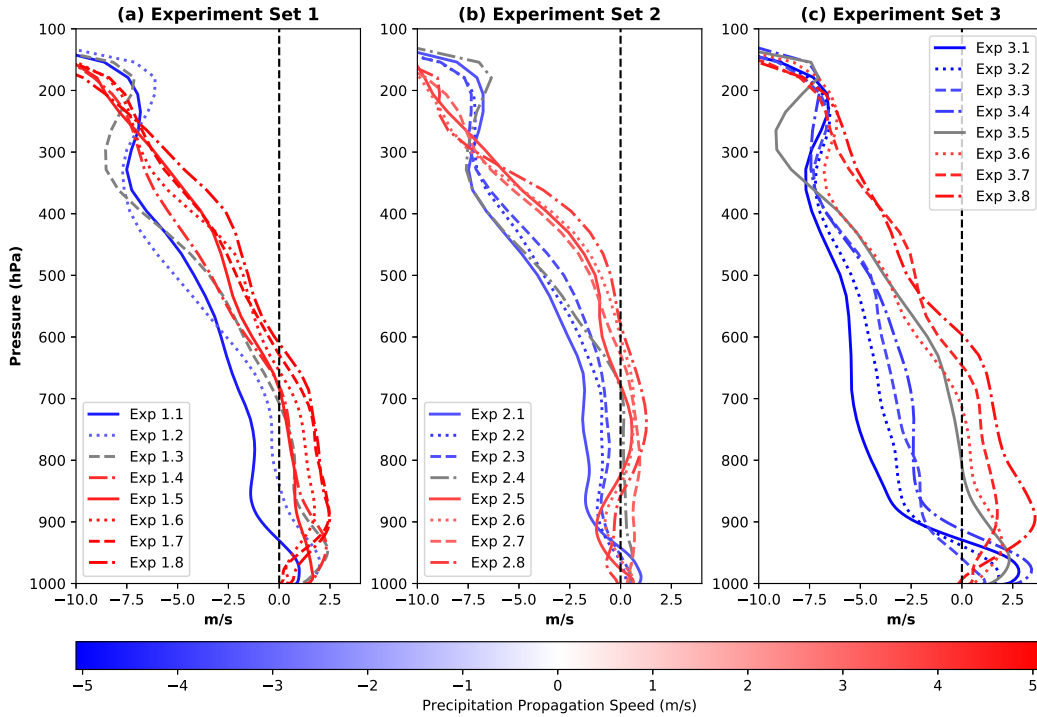


**Figure 3.15:** (a) Zonal wind profiles averaged from 17:00-20:00 within 25-km of the average location of maximum precipitation between 17:00 and 20:00 in the composite, for sensitivity experiments set 1. (b) As in (a) but for sensitivity experiments set 2. (c) As in (a) but for sensitivity experiments set 3. Profiles are color coded by the propagation velocity of the smoothed (to 5-km spacing) maximum precipitation rate between 20:00 and 08:00 in each experiment, with red indicating eastward propagation, and blue indicating westward propagation. The gray profiles are chosen subjectively as experiments with weak or inconsistent offshore propagation in which the objective algorithm to calculate propagation speed failed.

While the flow in the lower free-troposphere appears to be important for determining propagation direction, the PBL background flow is likely important for determining where within the island the heaviest precipitation falls. Figure 3.16 shows a scatter-plot of the average x-coordinate of maximum precipitation rate between 17:00 and 20:00 with the base-state wind at 0.68-km for each of the 24 sensitivity tests. This level yields the highest correlation coefficient of 0.97, which drops off to 0.84 when the lowest model level wind is used, and to 0.69 with the 1.98-km wind. The correlation coefficient of the location of maximum precipitation rate with the average wind in the roughly 700-900-hPa layer is 0.78. Thus, the PBL background flow appears to modify the speed of the sea-breeze fronts, and lead to their convergence on the leeward side of the island, consistent with Carbone et al. (2000). The variability in the location of maximum precipitation rate in experiment Set 2 shows roughly the amount of random spread that could be expected, since all of these have the same low-level wind but the location of maximum precipitation still varies inconsistently with the wind aloft. Carbone et al. (2000) also proposed that the ideal condition for long-lived diurnally forced convection is a flow-reversal in the lower free troposphere, such that surface winds are in opposition to the low-level shear vector. In such an environment, storms could initiate on the leeward side of the island (relative to the low-level wind) and then propagate entirely across the island, which occurred in our experiments 2.5-2.8 (not shown).

### **3.5 Conclusions**

This study has explored the impact of the environmental wind profile associated with different states of the monsoon-background on the diurnal cycle of precipitation. We have used Luzon Island in the northern Philippines as an observational test case to compare idealized modeling results of a 200-km wide island. It is shown that consideration of the environmental wind alone can explain many features in the observed variability of the diurnal cycle. These results complement the findings of many prior studies exploring the link between the diurnal cycle and large-scale modes of variability such as the MJO (e.g. Vincent and Lane 2016; Natoli and Maloney 2019; Short et al. 2019; Riley Dellaripa et al. 2020; Sakaeda et al. 2020), and also add to the general

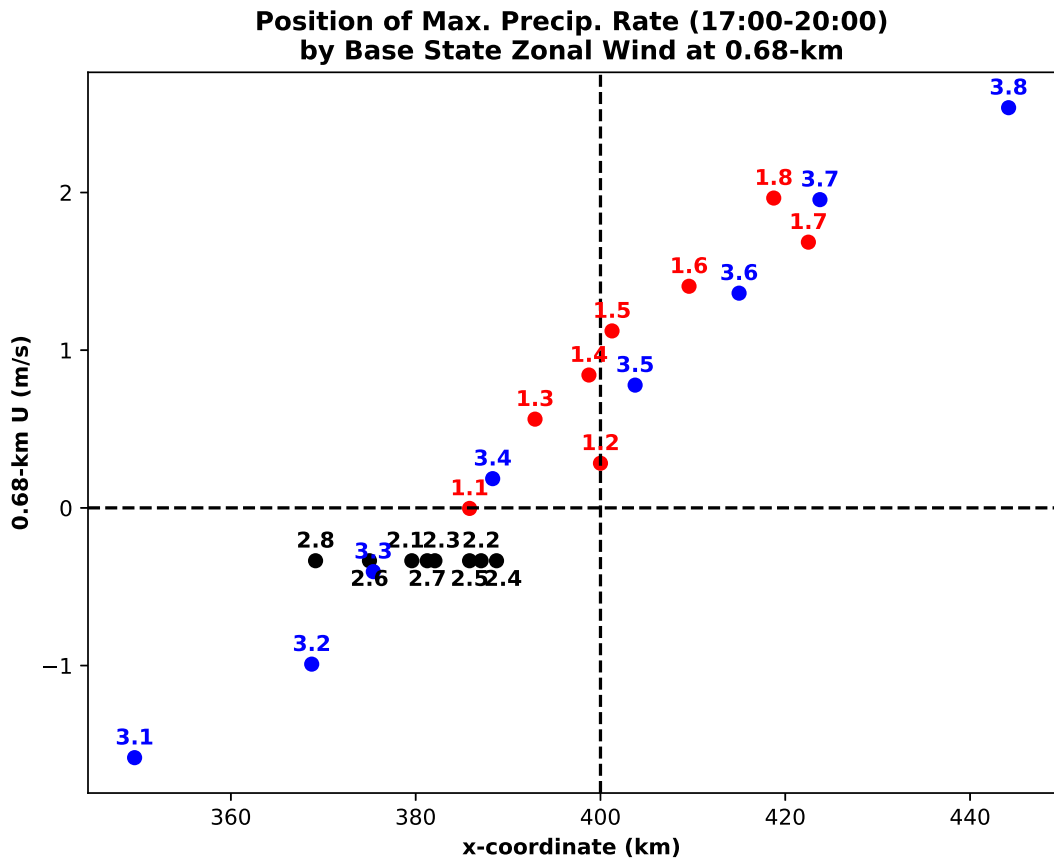


**Figure 3.16:** The average longitudinal position of the maximum precipitation rate (after smoothing to 5-km spacing) between 17:00 and 20:00 is shown on the x-axis (in kilometers), with the base-state zonal wind (in m/s) at the 0.68-km above the surface on the y-axis. Dotted black lines indicate the center of the island (vertical) and 0 m/s (horizontal). The dots are color-coded by experiment set, with Set 1 in red, Set 2 in black, and Set 3 in blue.

understanding of the diurnal cycle and offshore propagation of convection (Hassim et al., 2016; Kilpatrick et al., 2017; Yokoi et al., 2017, 2019). The main findings of this study are summarized as follows:

- Observed composite diurnal cycles conditioned on the environmental wind alone can capture distinct variability in diurnal cycle behavior. Strong diurnal cycles tend to occur with weak, offshore prevailing wind (Fig. 3.4b-f). Strong wind in either direction appears to be associated with a suppressed diurnal cycle (Fig. 3.4a,g).
- While westward propagation of diurnally generated convection is apparent in an observed composite of all days in the JJAS monsoon season (e.g. Natoli and Maloney 2019; Lee et al. 2021), this occurs primarily on days with the background wind more easterly than average (-1.5, -1.0, -0.5 $\sigma$  bins in Fig. 3.5a-c).
- A simple, 2-D idealized simulation using CM1 can replicate the direction of propagation and qualitative strength of diurnally generated convection as impacted by the background wind that is seen in observations (Figs. 3.5 and 3.7)
- Strong background winds can ventilate the land surface and reduce the land-sea contrast, particularly on the windward side of the island, and greatly reduce the sea-breeze strength (Figs. 3.8 and 3.9). A sea-breeze can still be identified on the leeward side of the island, but even this is reduced under the strongest winds.
- Propagating gravity waves of several different vertical modes are observed in these simulations (Figs. 3.10, 3.11). These may contribute to destabilization of the offshore environment and thus make offshore propagation more likely, but evidence of direct coupling between offshore propagating convection and a specific gravity wave mode is lacking (Figs. 3.11 and 3.12).

- Convection propagates offshore during the overnight hours in the direction of the wind between 700-900-hPa, but moves at a speed of 3-6 m/s, consistent with density current speeds (Figs. 3.7 and 3.14).

These results improve understanding of the large-scale controls on the diurnal cycle in and near tropical islands, and are applicable to the study of the MJO/BSISO-diurnal cycle relationship. We have shown that the background wind alone can explain several aspects of diurnal cycle variability attributed to the MJO. For example, the direction of offshore propagation appears to be determined by the wind in the lower free-troposphere (Figs. 3.7 and 3.14), consistent with Ichikawa and Yasunari (2006, 2008), Fujita et al. (2011), and Ruppert and Zhang (2019). Light, offshore winds appear to be associated with the strongest diurnal cycles both in observations (Fig. 3.4) and our idealized CM1 simulations (Figs. 3.7 and 3.2), favoring strong diurnally generated convection on the leeward side of an island (Fig. 3.16). This supports findings by Virts et al. (2013), Natoli and Maloney (2019), Sakaeda et al. (2020), and Qian (2020), among others, who have identified heavy diurnal precipitation during the transition from suppressed to active MJO state, particularly on the west side of large islands (which is in the lee before the westerly wind burst arrives later in the active phase). The reduction in land-sea contrast shown in Fig. 3.9 supports the hypothesis that the onshore wind during active phases of the MJO is an important reason why the diurnal cycle is suppressed (Short et al., 2019; Yokoi et al., 2019).

It is worth noting that many of these features from observations can be described in a 2-D model without topography. This is consistent with recent work that has suggested that topography is not vital in determining qualitative behavior of diurnally generated convection, although it can modestly increase the intensity of precipitation and modulate the timing of the diurnal cycle (Riley Dellaripa et al., 2020; Ruppert et al., 2020). Topography may also alter the precise location where convection forms on the island through interactions with the propagating sea breeze.

We have shown that prevailing wind speed and direction is vital to understanding the large-scale controls on tropical island diurnal cycle behavior, and the wind alone can explain many aspects of the widely studied MJO-diurnal cycle relationship. However, we have not yet addressed the effects

of other aspects of the environment modulated by large-scale modes of variability. Model sensitivity tests are ongoing to explore the contributions of several environmental background conditions, such as the ambient moisture and morning insolation, to diurnal cycle variability on tropical islands such as Luzon. We expect this will provide additional insight on the importance of the background wind relative to other variables in determining the behavior of the diurnal cycle on tropical islands and its offshore propagation.

## Chapter 4

# The Mechanisms Involved in the Modulation of the Tropical Island Diurnal Cycle by the Boreal Summer Intraseasonal Oscillation<sup>3</sup>

### 4.1 Introduction

In the prior two chapters, compelling hypotheses have been developed that aim to explain the observed variability in the tropical diurnal cycle. In Chapter 2, it was shown that the QBWO impacts the diurnal cycle near Luzon island very similarly to the BSISO, and that the similar modulation of the local environment by both modes could explain this. In Chapter 3, we highlighted the critical importance of the background wind profile regardless of timescale on which the wind varies in determining diurnal cycle behavior. What remains, however, is to tie these results back to the original goal that inspired this work. Specifically, we must conclusively show that the response of the local diurnal cycle to a BSISO event identified by Natoli and Maloney (2019) (or conversely, Peatman et al. (2014) for the wintertime MJO) can be explained by the modulation of the local environmental wind, moisture, and insolation. Thus, this chapter will return the focus to the BSISO to show that the presence of light easterly winds, increasing ambient moisture, and sufficient insolation in the transition from BSISO suppressed to active conditions leads to a strong, offshore propagating diurnal cycle on the western shore of MC islands.

We will test the previously stated hypothesis through a rigorous, probabilistic analysis of observation data and tightly controlled idealized model simulations. In the next section, we will outline the datasets and methods employed, as well as provide a detailed description of the model setup. The observational results will be discussed in Section 3 through a probabilistic framework that

---

<sup>3</sup>This chapter contains material that will soon be submitted for publication in *Journal of Climate*.

includes the range of conditions possible within a certain BSISO phase in order to understand how certain BSISO phases make environmental conditions that favor a strong diurnal cycle more likely. In Section 4, numerous model simulations using 3D Cloud Model 1 designed to explicitly test our hypothesis will be discussed. These simulations will adjust the base-state according to BSISO composite profiles, and then attempt to isolate the environmental conditions responsible for the observed BSISO modulation of the diurnal cycle. Additional simulations explore the importance of the island size, as well as precipitation behavior in the absence of a diurnal cycle. Lastly, the main conclusions and implications of these results will be explained in Section 5.

## **4.2 Data and Methods**

### **4.2.1 Observations**

Satellite observations and reanalysis are studied for the period of July-September (JJAS) 1998-2020. Precipitation estimates from version 1.0 of the bias-corrected Climate Prediction Center Morphing Technique (CMORPH; Joyce et al. 2004; Xie et al. 2017) are derived from multiple satellites and are available at 8-km spatial and 30-minute temporal resolution. Reanalysis data from the 5th Generation Reanalysis by the European Center for Medium Range Weather Forecasting (ERA5; Copernicus Climate Change Service (C3S) 2017; Hersbach et al. 2020) is used at 0.25° spatial and hourly temporal resolution for both observational analysis and driving the model described below. Variables examined on pressure levels from 1000-hPa to 100-hPa include zonal wind, specific humidity, geopotential height, and temperature. Total column water vapor (TCWV) and surface downward shortwave radiation (insolation) are also analyzed. Additional ERA5 variables are used in the model setup and are described below. Topographic information from the NOAA ETOPO2 dataset (National Geophysical Data Center, 2006) provide geographical context for the observational results.

CMORPH precipitation and ERA5 vertical profiles are composited based on the phase of the BSISO as defined by Lee et al. (2013), which is constructed from the first two multivariate EOFs of outgoing longwave radiation and 850-hPa zonal wind during boreal summer in the Asian mon-

soon region. Days in JJAS are only included in the composite if the amplitude of the BSISO index was greater than 1.0, and then data are partitioned into one of eight phases. The distribution of the CMORPH precipitation diurnal cycle amplitude among all days in the study period is frequently referenced as a baseline. The diurnal cycle amplitude (DCA) is defined in this study as the difference between the daily maximum spatially averaged precipitation rate and the daily minimum spatially averaged precipitation rate. This is done for six averaging domains inside boxes A-F shown in Figure 4.1. Thus, a DCA is found for each box, for each of the 2806 days in JJAS 1998-2020. The 85th percentile DCA is calculated for each box as a proxy for a day on which a strong precipitation diurnal cycle was observed. Other percentile thresholds were also considered, and the 85th percentile was found to be an appropriate balance between capturing only the most significant diurnal cycle events, while also retaining a substantial sample size. Days on which the DCA exceeded the 85th percentile in each box are referred to as 85th percentile diurnal cycle amplitude (DCA85) days. Note that specific dates included in the DCA85 group will be different for each averaging box.

## **4.2.2 CM1 Setup**

### **Control**

Idealized modeling experiments are conducted using version 20.2 of Cloud Model 1 (CM1; Bryan and Fritsch 2002) in order to examine the sensitivity of diurnal cycle behavior to the BSISO base-state, and the sensitivity to single environmental variables in isolation. The fairly low computational cost of this model facilitates the numerous experiments discussed in this manuscript. The model is run at 1-km horizontal grid spacing with a domain size of 800-km zonally, 60-km meridionally, and 20-km vertically. The high horizontal resolution allows for explicit simulation of convection. A stretched vertical grid is used, with grid spacing of 50-m in the boundary layer, increasing to 1150-m at the model top. In each experiment, the model is iterated for 7-days, with output saved every 30-minutes.

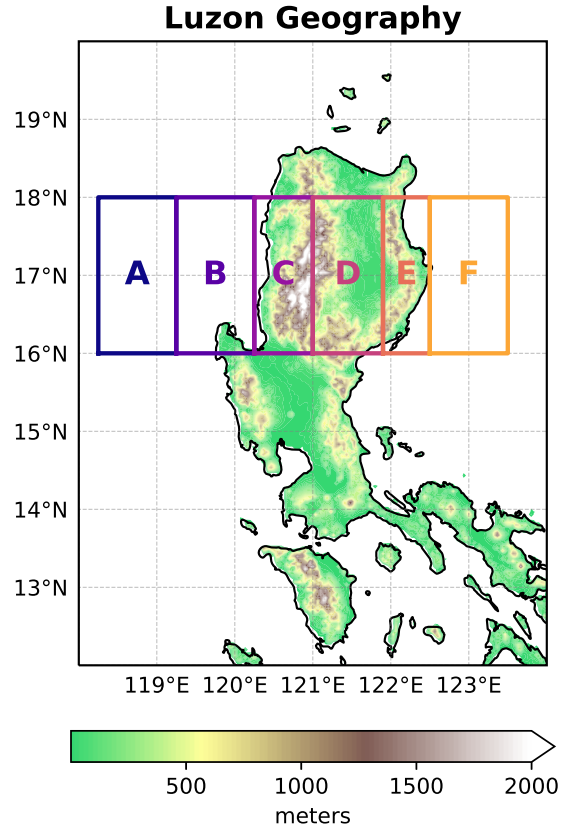


**Figure 4.1:** (a) NOAA ETOPO2 Topography (in meters) over the northern Philippines, overlaid with boxes of spatial averaging used in this study.

Boundary conditions are open radiative on the east and west boundaries, periodic at the north and south boundaries, free-slip at the top boundary, and partial-slip (includes a coefficient of friction) at the bottom boundary. To simulate the diurnal cycle in initial experiments, a 200-km wide island (roughly the width of Luzon island between 16-18°N as shown in Fig. 4.1) is placed at the center of the domain. The island is uniform in the meridional direction, which makes this more of a quasi-3D simulation. The physical setup is similar to Wang and Sobel (2017), and allows for the advantages of 3D cloud dynamics while easing analysis and maintaining a fairly small domain to reduce computational cost. Topography is not included in these simulations for simplicity. Riley Dellaripa et al. (2020) simulated the diurnal cycle over Luzon in a convection permitting regional model, and showed that results are qualitatively similar when topography is removed, which justifies this choice.

The base-state for each simulation comes from ERA5 vertical profiles averaged inside the region spanning boxes A-F (Fig. 4.1). The control simulations in this study are a set of 8 simulations with the base-state varying with the BSISO composite environmental profile. The background zonal wind and anomalous moisture profiles used in each of these simulations is shown in Figure 4.2. In addition to moisture and zonal wind, the BSISO composite temperature profile is also varied along with values of MSLP and T2m. Initial surface conditions come from the ERA5 sea surface temperature (SST) and the ERA5 skin temperature from land points below 400-m in elevation. The land surface temperature is allowed to evolve freely, while the SST is fixed at the ERA5 mean value of 302.5K. The model is initialized with insolation corresponding to 05:00 Local Time (LT) at 17°N on 1 August.

The following parameterizations are utilized: a revised surface scheme from the Weather Research and Forecasting (WRF) model (Jiménez et al., 2012), the Yonsei University planetary boundary layer (PBL) scheme (Hong et al., 2006), the Morrison double moment microphysical scheme (Bryan and Morrison, 2012), and the NASA-Goddard radiation scheme adapted to CM1 from the Advanced Regional Prediction System model. A Rayleigh damping layer is applied above 15-km with an e-folding timescale of 5 minutes. The base-state is maintained through two meth-

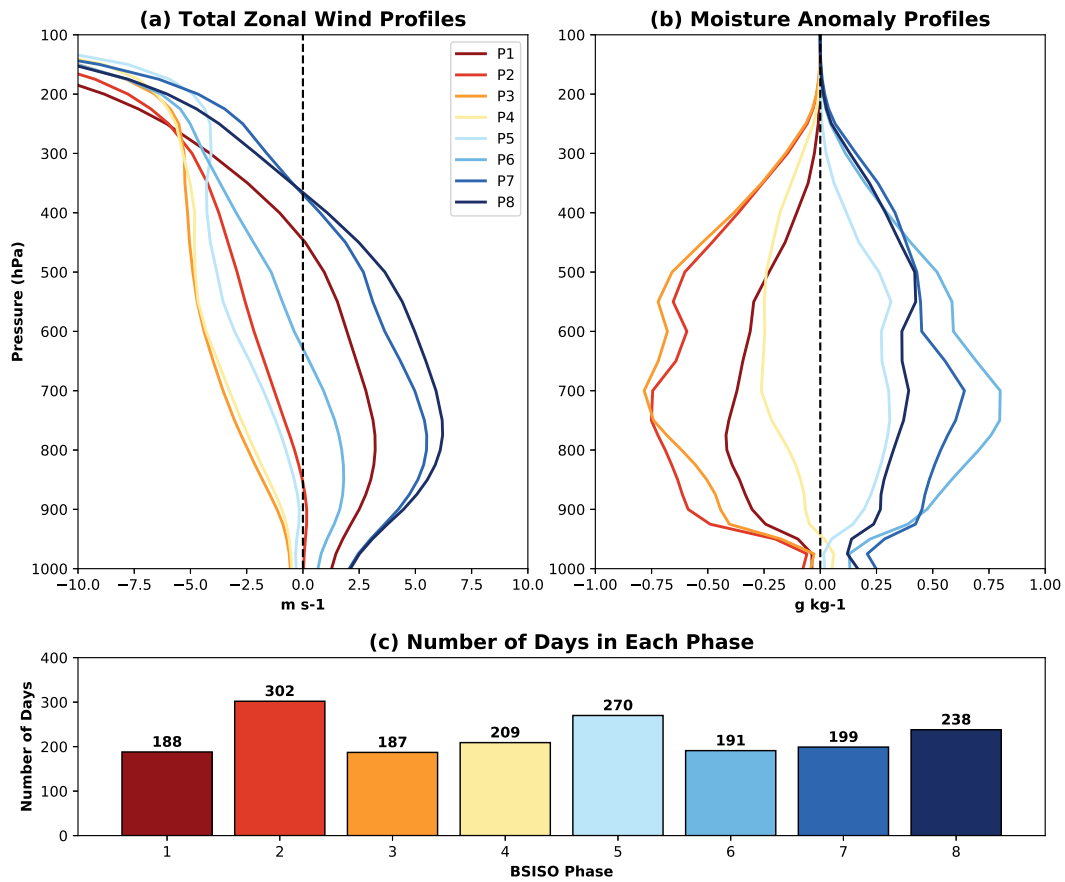


**Figure 4.2:** (a) Composite ERA5 zonal wind profiles (m/s) for each BSISO Phase in JJAS 1998-2020. Values are averaged inside Boxes A-F together (Fig. 4.1a). (b) Anomalous moisture profiles in g/kg by BSISO Phase. (c) The number of JJAS 1998-2020 days that fall into each bin is shown as bars, with this number noted on top.

ods. First, the inflow at the lateral boundaries is nudged towards the base-state with a timescale of one minute. Second, a large-scale nudging technique is applied, in which the domain mean at each vertical level is nudged back to the base-state with a timescale of 3 hours. This timescale was found to be a relatively good balance between preventing progressive divergence from the base-state late in the simulation and free evolution of the model diurnal cycle.

### **Sensitivity Experiments**

The first group of sensitivity experiments alters the model base-state to isolate the impacts of ambient moisture, lower tropospheric wind, and insolation on the diurnal cycle. These three variables are often invoked to explain the BSISO-diurnal cycle relationship (e.g. Chapter 2, Vincent and Lane 2017; Natoli and Maloney 2019; Sakaeda et al. 2020; Peatman et al. 2021). In all experiments in this study, very small random perturbations are applied to the initial condition to introduce some 3D inhomogeneity. The first eight simulations of this group titled BSISO Wind Only are designed to examine diurnal cycle behavior attributable to the wind anomalies associated with different BSISO phases, in the absence of other confounding factors. In these experiments, only the BSISO composite zonal wind profile is used in the model base-state, while the JJAS mean vertical profiles are used for all other variables.

Moisture experiments contribute an additional 8 sensitivity tests. The base-state moisture is varied across 4 levels while the temperature profile comes from the JJAS mean. Each moisture level is run twice, once with BSISO phase 3 composite winds (light to moderate easterlies), and once with BSISO phase 7 composite winds (strong westerlies), yielding a total of 8 simulations. The highest moisture experiment ( $+1.5\sigma$ ) uses a moisture profile from a composite of JJAS days in which the TCWV was between 1.25 and 1.75 standard deviations above the JJAS mean. Next, we use BSISO composite phase 7 moisture (P7), followed by BSISO composite phase 3 moisture (P3) profiles (Fig. 4.2b). The driest ( $-1.5\sigma$ ) comes from days on which TCWV was between 1.25 and 1.75 standard deviations below the JJAS mean. Note that the P7 moisture experiment with Phase 7 winds is very similar to the control experiment, but not identical, only varying in the temperature

profile which comes from the JJAS mean in the moisture experiments compared to the BSISO composite in the control.

Another set of simulations attempts to test the impact of insolation on the diurnal cycle. Here, the solar constant ( $S_0$ ) is altered to 115%, 85% and 70% of its actual value. Analysis of ERA5 surface downwelling shortwave radiation (not shown) indicates an approximate 15% increase or decrease in insolation in the driest or wettest BSISO phases respectively compared to the JJAS mean. The 70%  $S_0$  experiment tests a more extreme scenario. All other aspects are identical to the control simulations, but only the BSISO Phase 3 and BSISO Phase 7 base-states are tested, yielding six total Solar experiments. The resulting simulations are not exactly how the BSISO would impact insolation in the real atmosphere. The general hypothesis is that the diurnal cycle is more active in the BSISO suppressed state because of increased cloud cover, which reduces incident surface solar radiation, the land-sea temperature contrast, and thus the sea-breeze circulation (Peatman et al., 2014; Birch et al., 2016; Wu et al., 2018; Natoli and Maloney, 2019). However, a stable change in cloud cover in this idealized model could not be forced. In our model, insolation is altered at the top of atmosphere (TOA), rather than at the surface as in the real atmosphere. Caveats of this method are discussed below, but this set can qualitatively test the response of diurnally driven precipitation to radiation variations.

### **Island Size Experiments**

In addition to exploring the impact of various base-state on diurnal cycle behavior, the importance of the choice of island size to the results described below is addressed. An additional eight simulations alter the size of the landmass in the center of the domain from the 200-km in the control simulation. Two smaller islands are tested, with widths of 25-km and 100-km. Two larger islands of 400-km and 800-km are also tested, and the domain size is increased to 1600-km in these since the coastline would be close enough to the model boundary to contaminate the results if an 800-km domain was used. As in the Moisture and Solar experiments, each island-size experiment is run twice, once with the BSISO Phase 3 base-state, and once with the BSISO Phase 7 base-state.

## No Diurnal Cycle Experiments

Lastly, the precipitation behavior in this model setup in the absence of a diurnal cycle was explored. To accomplish this, some basic alterations to the radiation scheme were made. First, the solar constant was changed to  $444.1 \text{ W/m}^2$ , which is the daily averaged TOA incident radiation at  $17^\circ\text{N}$  on August 1 1979-2020 from ERA5. The solar zenith angle is fixed at  $0^\circ$ . The result is temporally uniform shortwave radiation nearly equal to the daily mean of the control simulation. It is worth noting that this is not perfectly equivalent to the daily averaged effects of insolation, since the albedo varies as a function of zenith angle. This is done for each of the eight BSISO composite base-states. Additionally, the island-size experiments are repeated without a diurnal cycle as described above, but with Phase 2 and Phase 6 base-states (since Phase 7 produced no precipitation without a diurnal cycle as will be discussed below).

A brief summary of each of the 54 simulations described in this study is shown in Table 1.

**Table 4.1:** Summary of CM1 simulations examined in this study.

Title of Set	Number in Set	Parameter Altered
Control	8	Base-State Profile (All Variables)
Wind Only	8	Base-State Wind Profile
Moisture	8	Base-State Moisture Profile
Solar	6	Solar Constant ( $S_0$ )
Island-Size	8	Width of Central Island
No-Diurnal	8	Control Experiments with Constant Insolation
Island-Size/No-Diurnal	8	Island-Size Experiments with Constant Insolation

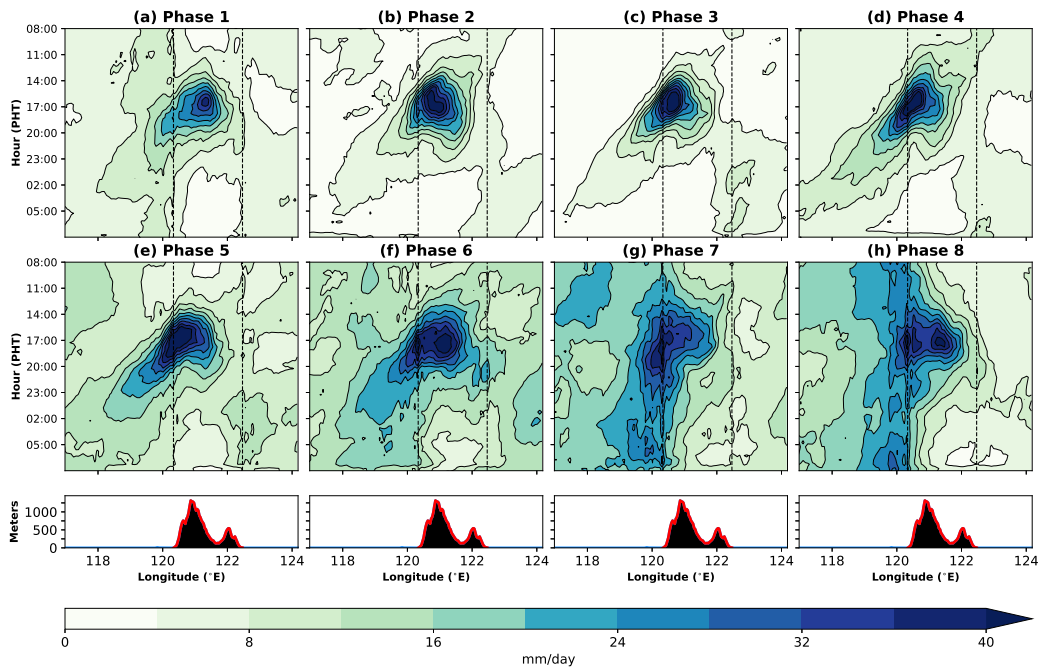
## 4.3 Observations

The goal of this section is to clearly elucidate the environmental background conditions associated with high amplitude diurnal cycles near Luzon island. While most studies evaluating the relationship between the MJO/BSISO and the diurnal cycle approach the problem through composites of precipitation based on the large-scale feature (e.g. Rauniyar and Walsh 2011; Peatman

et al. 2014; Lu et al. 2019; Natoli and Maloney 2019, among others), a reverse approach is taken here. In particular, we highlight the days on which a high amplitude diurnal cycle occurs, and identify the anomalous environmental conditions associated with these days. It is then demonstrated that certain BSISO regimes make specific configurations of local environmental background conditions that favor strong diurnal cycles significantly more likely. This analysis utilizes a probabilistic approach towards the understanding of ISO-diurnal cycle interactions.

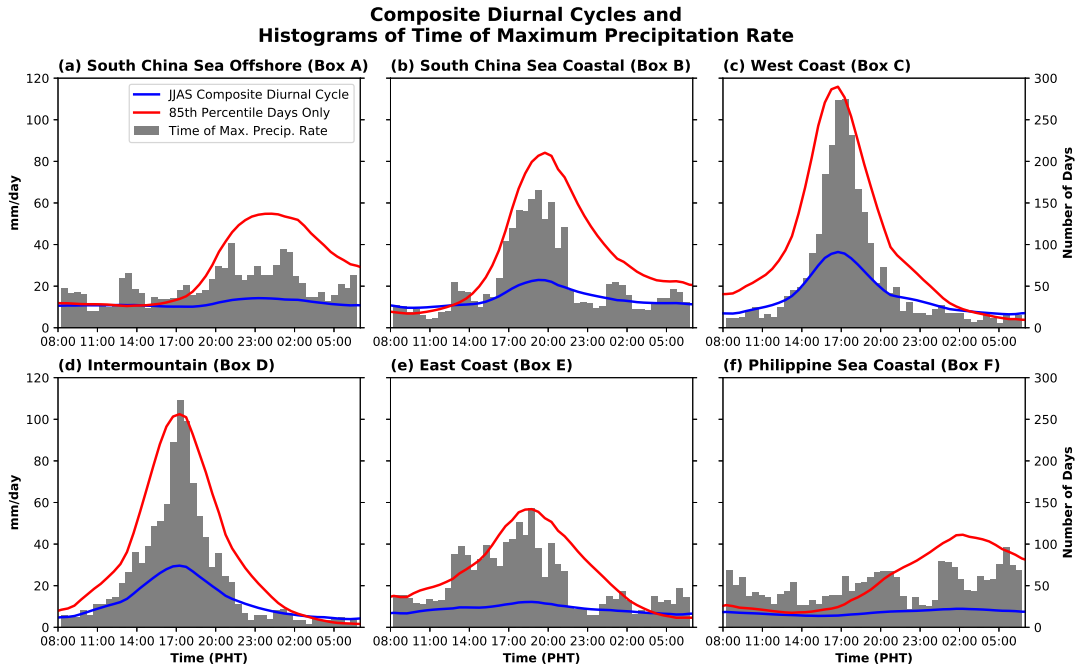
A more thorough analysis of the impact of the BSISO on the Luzon diurnal cycle can be found in Natoli and Maloney (2019), but is briefly reviewed here. Figure 4.3 shows Hovmöller diagrams of composite diurnal cycles of CMORPH precipitation estimates by Lee et al. (2013) BSISO phase. We note that Fig. 4.3 is very similar to Fig. 7a of Natoli and Maloney (2019), but not identical since we restrict our study here to JJAS rather than May-October. This is averaged across the latitudinal domain of boxes A-F in Fig. 4.1, but includes a slightly expanded longitudinal range. Convection initiates near the western shore in the mid to late afternoon, and exhibits westward offshore propagation into the South China Sea (SCS) in most phases. The diurnal cycle is much more pronounced in the suppressed BSISO phases (2-4), compared to the active phases (6-8). In particular, the transition from suppressed to active conditions through phases 3, 4, and 5 tends to exhibit the strongest diurnal cycles with the best westward propagation. This behavior has been tied to the combination of easterly wind anomalies and sufficient moisture and insolation that are concurrent in this transition (Chapter 2, Natoli and Maloney 2019). Chapter 3 also showed that westward propagation is highly sensitive to the background wind profile.

Figure 4.4 provides a closer look at the diurnal cycle in each of Boxes A-F in Fig. 4.1. Composite diurnal cycles spatially averaged inside each box are shown for all JJAS days in blue, while the composite for DCA85 days is shown in red. A histogram also shows the time at which the maximum daily precipitation rate occurs. The land boxes (top row) show a strong preference for the diurnal cycle to peak during the late afternoon, around 17:00, although it is more pronounced for the west (a) and center (b) of Luzon compared to the east (c). The coastal South China Sea (e) shows a significant preference for a diurnal cycle peak around 20:00, consistent with offshore



**Figure 4.3:** Hovmöller diagrams of CMORPH composite precipitation rate (mm/day) on JJAS days by Lee et al. (2013) BSISO index. Results are averaged across latitude inside Boxes A-F (Fig. 4.1a), but additional longitude to the west of Box A and the east of Box B is also included. Time starts at 08:00 local time in each panel, and increases downward. Vertical dotted lines show the position of each coastline. The average topography from NOAA ETOPO2 inside boxes A-F is shown at the bottom for reference.

propagation. While the histograms for the boxes further offshore (e.g. d and f) do not show a clear preference for the diurnal cycle to peak at a certain time among all JJAS days, filtering for only DCA85 days clearly shows a peak around midnight in Box A, and around 02:00 in Box F. It is likely that when a strong diurnal cycle is observed offshore, it is associated with convection that initiated over land in the late afternoon and then propagated offshore (Chudler et al., 2020).



**Figure 4.4:** The composite diurnal cycle of CMORPH precipitation (mm/day) averaged inside each box on all JJAS 1998-2020 days in Fig. 4.1 (blue line). The composite diurnal cycle only from days on which the amplitude of the diurnal cycle (as defined by the difference between daily maximum precipitation and daily minimum precipitation rate) is greater than its 85th percentile (red line). A histogram showing the number of days on which the maximum precipitation rate occurs in each half-hour bin (gray). The first (23:30-00:00 UTC or 07:30-08:00 Local Time) and last (00:00-00:30 UTC or 08:00-08:30 Local Time) bins are excluded since those bins capture days on which precipitation is either increasing or decreasing through the whole day due to longer time-scale features. The top row shows Boxes C-E, which include mainly land points, while the bottom row shows Boxes A, B, and F, which include mainly oceanic points.

The probability of observing a DCA85 day within a given BSISO phase for each subregion is shown in Figure 4.5. Since a DCA85 day has by definition a 15% chance of occurring, a relative change of +50% in Fig. 4.5 would indicate that given the BSISO is active in that specific phase, there is a 22.5% chance for a DCA85 day. On the west coast (c), there is a small increase in the

probability of a DCA85 day during phases 2 through 5, consistent the composite analysis (Fig. 4.3). Interestingly, the central and eastern portions of the island tend to have a reduced probability of a strong diurnal cycle during these phases. The east coast (e) exhibits higher probabilities for DCA85 days during phases 6-8. Offshore, each box (A, B, and F) is more likely to see a DCA85 day given the BSISO in phases 5 or 6, close to phases 4 and 5 which were identified by Natoli and Maloney (2019) with composite analysis as the phases with the most robust offshore propagation. The consistency between the east and west side of the island is somewhat surprising. However, based on the later timing of the diurnal cycle peak in Box F (Fig. 4.4f) and the discontinuous increase in precipitation off the eastern coastline in the Hovmöllers of Fig. 4.3e-f, we speculate that the diurnal cycle in the coastal Philippine Sea to the east of Luzon is driven by the land-breeze, independent from offshore propagation. It is also possible that this is completely independent from land, but rather related to the nocturnal peak found in previous studies over the open ocean (e.g. Gray and Jacobson 1977). The fact that strong diurnal cycles over the offshore box F occur on very different days from the east coast box E supports this hypothesis. Overall, the probabilistic results here are consistent with prior studies showing the preference for strong diurnal cycles during the suppressed BSISO phases over the west coast, with offshore propagation particularly favored during the transition from suppressed to active (Xu and Rutledge, 2018; Xu et al., 2021; Natoli and Maloney, 2019; Chudler et al., 2020).

Next, the environmental background conditions present on DCA85 days will be considered. Here, we examine a few fields from ERA5 averaged across boxes A-F (Fig. 4.1) to diagnose the larger-scale environment. Figure 4.6 shows histograms of three different variables hypothesized by prior studies (e.g. Vincent and Lane 2016; Yanase et al. 2017; Natoli and Maloney 2019; Short et al. 2019) to be important for modulating the local diurnal cycle. For the sake of brevity, the results for only two of the six boxes in Fig. 4.1 are examined. In each panel, the gray bars display the histogram of one environmental variable from all JJAS days. The colored bars superimposed show the distribution when only DCA85 days in the box (Coastal SCS/Box B for left column, East Coast/Box E for right column) are considered.

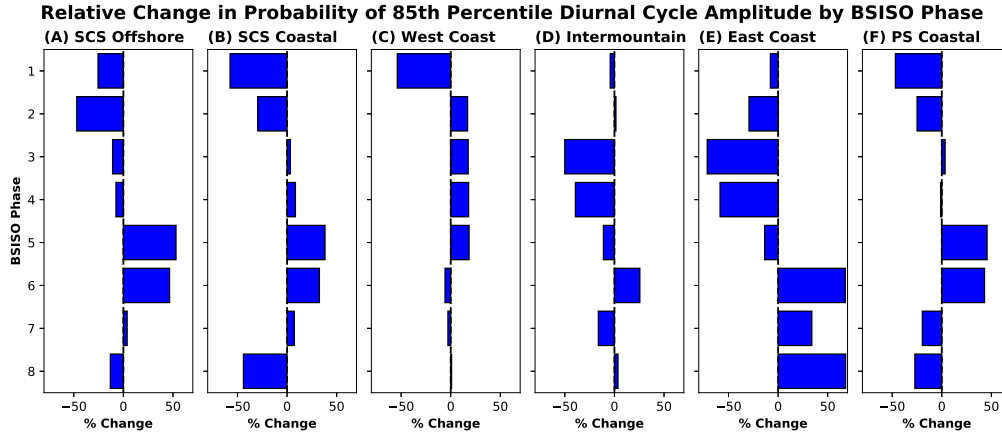


**Figure 4.5:** The relative change in the probability of an 85th percentile diurnal cycle amplitude day occurring in each box from Fig. 4.1 given a specific BSISO phase (y-axis). For example, if 30% of BSISO Phase X days showed a 85th percentile diurnal cycle amplitude in Box Y, it would display as a 100% increase, since 15% of all days can be expected to exceed the 85th percentile.

Stark stratification is seen in 850-hPa zonal wind ( $u_{850}$ ) (Fig. 4.6a,d). While the distribution from all JJAS days is fairly well centered around 0 m/s with a slight positive skew, DCA85 days in the Coastal SCS are strongly preferred with a weak easterly wind. While they can occur with a westerly wind, the probability is sharply reduced given the presence of a westerly wind in the lower troposphere. Conversely, DCA85 days on the East Coast are substantially *less* likely with an easterly wind, and become favored with a weak to moderate westerly wind. This indicates that a high amplitude diurnal cycle becomes much more likely given the presence of a weak to moderate offshore background wind. This supports the conclusions of Chapter 3, but the differing method used here accentuates the rarity of a strong diurnal cycle when unfavorable winds are present. Similarly conspicuous separation is apparent in TCWV. DCA85 days are much more likely in both boxes given a higher than average TCWV. This is unsurprising given previous studies that show a close correlation between precipitation and moisture in the tropics (e.g. Bretherton et al. 2004; Holloway and Neelin 2009, 2010; Kuo et al. 2017). Isolating the contributions of surface shortwave variations to the diurnal cycle is slightly more complicated. To reduce the influence of cloud cover induced by the diurnally generated convection itself, we consider only morning insolation by taking the average downward surface shortwave for 06:00-12:00 LT. The results in Fig. 4.6c,f are somewhat unexpected. The distribution of morning insolation for DCA85 days in both subregions

**Histograms of Environmental Variables  
on 85th Percentile Diurnal Amplitude Days**

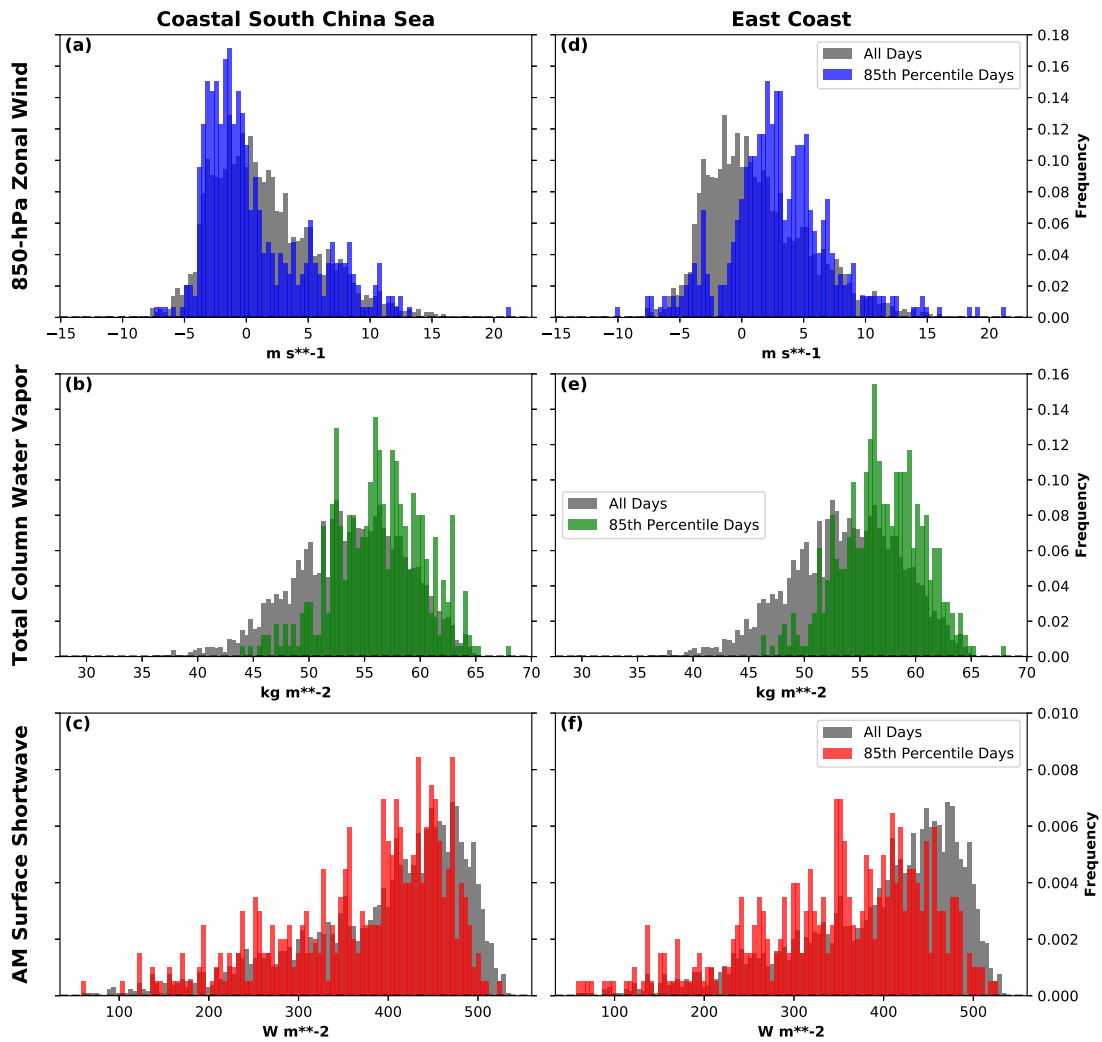


**Figure 4.6:** In gray, histograms of the daily spatial average value inside Boxes A-F (Fig. 4.1) of ERA5 06:00-12:00 Local Time surface shortwave radiation ( $W/m^2$ ; top row), total column water vapor ( $kg/m^2$ ; middle row), and 850-hPa Zonal Wind ( $m/s$ ; bottom row), for . The histogram in color is the histogram of the same variables, but only for days in which the diurnal cycle amplitude exceeded its 85th percentile over the coastal South China Sea (Box B in Fig. 4.1; left column), and the east coast of Luzon (Box E in Fig. 4.1; right column). Binned ERA5 variables still come from Boxes A-F together, but the diurnal cycle inside each sub-box determines the days from which to derive the distribution.

is noticeably *lower* than the distribution for all JJAS days. In other words, a DCA85 day becomes less likely given higher insolation in the morning, but confounding variables are almost certainly present. We hypothesize that low moisture days, which clearly favor a suppressed diurnal cycle (Fig. 4.4b,e), are also associated with reduced cloudiness and thus higher insolation. In fact, the time series of daily TCWV and morning insolation used here are negatively correlated with  $R^2 = 0.49$ . This is substantially higher than the correlation of u850 with TCWV or morning insolation, which yield  $R^2$  values of 0.14 and 0.26 respectively. The lack of moisture on such unusually sunny days appears to be a more significant factor for suppressing the diurnal cycle. This analysis suggests that the influence of insolation on the diurnal cycle is subdued compared to the effect of background moisture and low-level zonal wind.

To tie the above discussion together, 2D histograms of TCWV and u850 are considered to show that the certain background states of wind and moisture lead to strong diurnal cycles. Subsequently, it will be shown that certain BSISO phases make such conditions more likely. Figure 4.7 shows the 2D histogram based on the daily average values of these two variables in contours. The anomaly in the histogram given the occurrence of a DCA85 day is shown as colors. Anomalies are determined by first calculating the 2D histogram of wind and moisture only on DCA85 days, and then scaling those values as if the sample size were the same for DCA85 days and all JJAS days (e.g. the DCA85 histogram is divided by 0.15). Finally, the difference is calculated and displayed. Bins in which the difference was greater than or equal to a factor of 2 of the JJAS histogram (e.g. 100% greater or 50% less) have a small white dot in their center. On the West Coast of Luzon (a), DCA85 days are considerably more likely when TCWV is near to above average, and u850 is weakly easterly. DCA85 days in Central Luzon (b) are favored again with near to above average TCWV, and near zero to weakly westerly u850. The placement of higher probabilities includes noticeably more westerly winds than the West Coast. The East Coast (c) shifts the distribution further towards westerly wind and higher moisture, occupying mostly the upper right quadrant. A similar story can be derived from the offshore boxes. In each subregion, DCA85 days occur preferentially with near to above average moisture and near zero to easterly winds, but perhaps

show slightly stronger sensitivity to moisture than wind given the positive anomalies occurring in the upper right quadrant, even though the most substantial anomalies are in the upper left. Conversely, the strongest anomalies for the West Coast are generally close to average TCWV, but solidly in easterly u850. 2D histograms with insolation against both u850 and TCWV were also considered, but partially due to the higher correlations between those variables, they do not aid interpretation and were excluded.

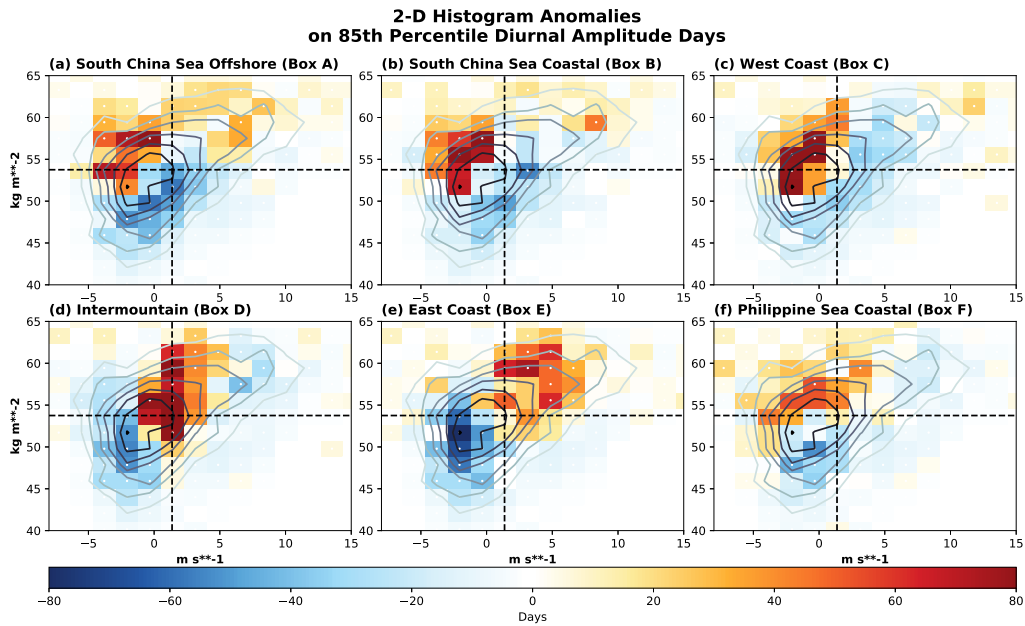


**Figure 4.7:** In contours, the 2-D histogram by bins of ERA5 850-hPa Zonal Wind averaged in Boxes A-F together (Fig. 4.1 on the x-axis (m/s), and ERA5 total column water vapor ( $\text{kg/m}^2$ ) averaged in Boxes A-F on the y-axis, and is the same in each panel. There are 20 total bins in both the zonal wind and total column water vapor distributed evenly between their respective maximum and minimum values. Contours are located every 12 days, with the innermost contour indicating 84 days. 2806 total days are used from JJAS 1998-2020 in this analysis. Colors indicate the anomalies in the histogram (of values for Boxes A-F together) given that an 85th percentile diurnal cycle amplitude day occurred in one of the 6 boxes A-F, and varies by panel. Values are scaled before calculating anomalies such that they represent the expected number of days in each 2-D bin if 2806 85th percentile days were to occur (i.e. the histogram is divided by 0.15, and then the anomaly is calculated). The top row's histograms comes from average precipitation rate Boxes C-E, which include mainly land points, while the bottom row comes from Boxes A, B, and F, which include mainly oceanic points. The vertical dotted black line indicates the JJAS mean 850-hPa Zonal Wind, while the horizontal dotted line indicates the JJAS mean total column water vapor.

Figure 4.8 shows a similar style of 2D histograms, but with anomalies showing the difference in distribution given a certain BSISO phase in order to demonstrate that the wind and humidity conditions favorable for a DCA85 day in Fig. 4.7 are well mapped by some BSISO phases. In BSISO Phase 1, the distribution appears heavily centered on the lower right quadrant, indicating westerly winds and below average moisture. In Fig. 4.7, it is evident that TCWV/u850 values in this quadrant make a DCA85 day much less likely for all subregions, which supports the results described above in Figs. 4.3 and 4.5 which indicated suppressed diurnal cycles in BSISO phase 1. In BSISO Phases 2 and 3, the probability distribution shifts more towards easterly wind, but remains dry. This situation can favor a strong diurnal cycle on the West Coast (Fig. 4.7a), but not the other subregions. The composite analysis in Fig. 4.3 shows that these phases are indeed associated with a substantial diurnal cycle centered on the west coast, but it struggles to propagate offshore. In phase 4, the distribution shifts more towards higher moisture values, but remains easterly. This situation is more favorable for offshore propagation on the west side of the island, which is seen in Fig. 4.3d. In phases 5-6 (Fig. 4.8e-f), the upper left quadrant is most favored, which is associated with enhanced odds of a DCA85 day particularly in the SCS. Phases 7-8 tend to have above average moisture, but strongly westerly winds, which is unfavorable for the diurnal cycle on the West Coast and in the SCS. However, this quadrant is where the most DCA85 days on the East Coast are observed (Fig. 4.7).

To emphasize the variability within a specific BSISO phase, the same Hovmöllers from Fig. 4.3 are displayed in Figs. 4.9 and 4.10, but separated by the zonal wind profile. Days that have an active BSISO in one of the eight phases, but also have an anomalously easterly wind as indicated by the first EOF of the vertical profile of Luzon zonal wind (described in Chapter 3) less than or equal to  $-0.25\sigma$  are shown in Fig. 4.9. Those with a westerly wind are shown in Fig. 4.10. The disparities between the two are striking. Regardless of BSISO phase, restricting the composite to easterly wind leads to the emergence of the clear canonical offshore propagating diurnal cycle. When restricted to westerly wind, this signal disappears entirely, from even the phases exhibiting the most prominent tendencies for offshore propagation (phases 4 through 6). The composites in

### 2-D Histogram Anomalies on BSISO Active Days

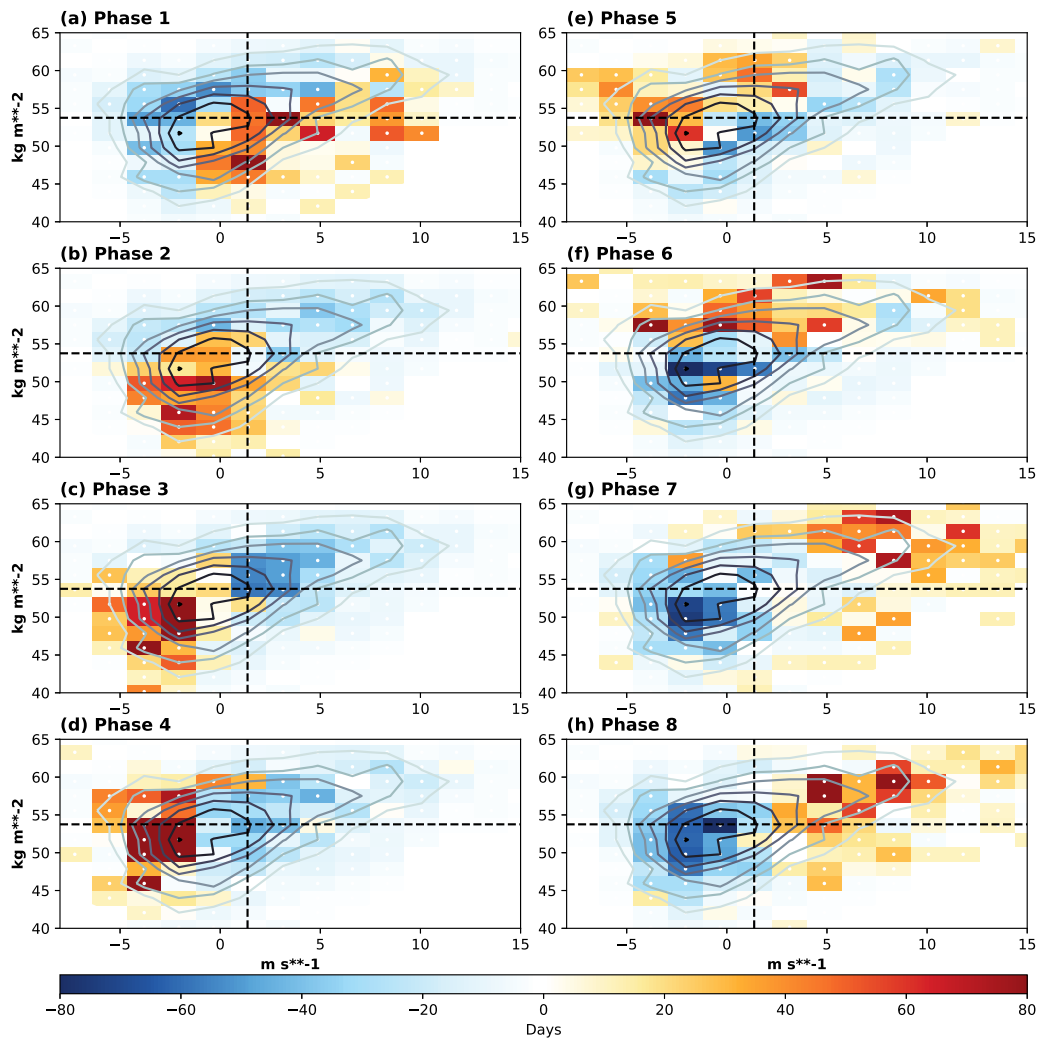


**Figure 4.8:** As in Fig. 4.7 for the contours and vertical lines. Colors indicate the anomalies in the histogram given that the BSISO was active in a certain phase. Values are scaled before calculated anomalies such that they represent the expected number of days in each 2-D bin if 2806 days from each BSISO phase were to occur. For example, to display the Phase 1 anomaly, the 2-D histogram is multiplied by 2806/188 (188 is the number of BSISO Phase 1 active days shown in Fig. 4.2c in JJAS 1998-2020), and then the anomaly is calculated.

4.3 can then be interpreted as which wind regime is more likely under a certain BSISO phase. For example, easterly winds are much more likely in Phases 2 through 5 (as indicated by the number in parentheses in the title of each panel, which shows the total number of days in each composite). Westerly days make up the bulk of the BSISO composite days in Phases 7, 8, and 1, while Phase 6 is fairly evenly split between the two. Considering the variability within a given phase clearly demonstrates that the BSISO phase simply makes certain environmental conditions more likely, which then impact the local diurnal cycle.

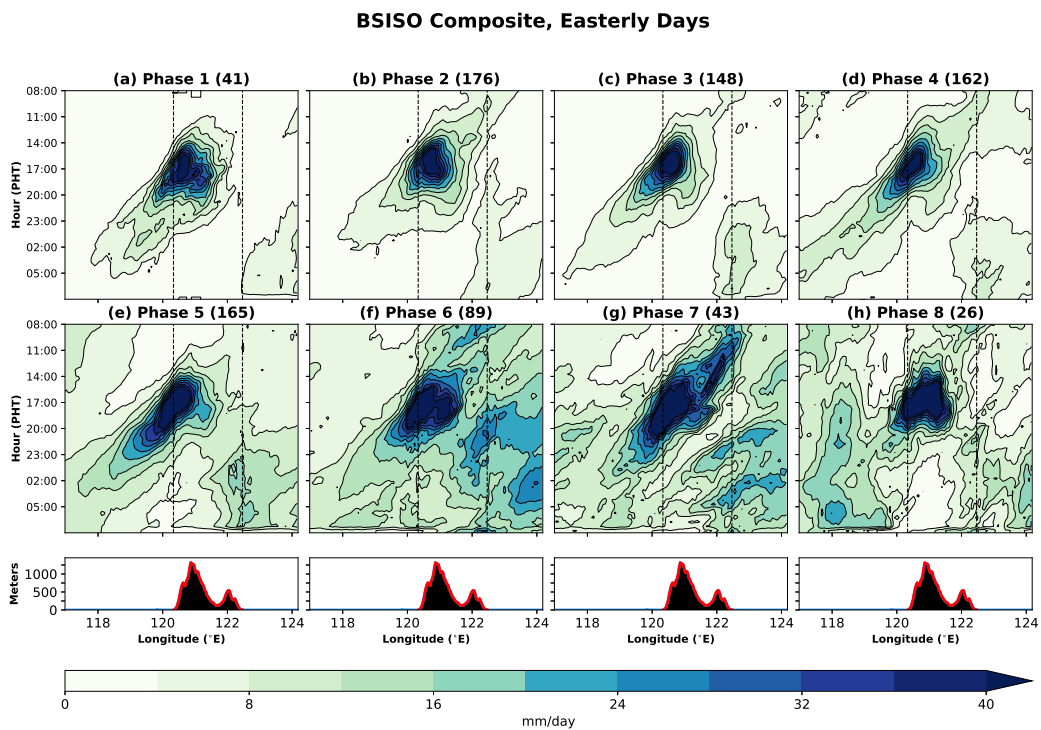


**Figure 4.9:** As in Fig. 4.3, but with the composite restricted to BSISO active days in a certain phase on which the first EOF of the Luzon vertical profile of zonal wind described in Chapter 3 was less than or equal to  $-0.25\sigma$ , indicating anomalous easterly winds. The number in parentheses next to the title indicates the number of days in each composite.

In summary, strong diurnal cycles tend to occur with ambient conditions characterized by near to above average moisture, and weak offshore winds. Since certain BSISO phases make such conditions more probable, the impact of the BSISO on the local diurnal cycle can be understood

### BSISO Composite, Westerly Days

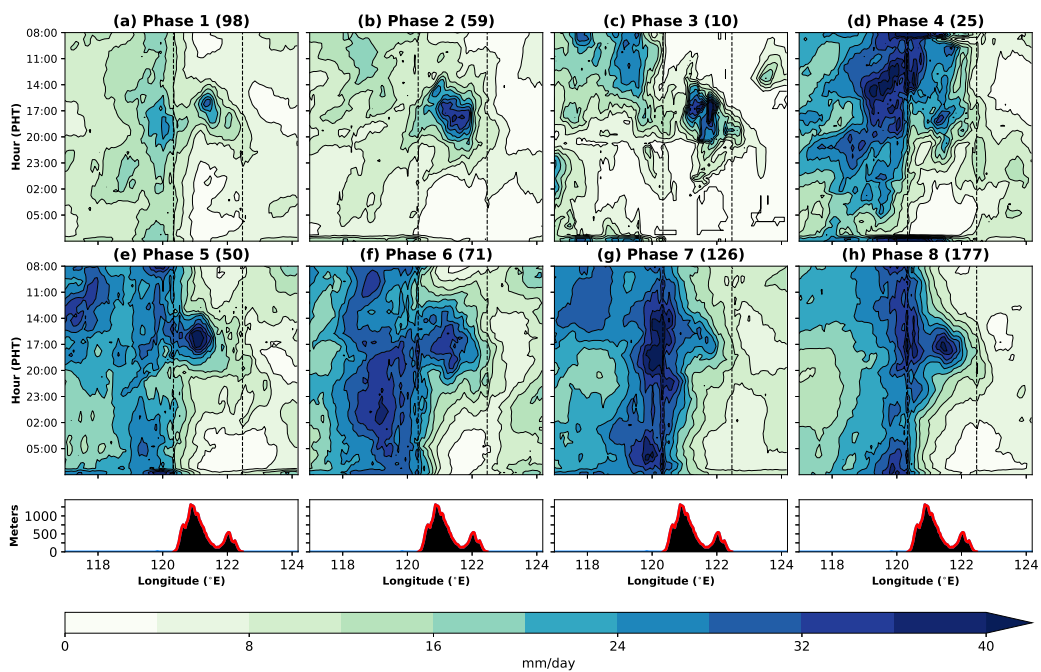


**Figure 4.10:** As in Fig. 4.3, but with the composite restricted to BSISO active days in a certain phase on which the first EOF of the Luzon vertical profile of zonal wind described in Chapter 3 was greater than or equal to  $+0.25\sigma$ , indicating anomalous westerly winds. The number in parentheses next to the title indicates the number of days in each composite.

in terms of its modulation of the local environment, particularly the ambient moisture and low-level wind. The analysis in this section takes a probabilistic approach toward understanding this relationship, and considers the variability within each BSISO phase rather than simply analyzing a composite which may smooth out much of this variability. The results here support those derived from composite analysis (e.g. Chapters 2 and 3), but are not subject to the same limitations, thus reinforcing the conclusions. Not all BSISO active days in a certain phase are the same, and this analysis shows how the relative probability of a strong diurnal cycle changes given the range of environmental background conditions possible within each phase. The results generally support those found with composite analysis (e.g. Xu and Rutledge 2018; Natoli and Maloney 2019; Chudler et al. 2020; Sakaeda et al. 2020), but broaden the understanding of the variability within the composite, and present a clearer case for the mechanisms involved.

## 4.4 CM1 Experiments

In this section, idealized model experiments will be discussed in order to control for the mechanisms cited as important for the BSISO-diurnal cycle relationship highlighted in the previous section. The observational analysis provides the best information regarding what is happening in the real atmosphere, but potentially major confounding factors are present. For example, it is challenging to separate the impact of one mechanism from another, which warrants the use of a model to control this more tightly. In the first subsection, we will show that several important aspects of the variability of the local diurnal cycle as a function of BSISO phase can be replicated in the simplified set up here, which validates the use of this setup for sensitivity experiments. The next subsection will explore variations applied to the base-state that test sensitivity to specific aspects of the environmental background conditions such as wind, moisture, and insolation. Lastly, we will consider the extent to which these results can be generalized by altering the size of the island in the experiment, and identify aspects of precipitation behavior specifically attributable to the diurnal cycle of insolation by fixing insolation at its daily mean value. Throughout the section, only meridionally averaged results are discussed.

#### 4.4.1 Control Experiments

Hovmöller diagrams of the full 7-days of the control simulations with BSISO phases 3 and 7 base-states are shown in Figure 4.11. Convection develops over land every afternoon, and exhibits some offshore propagation on most days. There is some variability in the strength of precipitation and the extent of offshore propagation, but no clear trends in behavior after the first day. Thus, for much of the next few subsections, a daily composite across the 7 days will be used to ease the interpretation and smooth random variability.

Figure 4.12 shows the results of this composite for control simulations from all eight BSISO phases. Comparing these results to Fig. 4.3 reveals several important insights. Starting with the similarities, it is evident that precipitation in the model is diurnally driven, with a peak over land around 17:00 that then slowly propagates offshore at around 3-6 m/s. Phase 3 and 4 base-states lead to precipitation clustered closer to the western coast as in observations. In most simulations, a very weak precipitation signal initiates in the early afternoon on both coasts, and propagates inland until the two sea-breeze fronts converge, leading to deep convection and heavier precipitation rates (Saito et al., 2001). The general preference for a strong diurnal cycle over land in the suppressed and transition to active BSISO base-state is also well replicated. Furthermore, the most obvious offshore propagation occurs with Phase 3-6 base-states, coinciding with the best propagation into the SCS in observations (Fig. 4.3e,f). We note that precipitation propagates exclusively eastward with the phase 6 base-state rather than both directions but mainly westward in observations (Figs. 4.3, 4.9, and 4.10), but the intensity of offshore precipitation is elevated compared to phases 7, 8, 1, and 2. With the Phase 7-8 base-states, the diurnal cycle is weaker and shifted to the east side of the island.

There are also several important differences between the model depiction and the real atmosphere. The model completely lacks any non-diurnally driven precipitation. While observations show significant precipitation at all times of day especially over the coastal SCS during the BSISO active state, the model is unable to reproduce this. The only oceanic precipitation produced is that which is clearly associated with offshore propagation of convection that initiated over land in the

## Full Control Simulation Precipitation Rate

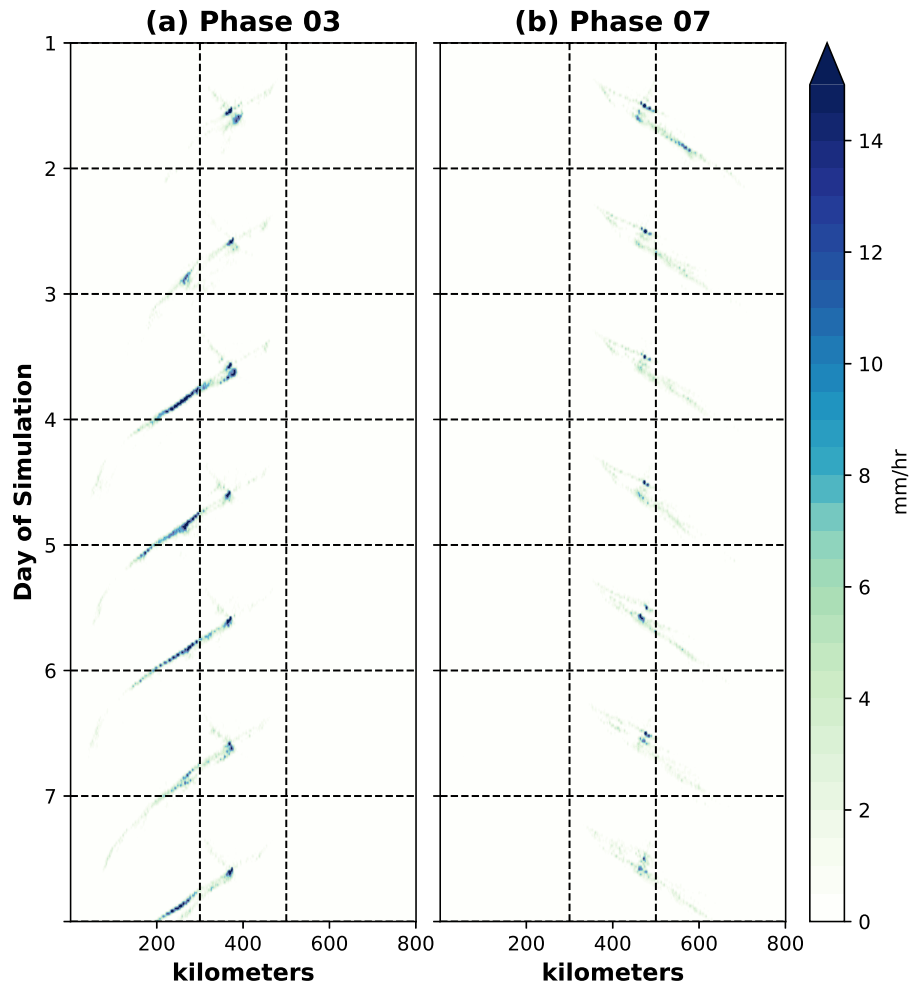


**Figure 4.11:** Meridionally averaged precipitation rate (mm/hr) for the full 7-day simulation the Cloud Model 1 (CM1) control simulations with a BSISO Phase 3 base-state (a), and a BSISO Phase 7 base-state (b). The x-axis in each is in km, with the coastlines marked as vertical dotted black lines. 05:00 on each day is noted as a horizontal dotted black line.

### Control Composite Precipitation Rate

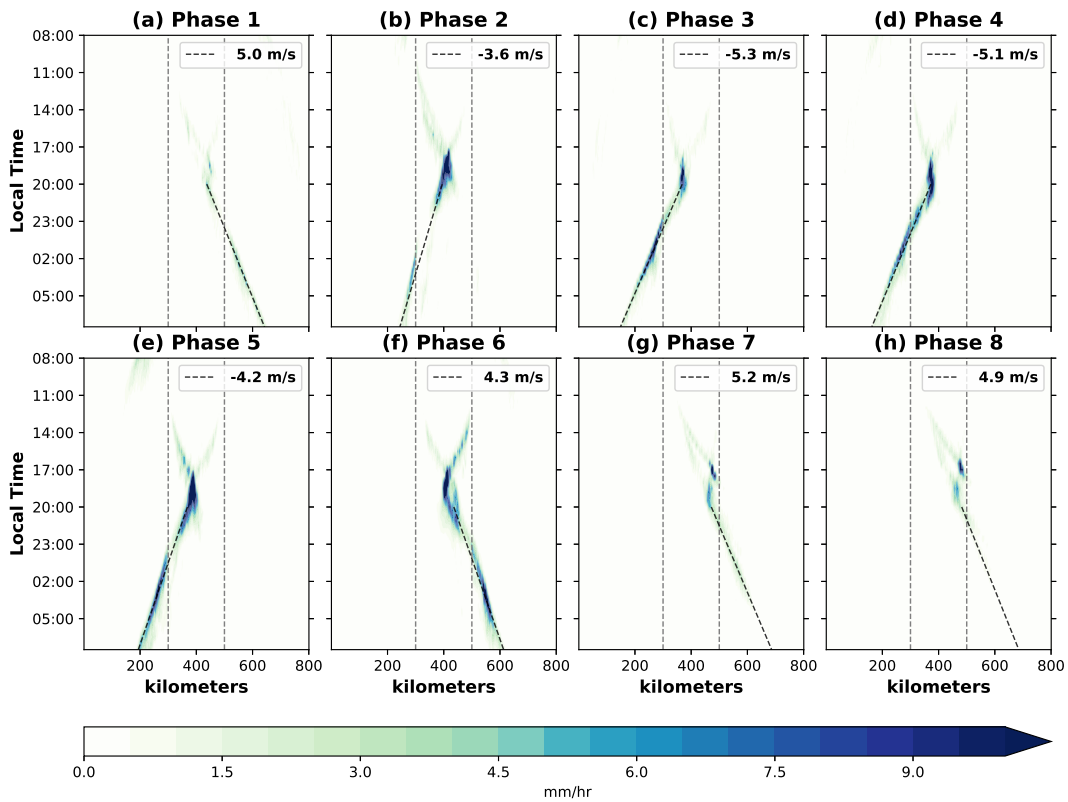


**Figure 4.12:** Daily composite of the 7-day control CM1 simulations showing meridionally averaged precipitation rate (mm/hr) by longitude at 1-km resolution. Each simulation varies the base state with ERA5 BSISO composite profiles. The wind and moisture profiles are shown in Fig. 4.2a-b. Dotted gray lines note the coastlines, and the dotted black line follows a line of best fit connecting the longitude of maximum precipitation rate at each time between 20:00 and 08:00. This is calculated based on precipitation rate smoothed to 5-km resolution.

afternoon. This is not necessarily a weakness though, as it allows the claim to be made that most precipitation is due to the diurnal cycle in this simulation, and thus removes one confounding variable in the real atmosphere of determining how much precipitation is related to the diurnal cycle. Propagation also only occurs in one direction, and is fairly symmetric between eastward and westward propagation. In the observations, westward propagation is clearly dominant over eastward, but there is some evidence of propagation occurring in both directions in a single phase (Figs. 4.3, 4.9, and 4.10). Some of this variability is consistent with the discussion in the previous section, in which the variability of conditions within a BSISO phase was discussed. In the real composites, a range of different days with varying conditions were present, while the composite base-state used in the model only provides one of many possible realizations.

Based on the aspects that the model captures well, the successive sensitivity experiments aim to test the sensitivity of the tropical diurnal cycle behavior to the environmental background conditions. We aim to determine which aspects of the ambient atmosphere determine why a strong diurnal cycle occurs over land during Phases 2-5, why the opposite is apparent in Phases 7, 8, and 1, how much precipitation will be produced by offshore-propagating convection, and which direction convection will propagate.

## **4.4.2 Sensitivity Experiments**

### **Wind**

Next, the BSISO Wind Only experiments will be discussed. In this set, we only vary the base-state zonal wind profile across simulations, while all other variables have a base-state fixed at the JJAS mean. The similarities between these results and those from the control simulations will show what aspects are likely determined by the wind profile, while the differences show what other variables, particularly moisture, modulate. Figure 4.13 shows the composite diurnal cycles for the Wind Only experiments. At first glance, these results look very similar to the control. By only changing the base-state wind profile, several qualitative aspects of the diurnal cycle behavior are retained. Notably, the strong land-based diurnal cycles in Phases 2-5, the weak diurnal cycle

on the eastern coast in Phases 7, 8, and 1, and the significant offshore propagation in Phases 3-6. This supports the argument that the BSISO modulation of the wind profiles is one of the primary mechanisms through which it impacts the diurnal cycle (e.g. Chapter 3, Short et al. 2019; Peatman et al. 2021). Critically, the strong onshore wind appears to be the primary variable responsible for the reduction in diurnal cycle strength during the BSISO active state (Phases 6-8). The model produces a stronger diurnal cycle on the leeward side of the island under a weak to moderate background wind, similar to previous modeling studies and observations (Ho et al., 2008; Virts et al., 2013; Liang et al., 2017; Wang and Sobel, 2017; Qian, 2020). Conversely, a strong wind, particularly in the lower atmosphere, reduces the magnitude of diurnally generated precipitation by limiting the land-sea contrast, and thus the sea-breeze circulation (Shige et al., 2017; Wu et al., 2017; Yokoi et al., 2019).

Since the differences compared to the control runs are difficult to discern in Fig. 4.13, Figure 4.14 shows the average precipitation rate over land, and over ocean on the leeward side of the island for both the Control and Wind Only simulations. Notably, more than simply wind variability appears to regulate precipitation variability in the control simulations. Over both land and water, Phases 1-4 produce more precipitation when only the BSISO wind is used, while Phases 5-8 produce less. Not coincidentally, Phases 1-4 have drier than average moisture profiles in BSISO composites, while Phases 5-8 are more moist (Fig. 4.2b). The reduced ambient moisture during the suppressed BSISO phases inhibits what would be a stronger diurnal cycle based on weak to moderate easterlies alone, hence reflected in an increase in precipitation during Phases 1-4 when only the wind is varied. The leeward waters actually see the most precipitation with BSISO Phases 3-4 winds, but once the rest of the environmental profile is factored in as in the control, the most precipitation occurs with a BSISO Phase 5-6 profile. This result is unsurprising and is consistent with the observational results discussed above and in the literature, highlighting the tight relationship between free-tropospheric moisture and precipitation in the tropics (Bretherton et al., 2004; Hassim et al., 2016; Vincent and Lane, 2017, 2018; Lu et al., 2019; Sakaeda et al., 2020). The relationship between moisture and precipitation in CM1 will be explored in more detail next.

### BSISO Wind Only Composite Precipitation Rate

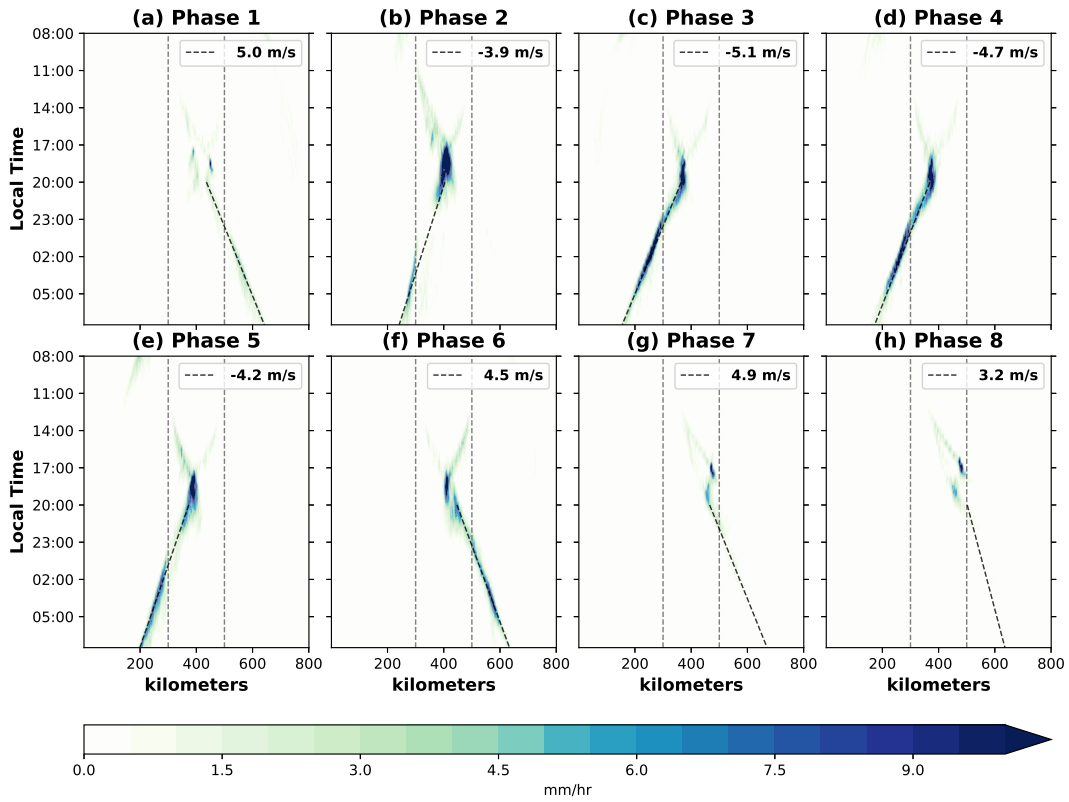


**Figure 4.13:** As in Figure 4.12, but for the wind-only CM1 simulations. The base-state for these simulations uses the wind profile from each BSISO phase composite (shown in Fig. 4.2a), and the JJAS mean profile for the moisture and temperature.

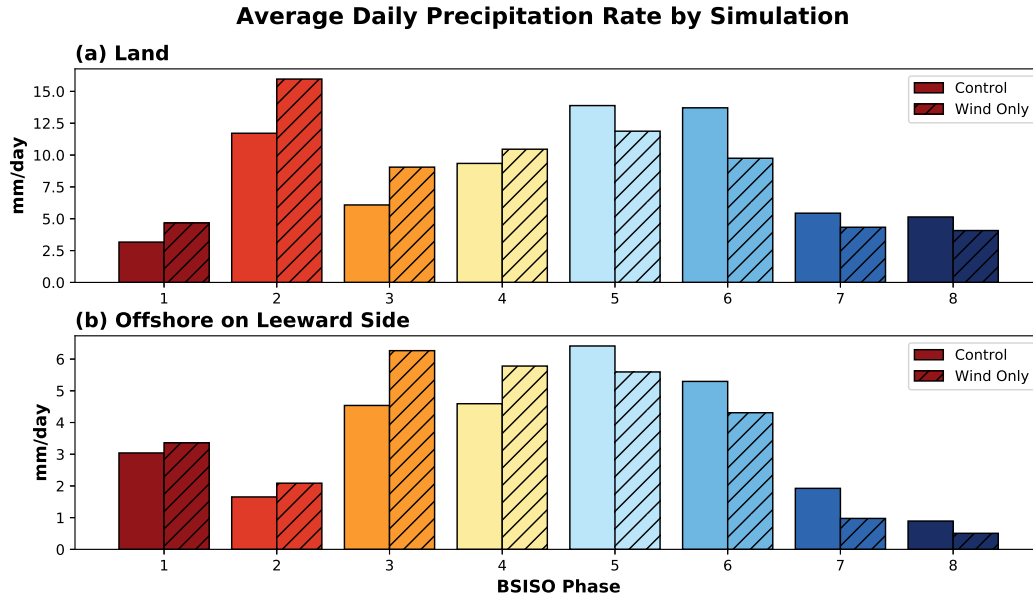


**Figure 4.14:** (a) CM1 precipitation rate (mm/day) averaged over land for each of simulations with varying BSISO composite derived base-states. Bars for the Control simulations (Fig. 4.12) are solid colors, while those for the Wind-Only simulations (Fig. 4.13) are hatched. (b) As in (a), but averaged over the ocean grid points on the leeward side of the island (west for Phases 2-5, east for others).

## Moisture

The next set of experiments takes a closer look at the role of ambient moisture by exploring a wider range of moisture profiles, the details of which are described in Section 2. Average precipitation rate by time of day in the diurnal composite for each simulation is shown in Figure 4.15 averaged over the modeled landmass (300-500-km), and in Figure 4.16 averaged over ocean grid points on the leeward side of the landmass (0-300-km in easterly flow, 500-800-km in westerly flow). The expected result of increasing precipitation with increasing moisture emerges with both BSISO phases 3 and 7 winds. Differences between the wettest and the driest experiment are dramatic, likely resulting from the fairly extreme moisture profiles used here. Interestingly, the diurnal cycle over land does appear to peak earlier in the day under high moisture conditions, consistent with Riley Dellaripa et al. (2020), who showed an earlier diurnal cycle peak during BSISO active conditions when topography was removed from the model. Significantly more rainfall in the higher moisture experiments again emphasizes the importance of having sufficient ambient water vapor

content to attain significant precipitation in the tropics (Holloway and Neelin, 2009, 2010), since convection developing in a dry environment will entrain dry air and weaken (Kuo et al., 2017).

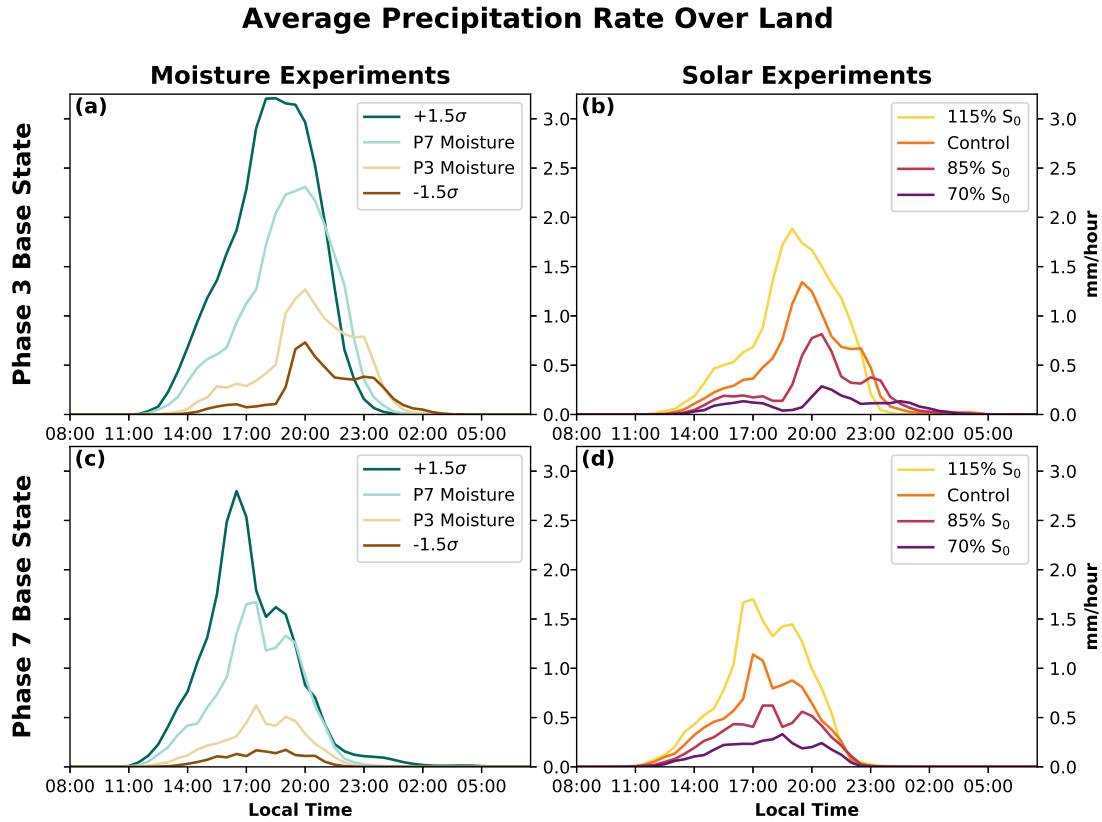


**Figure 4.15:** Composite precipitation rate (mm/hr) averaged over land for the moisture experiments (left), and solar experiments (right). Simulations in the top row use BSISO Phase 3 profile in the base-state, while the bottom row forces BSISO Phase 7 profile in the base-state. The moisture experiments use the BSISO profile only for the winds, the JJAS mean temperature profile, and prescribe the moisture profile. The solar experiments use the control BSISO profile in the base-state, but vary the solar constant.

Examination of precipitation in the offshore environment (Fig. 4.16a,c) by moisture experiment reveals surprising results. With BSISO Phase 3 winds, there appears to be little to no relationship between the ambient moisture and offshore precipitation. The lowest (but broadest) peak in precipitation rate occurs with the  $+1.5\sigma$  moisture, while the highest precipitation rate occurs with Phase 3 moisture, which is the second driest sounding studied. The expected result would be for the offshore precipitation to be even more stratified by moisture than land-based precipitation based

### Average Precipitation Rate Over Ocean (Leeward Side)

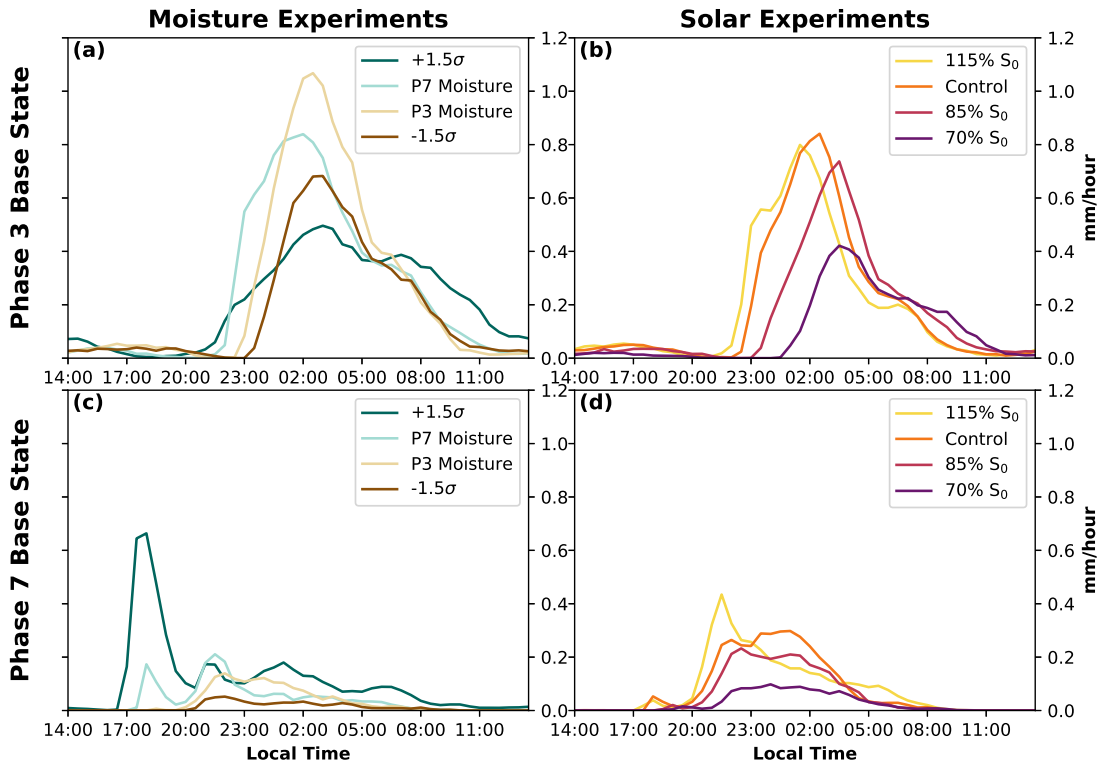


**Figure 4.16:** As in Fig. 4.15, but averaged over ocean on the leeward side of the island (west for Phase 3, east for Phase 7).

on the results from Section 3. We present a few hypotheses to explain this discrepancy, but leave a more conclusive answer to future work. First, the Phase 3 wind profile is easterly throughout the column, and thus moisture advection by the mean wind acts to moisten the environment west of the island. The offshore environment on the leeward side of the island moistens over the first two days of the simulation (not shown), and results in about a 10% increase in TCWV by day 3, while the east side of the island exhibits a 10% decrease. The large-scale nudging techniques employed to maintain the base-state only nudge the domain mean, so a redistribution of moisture across the domain will not be corrected. Thus, the driest simulations are not quite as dry in the offshore environment as they should be had the initial profile stayed uniform. However, this does not explain the relative lack of offshore precipitation in the  $+1.5\sigma$  experiment. This simulation does result in a much stronger cold pool that develops earlier in the day (not shown) due to the early peak over land (Fig. 4.15a). We offer some speculation on the mechanism involved here. Deep convection initiates along the leeward coast's inland propagating sea-breeze front in both of the increased moisture simulations before opposing sea-breeze fronts converge, and continues to propagate inland after the fronts converge (not shown). This is unlike each of the control simulations, in which the onset of deep convection occurs after the sea-breeze fronts converge. As a result, instability may be more depleted on the leeward side of the island due to the earlier convective onset. A time series of convective available potential energy (CAPE; not shown) indeed indicates that the  $+1.5\sigma$  moisture experiment actually has the *lowest* CAPE on the west side of the island compared to all three other moisture experiments with BSISO phase 3 winds. Another possible explanation is that in the dry state, convection develops along a very narrow density current front, the only location in which there is sufficient lift to attain deep convection. The higher moisture environment isn't as confined to the density current boundary, resulting in a broader precipitation peak.

Overall, the results of the wind and moisture experiments support the conclusions derived from Section 3, in that the BSISO modulation of ambient wind and moisture is what affects the local diurnal cycle. We can replicate several aspects of the BSISO-diurnal cycle relationship in an

idealized model with only the base-state from a composite BSISO profile, although the response to variable moisture profiles over the ocean in CM1 is more nuanced than expected.

## **Insolation**

Next, the insolation experiments are analyzed. While adjusting the solar constant is not an entirely realistic representation of the way in which the BSISO alters insolation, they still provide qualitative information on how insolation variations regulate diurnal cycle strength and offshore propagation. Results are displayed in Figs. 4.15b,d and 4.16b,d next to the moisture experiments to allow for direct quantification of the relative magnitudes of the changes. Over land, increasing the solar constant results in more precipitation, but the relationship is not linear. For example, using a solar constant of 70% its actual value results in precipitation peaking much lower than 70% of its value in the control run (Fig. 4.15b,d). Over ocean, however, the control experiment, the 115%, and the 85%  $S_0$  experiments have fairly similar precipitation rates, with just a delay in the timing as  $S_0$  decreases (Fig. 4.16b,d). The 70%  $S_0$  experiment displays a peak offshore precipitation rate about half that of the others, despite the diurnal convection being reduced by much greater amounts than this over land. This appears to indicate that the strength of daytime convection over land is not directly proportional to the strength of nocturnal offshore precipitation in this model.

These results support hypotheses that the lack of insolation during the BSISO active phase due to increased cloudiness could indeed result in a weaker diurnal cycle (Peatman et al., 2014; Birch et al., 2016; Wu et al., 2018; Natoli and Maloney, 2019). However, considering the results of Section 3 (Fig. 4.6), insolation may not be the most important factor leading to the reduction in diurnal cycle strength in the BSISO active phases. The CM1 experiments do not make this case as clearly, which adds some nuance to this conclusion. Precipitation rates appear slightly less sensitive to insolation compared to wind or moisture, but the reaction to insolation variations on par with the change in insolation in a BSISO composite is still substantial. These simulations indicate that solar radiation can have a major impact on diurnal cycle behavior in the absence of other confounding factors, but it is possible that the impacts of the wind profile and ambient moisture overwhelm that of insolation when we consider the observational results in tandem.

### 4.4.3 Impacts of Island Size and Diurnal Variation

The final sets of simulations discussed in this manuscript will explore how sensitive these results are to the size of the island used and analyze precipitation behavior in the absence of a diurnal cycle of insolation in this model. The former set will help establish the extent to which these results can be generalized to other tropical islands. The latter will determine whether radiative cooling at night appears to assist offshore propagation, and if a natural timescale of convection emerges in the absence of diurnal forcing.

7-Day composites of lowest model level zonal wind and precipitation rate in each of the island size experiments are shown in Figure 4.17. While not necessary for the understanding of these results, the full 7-day Hovmöllers of precipitation are shown in Figure 4.18. One striking feature is the presence of two inland propagating sea-breeze fronts across all island sizes. Unsurprisingly, the fronts take longer to converge with a larger island. With a 25-km island and Phase 3 winds, the fronts converge almost immediately, and precipitation develops around 11:00LT, but dissipates before 17:00LT. With a 100-km wide island, this convergence and onset of deep convection occurs around 15:00-16:00LT, and precipitation largely weakens a few hours later. Weak offshore propagation occurs later in the night with a subtle land breeze that develops around 02:00LT. This signal is apparent on four of the seven days, but appears independent from the daytime convection (Fig. 4.18). The 200-km island is identical to the control simulations described above, showing a cohesive transition from land-based convection that develops when the sea-breeze fronts converge around 17:00LT to offshore propagation after 20:00LT. With a 400-km island, the sea-breeze fronts converge later around 20:00LT, and offshore propagation is evident in the composite (Fig. 4.17), occurring on three of the seven days (Fig. 4.18). The largest island experiments result in sea-breeze fronts not converging until well after midnight, and no evidence of clear offshore propagation. It is worth noting that the strength of land-based precipitation as a function of island-size found in these simulations is not consistent with some prior research (e.g. Robinson et al. 2008; Cronin et al. 2015; Wang and Sobel 2017), which pointed to maximum precipitation with an island size of around 40-km rather than the 200-400-km identified here.

Island Size Experiments: Lowest Model Level Zonal Wind Composite

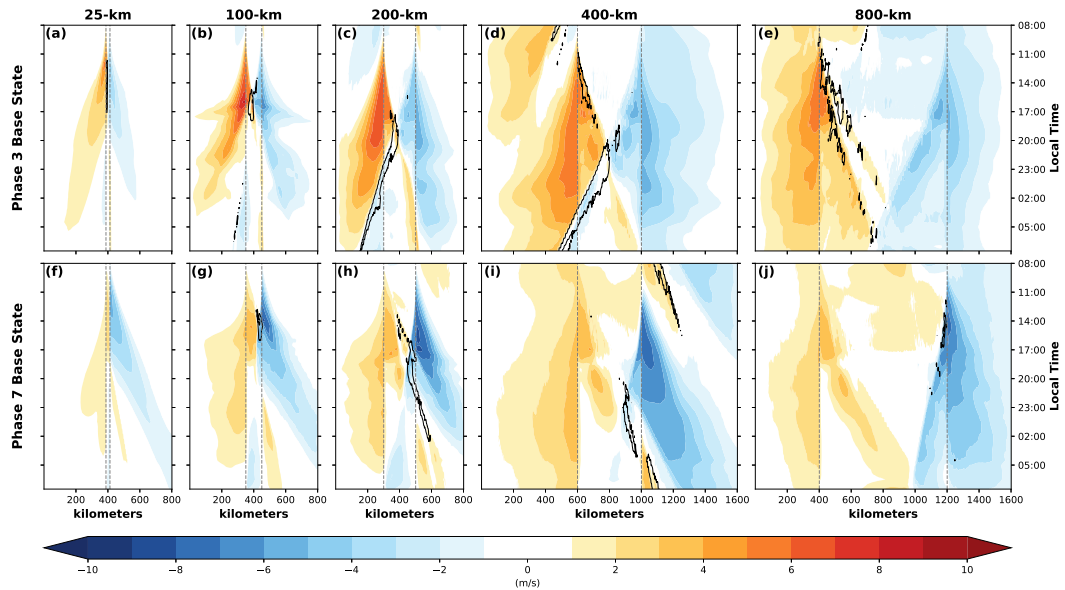


**Figure 4.17:** Daily composite of meridionally averaged lowest model level zonal wind (m/s) in color, with the 2 mm/hr contour of composite precipitation rate superimposed. BSISO Phase 3 base-state is used in each simulation in the top row, while BSISO phase 7 base-state is used in the bottom row. The size of the island positioned in the center of the domain is 25-km (a, f), 100-km (b, g), 200-km (c, h), 400-km (d, i), and 800-km (e, j). The 200-km simulation is identical to the control simulation in Fig. 4.11a. The domain size is 800-km for (a-c, f-g), but increases to 1600-km for (d-e, i-j).

### Island Size Experiments Precipitation Rate

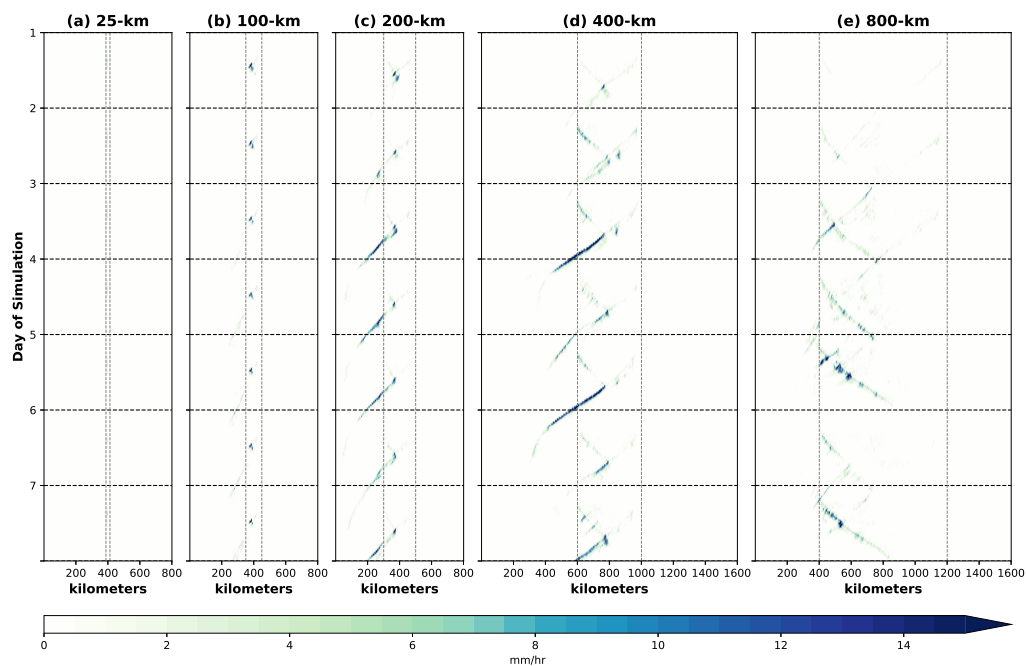


**Figure 4.18:** Meridionally averaged precipitation rate (mm/hr) for the full 7-day Island Size experiments. BSISO Phase 3 base-state is used in each simulation. The size of the island positioned in the center of the domain is 25-km (a), 100-km (b), 200-km (c), 400-km (d), and 800-km (e). The 200-km simulation is identical to the control simulation in Fig. 4.11a. The domain size is 800-km for (a-c), but increases to 1600-km for (d-e).

In order to explain why nocturnal offshore propagation consistently occurs with some island sizes but not others, the zonal wind will be examined more closely. With a 100-km island, the sea-breeze strength is maximized just before 17:00LT, after which time it slowly weakens. A weak land breeze develops, but long after daytime convection had already dissipated. In the 200-km (and the 400-km to a lesser extent), the sea-breeze remains strong later into the evening, and precipitation is ongoing when the land breeze develops. We hypothesize that the combination of cold pool dynamics in existing convection and the development of the land-breeze leads to offshore propagation. At least in CM1, the synchronization of the cold pool and land breeze in time may be important for offshore propagation. Thus, having convection present over land in the hours after sunset when the land surface starts to cool due to radiative process may make offshore propagation more likely.

The last set of simulations in this manuscript removes the diurnal cycle of insolation entirely. This was inspired by the results of the island-size experiments, as well as the possibility that there is a natural timescale in CM1 for offshore propagation that is independent of the diurnal cycle of insolation. Thus, if insolation synchronizes with this, a particularly strong diurnal cycle might be produced. In order to best compare to the control simulations and examine precipitation behavior under a variety of environmental conditions, these experiments are repeated for each of the eight BSISO composite base-state profiles. The results for the first 2 days of the 7-day simulation are shown in Figure 4.19. Without a diurnal cycle, a composite would be meaningless, but only the first two days are shown since the latter five days do not add significant additional information. Since maximum insolation is much weaker (recall that  $S_0$  is  $444.1 \text{ W/m}^2$  and the zenith angle is fixed), it takes longer for precipitation to develop with constant solar flux. In most simulations, deep convection doesn't emerge until close to 18 hours after "sunrise" (05:00LT) at 23:00LT. Additionally, nearly zero precipitation develops with the Phase 7 or 8 base-state, indicating a heightened sensitivity to the prevailing wind with much weaker thermodynamic forcing for convection. The most important aspect of these simulations to emphasize is the complete lack of oceanic precipitation at any time in any simulation. This indicates that cold pool and internal storm dynamics of weak

convection is not sufficient to initiate offshore propagation. Even though these simulations do have converging sea-breeze fronts (not shown), there is no land breeze and thus no offshore propagation. Some indication of a roughly 12-hour timescale of more intense convection can be seen here, which will be explored in more detail next when island-size is varied again.

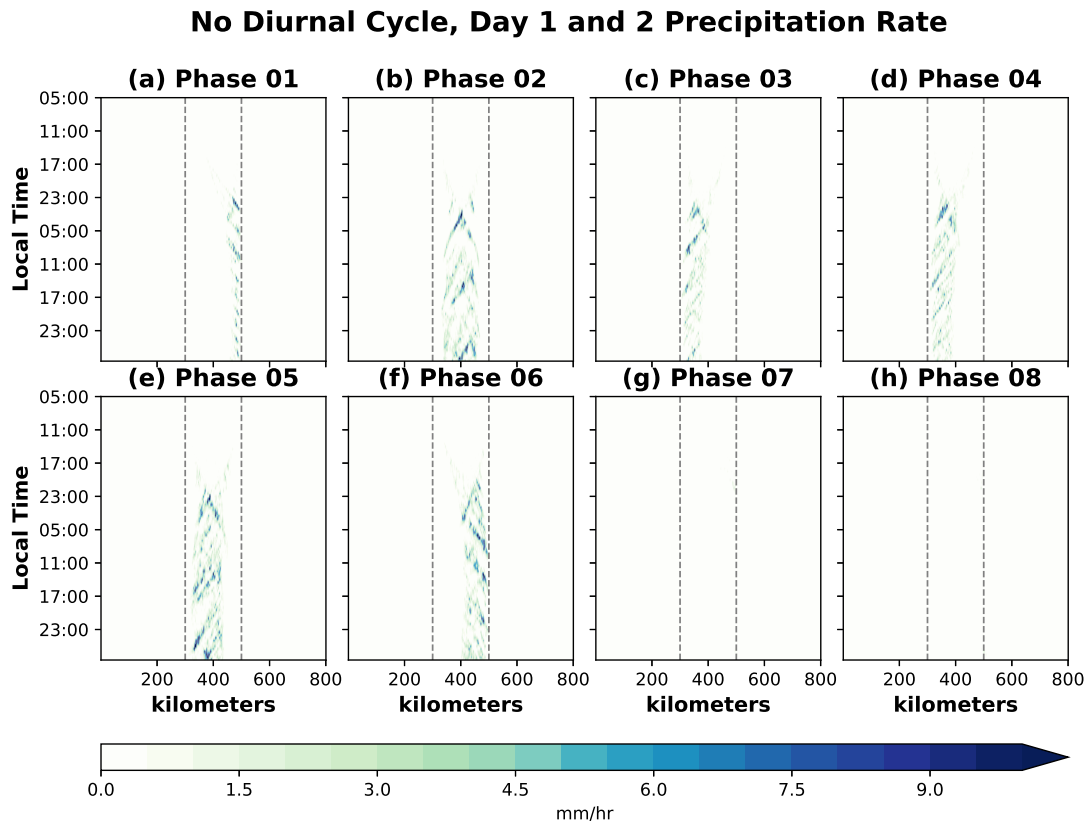


**Figure 4.19:** Meridionally averaged precipitation rate (mm/hr) for the first 2 days of the No-Diurnal-Cycle experiments. Simulations from each of the 8 BSISO base-states are shown. The diurnal cycle is removed by fixing the solar constant at the daily mean top-of-atmosphere incident shortwave on 1 August at 17N and fixing the solar zenith angle at  $0^\circ$ .

The island-size experiments were also repeated with the diurnal cycle removed (though with Phases 2 and 6 base states, since very little precipitation developed without a diurnal cycle and a Phase 3 or 7 base-state). The full 7-days of precipitation for these simulations is shown in Figure 4.20. First, we note that these simulations show slower inland propagation of the sea-breeze fronts, which is consistent with an expected slower density current propagation speed when the temper-

ature difference between the cold pool air and the environment is smaller (Benjamin, 1968). The behavior in the 400-km island simulation is particularly interesting. Somewhat cyclic precipitation develops, and generally propagates westward towards the leeward coastline, but dissipates abruptly upon reaching the shoreline. This adds support to the hypothesis that a land-breeze may be necessary for offshore propagation, and suggests the presence of a preferred time-scale of convective regeneration. Since precipitation is a noisy field, time series of T2m averaged over the island are shown in Figure 4.21. Considering the Phase 2 base-state, remarkable oscillatory behavior is evident in the surface temperature fields, but the relationship to island-size is nonlinear. The 400-km island shows the most pronounced periodicity, with a minimum in temperature occurring slightly longer than every 24-hours. The 200-km simulation experiences a T2m minimum every roughly 12 hours, while the 100-km simulation is slightly faster, but not nearly double the frequency. The simulation is too short to reliably estimate the periodicity in the 800-km simulation.

These results suggest the possibility that a strong diurnal cycle could be generated when the 24-hour period of the diurnal cycle is equal to, or a harmonic of, the potential natural timescale of the island. We offer some speculation regarding this observation. The timescale could be a result of the time it takes the two sea-breeze fronts from opposite sides of the island to converge (Fig. 4.17). This results in the initiation of deep convection, which then cools the land surface via evaporation of rainwater until instability is exhausted. Then, the landmass resumes warming until a sea-breeze front is initiated once again. A larger island leads to a longer timescale of convective regeneration due to the greater distance the sea-breeze fronts must travel. There likely is more to the timescale than just the island-size, since the 100-km and 200-km islands have rather similar timescales with the phase 2 base-state, and varying the base-state results in a different timescale (Fig. 4.21). However, the roughly 12-hour timescale seen with the 200-km island size could be a contributing factor to the enhanced tendency for offshore propagation from an island with this width (Fig. 4.18) since this is a harmonic of the 24-hour diurnal cycle of insolation. Perhaps this analysis leads to more questions than answers in its current state, but this suggests several

### No Diurnal Cycle Island Size Experiments: BSISO Phase 2

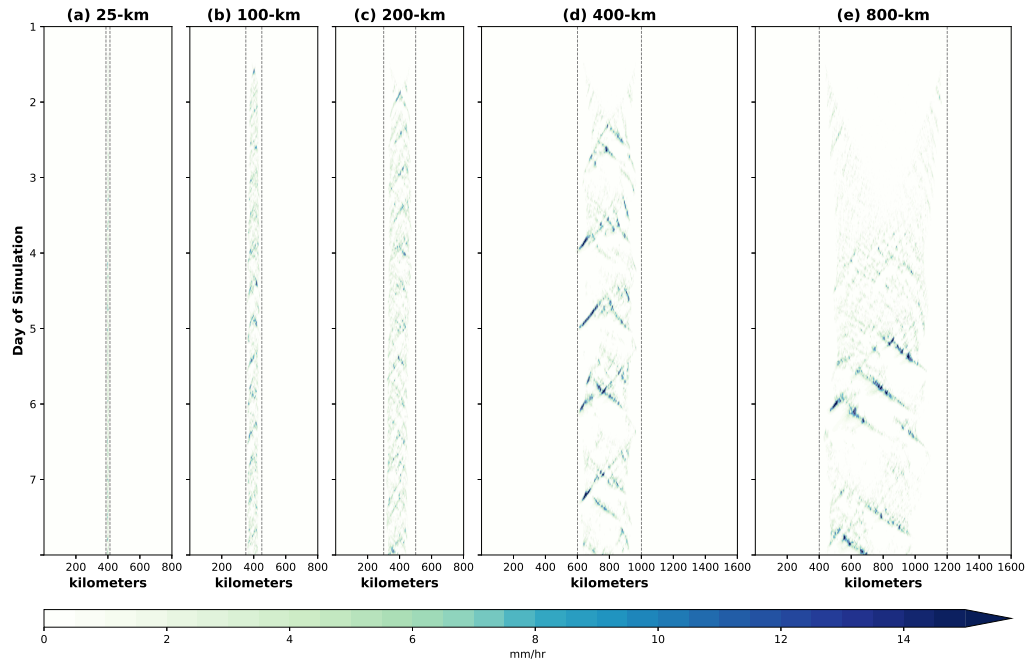


**Figure 4.20:** Meridionally averaged precipitation rate (mm/hr) for the full 7-day Island Size experiments with no insolation diurnal cycle. BSISO Phase 2 base-state is used in each simulation. The size of the island positioned in the center of the domain is 25-km (a), 100-km (b), 200-km (c), 400-km (d), and 800-km (e). The domain size is 800-km for (a-c), but increases to 1600-km for (d-e). The diurnal cycle is removed by fixing the solar constant at the daily mean top-of-atmosphere incident shortwave on 1 August at 17N and fixing the solar zenith angle at  $0^\circ$ .

## Island Size No Diurnal Cycle Experiments Land Temperature

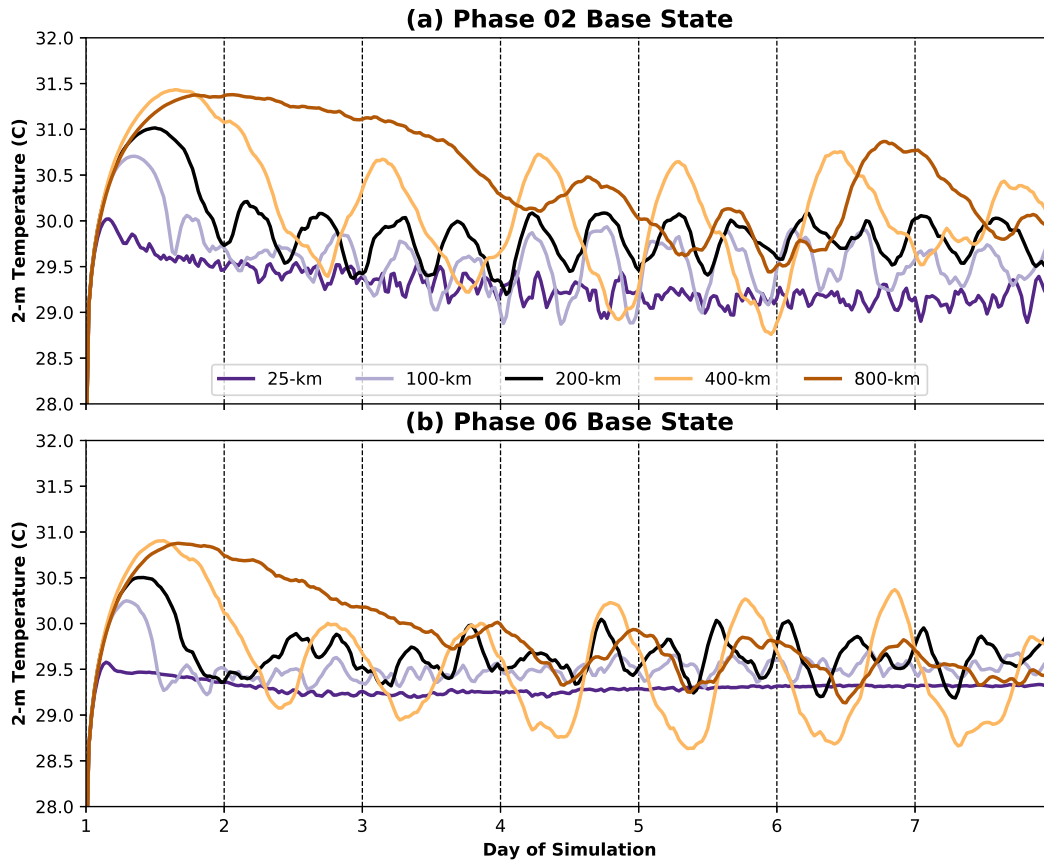


**Figure 4.21:** 2-m Temperature (C) averaged over land points by time for the full 7-day Island Size No Diurnal Cycle Experiments. Phase 2 base-state is used for (a), while Phase 6 base-state is used for (b). Shades of orange have a larger island and domain size compared to the control. Shades of purple have a smaller island but the same domain size.

interesting avenues for future research that examine the potential for a natural oscillating timescale of island-based convection.

In summary, the results of the island-size and no-diurnal cycle experiments propose the hypothesis that a land-breeze, the presence of deep convection over land in the hours after sunset, and significant convergence (such as converging sea-breeze fronts) may be necessary for the development of nocturnal offshore precipitation. The additional radiative cooling associated with the lack of insolation at night combined with cold pool dynamics can spur convection offshore, while cold pool dynamics alone, as in the no-diurnal cycle experiments, may be insufficient for offshore propagation (Figs. 4.19 and 4.20). Additionally, we show that the results in Sections 4a-b may be applicable to islands from roughly 100-km to 400-km in size with the current model setup.

## 4.5 Conclusions

The mechanisms through which large-scale patterns of tropical convective variability such as the MJO/BSISO impact the local diurnal cycle on tropical islands were examined. Using Luzon island in the northern Philippines as an example, a probabilistic approach to observational analysis was employed in lieu of the conventional composite analysis to examine diurnal cycle variability. Such techniques reveal more about the range of possible environments found within a certain phase of the BSISO, and the relative likelihood of a robust diurnally driven precipitation in varying regimes. This contributes a broader understanding of diurnal cycle behavior established through the composite analyses of prior research (e.g. Rauniyar and Walsh 2011; Peatman et al. 2014; Birch et al. 2016; Hassim et al. 2016; Vincent and Lane 2016; Sakaeda et al. 2017). Idealized model simulations with CM1 build upon the observational results, and allow for the isolation of three environmental variables, low-level wind, ambient moisture, and insolation, highlighted by prior research (Birch et al., 2016; Vincent and Lane, 2017; Natoli and Maloney, 2019; Short et al., 2019; Sakaeda et al., 2020) as potentially important for understanding the mechanisms of the BSISO-diurnal cycle relationship. Additional sensitivity tests exploring precipitation behavior in the absence of an insolation diurnal cycle and the role of the island's size in the timescale of

convective variability improve understanding of how CM1 portrays the diurnal cycle. The results address the nature of the diurnal cycle, its offshore propagation, and the physical mechanisms regulating its relationship to large-scale modes of variability (Virts et al., 2013; Wang and Sobel, 2017; Yokoi et al., 2019; Qian, 2020; Peatman et al., 2021). The main findings of this research are summarized as follows:

- The probability of a high amplitude diurnal cycle over the west coast of Luzon is maximized in observations during the suppressed BSISO phases and the transition to active (Figs. 4.3c-e, 4.5c). In the coastal South China Sea (SCS) offshore propagation is maximized in the phases covering the transition from suppressed to active. (Figs. 4.3e-f, 4.5a-b).
- High amplitude observed diurnal cycle days tend to occur with weak to moderate offshore low-level wind and near to above average column moisture (Figs. 4.6a,b,d,e, 4.7). There appears to be little association with morning insolation (Fig. 4.6c,f).
- The transition from BSISO suppressed to active conditions (roughly phases 3-6) is most likely to produce the wind and moisture conditions favorable for a high amplitude diurnal cycle in observations with substantial offshore propagation into the SCS (Figs. 4.7, 4.8).
- Idealized CM1 simulations using a base-state derived from BSISO composite wind, moisture, and thermodynamic profiles (Fig. 4.2) can replicate several important features of the observed diurnal cycle (Fig. 4.3), including the strong land-based diurnal cycle in the BSISO suppressed and transition phases, strong offshore propagation in the transition phases, and the suppressed diurnal cycle during BSISO active conditions (Figs. 4.11, 4.12, 4.14).
- Driving the simulations with only the BSISO wind profile and JJAS mean moisture and temperature profiles results in very similar diurnal cycle behavior to the control simulations, emphasizing the importance of the wind profile in producing the observed diurnal cycle traits by BSISO phase (Figs. 4.13, 4.14). Weak offshore prevailing wind favors an active diurnal cycle with offshore propagation.

- Land-based precipitation exhibits strong sensitivity to ambient moisture in CM1 (Figs. 4.14, 4.15a,c). Moisture anomalies enhance precipitation during the BSISO active phase, and weak precipitation during the suppressed phase, but wind explains the specific preference for the transition period.
- Varying the solar constant in CM1 leads to a robust diurnal cycle response (Figs. 4.15b,d, 4.16b,d). It is likely that insolation would be important in the absence of other factors, but its impact is shadowed by that of wind and moisture in observations (Figs. 4.6c,f, 4.15b,d).
- Experiments in which the diurnal cycle of insolation is removed and the daily mean insolation is applied at all hours equally suggest the possibility for a natural timescale of convective regeneration with some dependence on island width. We speculate that synchronization of the real 24-hour diurnal cycle with this natural timescale could lead to heavier precipitation and more robust offshore propagation (Figs. 4.20, 4.21).
- In CM1, offshore propagation seems to require the presence of a land-breeze, lingering deep convection over land after sunset, and a source of strong convergence, such as converging sea-breeze fronts (Figs. 4.17, 4.19).

The probabilistic view on diurnal cycle behavior combined with the ability of CM1 to realistically simulate many well-studied (e.g. Peatman et al. 2014; Sakaeda et al. 2017; Xu and Rutledge 2018; Lu et al. 2019; Natoli and Maloney 2019; Chudler et al. 2020) aspects of the ISO-diurnal cycle relationship with only the BSISO composite profile used in the base-state strongly suggests that the physical mechanisms regulating this relationship can be reduced to the large-scale modulation of local environmental variables, particularly moisture and wind.

# Chapter 5

## Conclusions

This dissertation has examined the variability of the tropical island diurnal cycle through several perspectives. In Chapter 2, it was shown using observations that the QBWO and the BSISO impact the diurnal cycle over the Philippines in very similar ways, despite operating on different timescales and with different mechanisms. However, each mode impacts the local environment through extending the moisture-laden monsoonal southwesterly winds across the Philippine archipelago. Based on composite analyses of these two large-scale modes, it was hypothesized that the local diurnal cycle behavior can be understood in terms of the background wind, moisture, and insolation on a given day. In Chapter 3, we approached this problem from another angle by examining the impact of the monsoonal flow directly in observations and an idealized model. Temporarily leaving timescale and a specific large-scale mode behind, it was shown that consideration of the background wind profile alone can determine several important aspects of diurnal cycle behavior attributed to a large-scale mode. Lastly, the stated hypothesis was tested in Chapter 4 through a different statistical perspective on the observational data and sensitivity tests with an idealized model. It was shown that notable features of diurnal cycle behavior through a BSISO event identified by Natoli and Maloney (2019) can be replicated in an idealized model when the only BSISO information introduced into the model is the composite wind, moisture, and temperature profiles serving as the model base-state. Observational results showed that a strong diurnal cycle that propagates offshore tends to occur with near to above average moisture and weak offshore wind. Since these conditions are made dramatically more likely during the transition from a BSISO suppressed state to active, these phases often lead to an enhanced diurnal cycle, consistent with prior literature (Peatman et al., 2014; Vincent and Lane, 2017; Sakaeda et al., 2017; Natoli and Maloney, 2019). Conversely, strong onshore winds or a dry free-troposphere lead to a substantial reduction in diurnal cycle strength, which explain why composite analysis did not identify as substantial diurnal cycle activity during the later stages of the BSISO active state or the early

stages of the BSISO suppressed period. This is the main thread connecting each chapter of this dissertation together, although there are also several intriguing conclusions relating to the nature of the tropical island diurnal cycle that are outlined within each chapter.

A few examples of important findings that are not directly related to the overall goal of this dissertation are briefly summarized. Chapter 2 identified the importance of convective variability on quasi-biweekly timescales to the Philippines diurnal cycle. In chapter 3, we showed that a strong background wind acts to ventilate the land-surface and reduce the sea-breeze circulation and diurnal cycle strength. Additionally convection in CM1 appears to propagate offshore in the direction of the background wind in the lower free troposphere at a typical density current speeds, into an environment partially destabilized by gravity waves. Lastly, chapter 4 included a robust probabilistic framework for an alternative to composite analysis in diurnal cycle studies. The simulations that altered the island size and removed the insolation diurnal cycle suggested that the nocturnal radiative cooling, a strong convective cold-pool lingering after sunset, and strong mechanical convergence are all necessary for offshore propagation. Additionally, there may be a natural timescale for convective regeneration that depends on the island width.

There are a few caveats to our analysis here that must be identified. These will lead to suggested avenues for future work to strengthen the conclusions of this research. On the observational side, only the Philippine archipelago has been examined in this dissertation. While prior literature (e.g. Peatman et al. 2014; Vincent and Lane 2016) has suggested that the conclusions regarding the general timing of an active diurnal cycle through an MJO life-cycle hold true for several other regions in the MC, a thorough analysis of the mechanisms involved has not confirmed that our conclusions from Chapters 3 and 4 hold universally. Peatman et al. (2021) found that there can be some differences in diurnal cycle behavior associated with ambient wind between different islands, suggesting that the unique geography of an island may need to be considered when generalizing these results. To address this, the methods of observational analysis applied in this dissertation, particularly the probabilistic techniques described in Chapter 4, could be repeated for other land-masses. Sumatra, Borneo, and New Guinea have been widely studied but these techniques have

yet to be applied there. Additionally, diurnal cycle studies have often overlooked the Southeast Asia mainland coastline. Determining if the conclusions derived here for a tropical island can apply to the coast of a larger continent would also prove enlightening. The coast of southeast Asia, India, the bight of Panama, and the coast of Columbia are compelling regions for further study on that subject. We have also only considered these results with one BSISO index, which may have some difficulties capturing certain events (Wang et al., 2018). Repeating some of this analysis with another of the various MJO/BSISO indices (e.g. Wheeler and Hendon 2004; Kikuchi et al. 2012; Kiladis et al. 2014) could further support these conclusions.

While the simplifications made to the model simulations in Chapters 3 and 4 have significant advantages outlined within the text, they also present some drawbacks. Most notably, only one model has been employed in these studies. There is a possibility that some of the conclusions made in this dissertation are unique to CM1 and may not generalize to other more complex models such as WRF or RAMS. The findings in Chapter 4 regarding the sensitivity of precipitation to the size of the island are not consistent with WRF simulations by Wang and Sobel (2017), who showed maximum precipitation intensity occurring with an island around 40-km in width. Some of this discrepancy could be due to unique characteristics of CM1, so future simulations that repeat this analysis with a different model could improve understanding of both model nature and our physical conclusions. Our simulations also do not include topography. As outline above, the results of Riley Dellaripa et al. (2020) support this decision, but there are undoubtedly some details that cannot be resolved with this simplification. For example, the CM1 simulations in Chapter 3 are symmetric between westward and eastward propagation (Fig. 3.7, while westward propagation is clearly dominant over eastward propagation in observations (Fig. 3.5). Since this cannot be replicated in these simulations, we are unable to test the mechanism producing this asymmetry. However, it is hypothesized that this is related to the asymmetry in the topography of Luzon, with the highest mountains concentrated near the west coast, and a much shorter mountain range on the east coast. The enhanced convergence contributed by the mountains concentrates precipitation near the west coast in the real atmosphere, and it is possible that the east coast range interferes

with cold-pool and land-breeze dynamics, thus limiting eastward propagation. Future simulations directly testing the sensitivity of these results to both idealized and real topography would help generalize these conclusions. We also acknowledge that some aspects of the experimental set-up are not ideal. The large-scale nudging technique which is necessary to maintain the base-state through a longer simulation still allows significant spatial variability to develop in the temporal mean. This is not necessarily physical and could impact the interpretation of some results, specifically in the moisture sensitivity experiments of Chapter 4. Advection of column moisture to the leeward side of the island in all experiments resulted in a model environment over the ocean on the leeward side of the island roughly 10% wetter than the base-state, which may mute the importance of a dry free-troposphere. Our simulations are also unable to produce any oceanic precipitation not associated with offshore propagation, unlike the real atmosphere where the SCS experiences substantial rainfall around the clock during the active BSISO phases. Thus, our representation of the active phase may not be entirely realistic without temporal mean moisture convergence. This shortcoming could likely be addressed with a more complex model such as WRF or RAMS.

We also envision future research stemming from the conclusions outlined in Chapter 4. For example, we hypothesized that offshore propagation is conditioned upon the presence of both a convectively generated cold pool, and the added effects of radiative surface cooling driving the land-breeze. We have not tested this hypothesis in this dissertation, but simulations in which the radiative and evaporative cooling mechanisms are turned off individually could address this. We also neglected variability in the land surface (i.e. soil moisture), and the sea surface temperature, which could be important contributors to diurnal cycle variability. Additionally, the final experiments of Chapter 4 in which the diurnal cycle of insolation was removed suggested the potential for an innate timescale in CM1 for producing tropical island-based convection. Exploring this result in more detail is beyond the scope of this dissertation, but the implications are an intriguing path for future analysis. This research also did not include a substantial analysis of these results in the context of extreme precipitation events such as flooding and prolonged droughts. This is another course for future research that could better tie these results to wider societal implications.

These proposed paths for future research would provide further clarity regarding the tropical island diurnal cycle and its offshore propagation.

# Bibliography

- Adler, R. F., and Coauthors, 2003: The version-2 global precipitation climatology project (GPCP) monthly precipitation analysis (1979-present). *J. Hydrometeor.*, **4**, 1147–1167.
- Annamalai, H., and J. M. Slingo, 2001: Active / break cycles: diagnosis of the intraseasonal variability of the Asian Summer Monsoon. *Climate Dyn.*, **18**, 85–102.
- Aves, S. L., and R. H. Johnson, 2008: The diurnal cycle of convection over the northern South China Sea. *J. Meteor. Soc. Japan*, **86**, 919–934.
- Bagtasa, G., 2017: Contribution of tropical cyclones to rainfall in the Philippines. *J. Climate*, **30**, 3621–3633.
- Bagtasa, G., 2020: Influence of Madden-Julian Oscillation on the intraseasonal variability of summer and winter monsoon rainfall in the Philippines. *J. Climate*, **33**, 9581–9594.
- Benjamin, T. B., 1968: Gravity currents and related phenomena. *J. Fluid Mech.*, **31**, 209–248.
- Bergemann, M., C. Jakob, and T. P. Lane, 2015: Global detection and analysis of coastline-associated rainfall using an objective pattern recognition technique. *J. Climate*, **28**, 7225–7236.
- Biasutti, M., S. E. Yuter, C. D. Burleyson, and A. H. Sobel, 2012: Very high resolution rainfall patterns measured by TRMM Precipitation Radar: Seasonal and diurnal cycles. *Climate Dyn.*, **39**, 239–258.
- Birch, C. E., S. Webster, S. C. Peatman, D. J. Parker, A. J. Matthews, Y. Li, and M. E. E. Hassim, 2016: Scale interactions between the MJO and the western Maritime Continent. *J. Climate*, **29**, 2471–2492.
- Bretherton, C. S., M. E. Peters, and L. E. Back, 2004: Relationships between water vapor path and precipitation over the tropical oceans. *J. Climate*, **17**, 1517–1528.

- Bryan, G. H., and J. M. Fritsch, 2002: A benchmark simulation for moist nonhydrostatic numerical models. *Mon. Wea. Rev.*, **130**, 2917–2928.
- Bryan, G. H., and H. Morrison, 2012: Sensitivity of a simulated squall line to horizontal resolution and parameterization of microphysics. *Mon. Wea. Rev.*, **140**, 202–225.
- Carbone, R. E., J. W. Wilson, T. D. Keenan, and J. M. Hacker, 2000: Tropical island convection in the absence of significant topography. Part I: Life cycle of diurnally forced convection. *Mon. Wea. Rev.*, **128**, 3459–3480.
- Cayanan, E. O., T.-C. Chen, J. C. Argete, M.-C. Yen, and P. D. Nilo, 2011: The effect of tropical cyclones on southwest monsoon rainfall in the Philippines. *J. Meteor. Soc. Japan*, **89A**, 123–139.
- Chatterjee, P., and B. N. Goswami, 2004: Structure, genesis and scale selection of the tropical quasi-biweekly mode. *Quart. J. Roy. Meteor. Soc.*, **130**, 1171–1194.
- Chen, G., and C.-H. Sui, 2010: Characteristics and origin of quasi-biweekly oscillation over the western North Pacific during boreal summer. *J. Geophys. Res.*, **115**, D14 113.
- Chen, R., Z. Wen, and R. Lu, 2016: Evolution of the circulation anomalies and the quasi-biweekly oscillations associated with extreme heat events in southern China. *J. Climate*, **29**, 6909–6921.
- Chen, T.-C., and J.-M. Chen, 1993: The 10-20 day mode of the 1979 Indian Monsoon: Its relation with the time variation of monsoon rainfall. *Mon. Wea. Rev.*, **121**, 2465–2482.
- Chen, T.-C., and J.-M. Chen, 1995: An observational study of the South China Sea monsoon during the 1979 summer: Onset and life cycle. *Mon. Wea. Rev.*, **123**, 2295–2318.
- Chen, T.-C., and K. Takahashi, 1995: Diurnal variation of outgoing longwave radiation in the vicinity of the South China Sea: Effect of intraseasonal oscillation. *Mon. Wea. Rev.*, **123**, 566–577.
- Chen, T.-C., M.-C. Yen, and S.-P. Weng, 2000: Interaction between the summer monsoons in east Asia and the South China Sea: Intraseasonal monsoon modes. *J. Atmos. Sci.*, **57**, 1373–1392.

- Chen, X., F. Zhang, and J. H. Ruppert, 2019: Modulations of the diurnal cycle of coastal rainfall over south China caused by the Boreal Summer Intraseasonal Oscillation. *J. Climate*, **32**, 2089–2108.
- Chen, X., F. Zhang, and K. Zhao, 2017: Influence of monsoonal wind speed and moisture content on intensity and diurnal variations of the Mei-Yu season coastal rainfall over south China. *J. Atmos. Sci.*, **74**, 2835–2856.
- Chudler, K., and S. A. Rutledge, 2021: The coupling between convective variability and large-scale flow patterns observed during PISTON 2018-2019. *J. Climate*, in press.
- Chudler, K., W. Xu, and S. A. Rutledge, 2020: Impact of the Boreal Summer Intraseasonal Oscillation on the diurnal cycle of precipitation near and over the island of Luzon. *Mon. Wea. Rev.*, **148**, 1805–1827.
- Ciesielski, P. E., and Coauthors, 2014: Quality-controlled upper-air sounding dataset for DYNAMO/CINTY/AMIE: development and corrections. *J. Atmos. Oceanic Technol.*, **31**, 741–764.
- Copernicus Climate Change Service (C3S), 2017: ERA5: Fifth generation of ECMWF atmospheric reanalyses of the global climate. Copernicus Climate Change Service Climate Data Store (CDS), URL <https://cds.climate.copernicus.eu/cdsapp#!/home>, accessed 16 February 2021.
- Coppin, D., and G. Bellon, 2019: Physical Mechanisms Controlling the Offshore Propagation of Convection in the Tropics: 1. Flat Island. *J. Adv. Model. Earth Syst.*, **11**, 3042–3056.
- Cronin, T. W., K. A. Emmanuel, and P. Molnar, 2015: Island precipitation enhancement and the diurnal cycle in radiative-convective equilibrium. *Quart J. Roy. Meteor. Soc.*, **141**, 1017–1034.
- Cruz, F. T., G. T. Narisma, M. Q. V. II, K. U. C. Chua, and L. M. Olaguera, 2013: A climatological analysis of the southwest monsoon rainfall in the Philippines. *Atmos. Res.*, **122**, 609–616.
- Dai, A., 2001: Global precipitation and thunderstorm frequencies. Part II: Diurnal variations. *J. Climate*, **14**, 1112–1128.

- Duchon, C. E., 1979: Lanczos filtering in one and two dimensions. *J. Appl. Meteor.*, **18**, 1016–1022.
- Durran, D. R., and J. B. Klemp, 1983: A compressible model for the simulation of moist mountain waves. *Mon. Wea. Rev.*, **111**, 2341–2361.
- Ferrett, S., G.-Y. Yang, S. J. Woolnough, J. Methven, K. Hodges, and C. E. Holloway, 2020: Linking extreme precipitation in Southeast Asia to equatorial waves. *Quart. J. Roy. Meteor. Soc.*, **146**, 665–684.
- Finkele, K., 1998: Inland and offshore propagation speeds of a sea breeze from simulations and measurements. *Bound.-Layer Meteor.*, **87**, 307–329.
- Fujita, M. K., K. Yoneyama, S. Mori, T. Nasuno, and M. Satoh, 2011: Diurnal convection peaks over the eastern Indian Ocean off Sumatra during different MJO phases. *J. Meteor. Soc. Japan*, **89A**, 317–330.
- Gao, M., J. Yang, B. Wang, S. Zhou, D. Gong, and S.-J. Kim, 2018: How are heat waves over Yangtze River valley associated with atmospheric quasi-biweekly oscillation? *Clim. Dyn.*, **51**, 4421–4437.
- Gill, A. E., 1980: Some simple solutions for heat-induced tropical circulation. *Quart. J. Roy. Meteor. Soc.*, **106**, 447–462.
- Gilman, D. L., F. J. Fuglister, and J. M. M. Jr., 1963: On the power spectrum of "Red Noise". *J. Atmos. Sci.*, **20**, 182–184.
- Grant, L. D., T. P. Lane, and S. C. van den Heever, 2018: The role of cold pools in tropical oceanic convective systems. *J. Atmos. Sci.*, **75**, 2615–2634.
- Grant, L. D., M. W. Moncrieff, T. P. Lane, and S. C. van den Heever, 2020: Shear-parallel tropical convective systems: Importance of cold pools and wind shear. *Geophys. Res. Lett.*, **47**, e2020GL087720.

- Grant, L. D., and S. C. van den Heever, 2016: Cold pool dissipation. *J. Geophys. Res. Atmos.*, **121**, 1138–1155.
- Gray, W. M., and R. W. Jacobson, 1977: Diurnal variation of deep cumulus convection. *Mon. Wea. Rev.*, **105**, 1171–1188.
- Hagos, S. M., C. Zhang, Z. Feng, C. D. Burleyson, C. DeMott, B. Kerns, J. J. Benedict, and M. N. Martini, 2016: The impact of the diurnal cycle on the propagation of Madden-Julian Oscillation convection across the Maritime Continent. *J. Adv. Model. Earth Syst.*, **8**, 1552–1564.
- Han, X., H. Zhao, X. Li, G. B. Raga, C. Wang, and Q. Li, 2020: Modulation of boreal extended summer tropical cyclogenesis over the northwest Pacific by the quasi-biweekly oscillation under different El Niño-southern oscillation phases. *Int. J. Climatol.*, **40**, 858–873.
- Hassim, M. E. E., T. P. Lane, and W. W. Grabowski, 2016: The diurnal cycle of rainfall over New Guinea in convection-permitting WRF simulations. *Atmos. Chem. Phys.*, **16**, 161–175.
- Hersbach, H., and Coauthors, 2020: The ERA5 global reanalysis. *Quart. J. Roy. Meteor. Soc.*, **146**, 1999–2049.
- Ho, C.-H., M.-S. Park, Y.-S. Choi, and Y. N. Takayabu, 2008: Relationship between intraseasonal oscillation and diurnal variation of summer rainfall over the South China Sea. *Geophys. Res. Lett.*, **35**, L03701.
- Holloway, C. E., and J. D. Neelin, 2009: Moisture vertical structure, column water vapor, and tropical deep convection. *J. Atmos. Sci.*, **66**, 1665–1683.
- Holloway, C. E., and J. D. Neelin, 2010: Temporal relations of column water vapor and tropical precipitation. *J. Atmos. Sci.*, **67**, 1091–1105.
- Hong, S.-Y., Y. Noh, and J. Dudhia, 2006: A new vertical diffusion package with an explicit treatment of entrainment processes. *Mon. Wea. Rev.*, **134**, 2318–2341.

- Houze, R. A., S. G. Geotis, F. D. M. Jr., and A. K. West, 1981: Winter monsoon convection in the vicinity of north Borneo. Part I: Structure and time variation of the clouds and precipitation. *Mon. Wea. Rev.*, **109**, 1595–1614.
- Huffman, G. J., and Coauthors, 2015: NASA Global Precipitation Measurement (GPM) Integrated Multi-satellitE Retrievals for GPM (IMERG). Algorithm Theoretical Basis Doc. (ATBD), version 06, 39 pp., accessed 7 July 2021.
- Ichikawa, H., and T. Yasunari, 2006: Time-space characteristics of diurnal rainfall over Borneo and surrounding oceans as observed by TRMM-PR. *J. Climate*, **19**, 1238–1260.
- Ichikawa, H., and T. Yasunari, 2008: Intraseasonal variability in diurnal rainfall over New Guinea and the surrounding oceans during austral summer. *J. Climate*, **21**, 2852–2868.
- Jiang, X., Á. F. Adames, M. Zhao, D. E. Waliser, and E. D. Maloney, 2018: A unified moisture mode framework for seasonality of the Madden-Julian Oscillation. *J. Climate*, **31**, 4215–4224.
- Jiménez, P. A., J. Dudhia, J. F. González-Ruoco, J. Navarro, J. P. Montávez, and E. García-Bustamante, 2012: A revised scheme for the WRF surface layer formulation. *Mon. Wea. Rev.*, **140**, 898–918.
- Joyce, R. J., J. E. Janowiak, P. A. Arkin, and P. Xie, 2004: CMORPH: A method that produces global precipitation estimates from passive microwave and infrared data at high spatial and temporal resolution. *J. Hydrometeor.*, **5**, 487–503.
- Keenan, T. D., and R. E. Carbone, 1992: A preliminary morphology of precipitation systems in tropical northern Australia. *Quart. J. Roy. Meteor. Soc.*, **118**, 283–326.
- Kerns, B. W., and S. S. Chen, 2016: Large-scale precipitation tracking and the MJO over the Maritime Continent and Indo-Pacific warm pool. *J. Geophys. Res. Atmos.*, **121**, 8755–8776.
- Kikuchi, K., and B. Wang, 2008: Diurnal precipitation regimes in the global tropics. *J. Climate*, **21**, 2680–2696.

- Kikuchi, K., and B. Wang, 2009: Global perspective of the quasi-biweekly oscillation. *J. Climate*, **22**, 1340–1359.
- Kikuchi, K., B. Wang, and Y. Kajikawa, 2012: Bimodal representation of the tropical intraseasonal oscillation. *Climate Dyn.*, **38**, 1989–2000.
- Kiladis, G. N., J. Dias, K. H. Straub, M. C. Wheeler, S. N. Tulich, K. Kikuchi, K. M. Weickmann, and M. J. Ventrice, 2014: A comparison of OLR and circulation-based indices for tracking the MJO. *Mon. Wea. Rev.*, **142**, 1697–1715.
- Kilpatrick, T., S.-P. Xie, and T. Nasuno, 2017: Diurnal convection-wind coupling in the Bay of Bengal. *J. Geophys. Res.*, **122**, 9705–9720.
- Kim, H.-M., D. Kim, F. Vitart, V. E. Toma, J.-S. Kug, and P. J. Webster, 2016: MJO propagation across the Maritime Continent in the ECMWF Ensemble Prediction System. *J. Climate*, **29**, 3973–3988.
- Knapp, K. R., H. J. Diamond, J. P. Kossin, M. C. Kruk, and C. J. Schreck, 2018: NCDC International Best Track Archive for Climate Stewardship (IBTrACS) Project, Version 4. NOAA National Centers for Environmental Information, accessed 8 July 2021.
- Knapp, K. R., M. C. Kruk, D. H. Levinson, H. J. Diamond, and C. J. Neumann, 2010: The International Best Track Archive for Climate Stewardship (IBTrACS): Unifying tropical cyclone best track data. *Bull. Amer. Meteor. Soc.*, **91**, 363–376.
- Ko, K.-C., and H.-H. Hsu, 2006: Sub-monthly circulation features associated with Tropical Cyclone tracks over the East Asian monsoon area during July-August season. *J. Meteor. Soc. Japan*, **84**, 871–889.
- Ko, K.-C., and H.-H. Hsu, 2009: ISO modulation on the submonthly wave pattern and recurving tropical cyclones in the tropical western North Pacific. *J. Climate*, **22**, 582–599.

- Krishnamurti, T. N., and P. Ardanuy, 1980: The 10 to 20-day westward propagating mode and "Breaks in the Monsoons". *Tellus*, **32**, 15–26.
- Krishnamurti, T. N., and H. N. Bhalme, 1976: Oscillations of a monsoon system. part i. observational aspects. *J. Atmos. Sci.*, **33**, 1937–1954.
- Kuo, Y.-H., J. D. Neelin, and C. R. Mechoso, 2017: Tropical convection transition statistics and causality in the water vapor-precipitation relation. *J. Atmos. Sci.*, **74**, 915–931.
- Lafore, J.-P., and M. W. Moncrieff, 1989: A numerical investigation of the organization and interaction of the convective and stratiform regions of tropical squall lines. *J. Atmos. Sci.*, **46**, 521–544.
- Lane, T. P., and M. J. Reeder, 2001: Convectively generated gravity waves and their effect on the cloud environment. *J. Atmos. Sci.*, **58**, 2427–2440.
- Lane, T. P., and F. Zhang, 2011: Coupling between gravity waves and tropical convection at mesoscales. *J. Atmos. Sci.*, **68**, 2582–2598.
- Lee, C.-A., W.-R. Huang, Y.-H. Chang, and S.-M. Huang, 2021: Impact of multiple-scale circulation interactions on the spring diurnal precipitation over Luzon. *Sci. Rep.*, **11**, 9937.
- Lee, J.-Y., B. Wang, M. C. Wheeler, X. Fu, D. E. Waliser, and I.-S. Kang, 2013: Real-time multivariate indices for the boreal summer intraseasonal oscillation over the Asian summer monsoon region. *Climate Dyn.*, **40**, 493–509.
- LeMone, M. A., G. M. Barnes, and E. J. Zipser, 1984: Momentum flux by lines of cumulonimbus over the tropical oceans. *J. Atmos. Sci.*, **41**, 1914–1932.
- Li, K., Y. Yang, L. Feng, W. Yu, and S. Liu, 2020: Structures and northward propagation of the Quasi-Biweekly oscillation in the western north Pacific. *J. Climate*, **33**, 6873–6888.
- Liang, Z., and D. Wang, 2017: Sea breeze and precipitation over Hainan Island. *Quart. J. Roy. Meteor. Soc.*, **143**, 137–151.

- Liang, Z., D. Wang, Y. Liu, and Q. Cai, 2017: A numerical study of the convection triggering and propagation associated with sea breeze circulation over Hainan Island. *J. Geophys. Res. Atmos.*, **122**, 8567–8592.
- Liebmann, B., and C. A. Smith, 1996: Description of a complete (interpolated) outgoing longwave radiation dataset. *Bull. Amer. Meteor. Soc.*, **77**, 1275–1277.
- Liu, C., and M. W. Moncrieff, 1996: A numerical study of the effects of ambient flow and shear on density currents. *Mon. Wea. Rev.*, **124**, 2282–2303.
- Liu, H.-B., J. Yang, D.-L. Zhang, and B. Wang, 2014: Roles of synoptic to quasi-biweekly disturbances in generating the summer 2003 heavy rainfall in east China. *Mon. Wea. Rev.*, **142**, 886–904.
- Love, B. S., A. J. Matthews, and G. M. S. Lister, 2011: The diurnal cycle of precipitation over the Maritime Continent in a high resolution f model. *Quart. J. Roy. Meteor. Soc.*, **137**, 934–947.
- Lu, J., T. Li, and L. Wang, 2019: Precipitation diurnal cycle over the Maritime Continent modulated by the MJO. *Clim. Dyn.*, **53**, 6489–6501.
- Madden, R. A., and P. R. Julian, 1971: Detection of a 40-50 day oscillation in the zonal wind in the tropical Pacific. *J. Atmos. Sci.*, **28**, 702–708.
- Madden, R. A., and P. R. Julian, 1972: Description of global-scale circulation cells in the tropics with a 40-50 day period. *J. Atmos. Sci.*, **29**, 1109–1123.
- Madden, R. A., and P. R. Julian, 1994: Observations of the 40–50-Day tropical oscillation - A review. *Mon. Wea. Rev.*, **22**, 813–837.
- Maloney, E. D., and D. L. Hartmann, 1998: Frictional moisture convergence in a composite life cycle of the Madden-Julian oscillation. *J. Climate*, **11**, 2387–2403.

- Mapes, B. E., T. T. Warner, and M. Xu, 2003: Diurnal patterns of rainfall in northwestern South America. Part III: Diurnal gravity waves and nocturnal convection offshore. *Mon. Wea. Rev.*, **131**, 830–844.
- Matsumoto, J., L. M. P. Olaguera, D. Nguyen-Le, H. Kubota, and M. Q. V. II, 2020: Climatological seasonal changes of wind and rainfall in the Philippines. *Int. J. Climatol.*, **40**, 4843–4857.
- Matsuno, T., 1966: Quasi-geostrophic motions in the equatorial area. *J. Meteor. Soc. Japan*, **44**, 25–43.
- Mori, S., J.-I. Hamada, Y. I. Tauhid, and M. D. Yamanaka, 2004: Diurnal land-sea rainfall peak migration over Sumatera island, Indonesian Maritime Continent, observed by TRMM satellite and intensive rawinsonde soundings. *Mon. Wea. Rev.*, **132**, 2021–2039.
- Moron, V., A. Lucero, F. Hilario, B. Lyon, A. W. Robertson, and D. DeWitt, 2009: Spatio-temporal variability and predictability of summer monsoon onset over the Philippines. *Clim. Dyn.*, **33**, 1159–1177.
- National Geophysical Data Center, 2006: 2-minute Gridded Global Relief Data (ETOPO2)v2. NOAA, accessed 12 February 2018, <https://doi.org/10.7289/V5J1012Q>.
- Natoli, M. B., and E. D. Maloney, 2019: Intraseasonal variability of the diurnal cycle of precipitation in the Philippines. *J. Atmos. Sci.*, **76**, 3633–3654.
- Neale, R., and J. Slingo, 2003: The Maritime Continent and its role in the global climate: A GCM study. *J. Climate*, **16**, 834–848.
- Nicholls, M. E., R. H. Johnson, and W. R. Cotton, 1988: The sensitivity of two-dimensional simulations of tropical squall lines to environmental profiles. *J. Atmos. Sci.*, **45**, 3625–3649.
- Oh, J.-H., B.-M. Kim, K.-Y. Kim, H.-J. Song, and G.-H. Lim, 2013: The impact of the diurnal cycle on the MJO over the Maritime Continent: a modeling study assimilating TRMM rain rate into global analysis. *Clim. Dyn.*, **40**, 893–911.

- Oh, J.-H., K.-Y. Kim, and G.-H. Lim, 2012: Impact of MJO on the diurnal cycle of rainfall over the western Maritime Continent in the austral summer. *Climate Dyn.*, **38**, 1167–1180.
- Olaguera, L. M. P., J. Matsumoto, H. Kubota, E. O. Cayan, and F. D. Hilario, 2020: A climatological analysis of the monsoon break following the summer monsoon onset over Luzon Island, Philippines. *Int. J. Climatol.*, **41**, 2100–2117.
- Park, M.-S., C.-H. Ho, J. Kim, and R. L. Elsberry, 2011: Diurnal circulations and their multi-scale interaction leading to rainfall over the South China Sea upstream of the Philippines during intraseasonal monsoon westerly wind bursts. *Climate Dyn.*, **37**, 1483–1499.
- Peatman, S. C., A. J. Matthews, and D. P. Stevens, 2014: Propagation of the Madden-Julian Oscillation through the Maritime Continent and scale interaction with the diurnal cycle of precipitation. *Quart. J. Roy. Meteor. Soc.*, **140**, 814–825.
- Peatman, S. C., J. Schwendike, C. E. Birch, J. H. Marsham, A. J. Matthews, and G.-Y. Yang, 2021: A Local-to-Large Scale View of Maritime Continent Rainfall: Control by ENSO, MJO, and Equatorial Waves. *J. Climate*, **34**, 8933–8953.
- Peters, K., and C. Hohenegger, 2017: On the dependence of squall-line characteristics on surface conditions. *J. Atmos. Sci.*, **74**, 2211–2228.
- Qian, J. H., 2020: Mechanisms for the dipolar patterns of rainfall variability over large islands in the Maritime Continent associated with the Madden-Julian oscillation. *J. Atmos. Sci.*, **77**, 2257–2278.
- Qian, Y., P.-C. Hsu, and K. Kikuchi, 2019: New real-time indices for the quasi-biweekly oscillation over the Asian summer monsoon region. *Clim. Dyn.*, **53**, 2603–2624.
- Ramage, C. S., 1968: Role of a tropical "Maritime Continent" in the atmospheric circulation. *Mon. Wea. Rev.*, **96**, 365–370.

- Rauniyar, S. P., and K. J. E. Walsh, 2011: Scale interaction of the diurnal cycle of rainfall over the Maritime Continent and Australia: Influence of the MJO. *J. Climate*, **24**, 325–348.
- Rauniyar, S. P., and K. J. E. Walsh, 2013: Influence of ENSO on the diurnal cycle of rainfall over the Maritime Continent and Australia. *J. Climate*, **26**, 1304–1321.
- Riley, E. M., B. E. Mapes, and S. N. Tulich, 2011: Clouds associated with the Madden-Julian Oscillation: A new perspective from *CloudSat*. *J. Atmos. Sci.*, **68**, 3032–3051.
- Riley Dellaripa, E. M., E. D. Maloney, B. A. Toms, S. M. Saleeby, and S. C. van den Heever, 2020: Topographic effects on the Luzon diurnal cycle during the BSISO. *J. Atmos. Sci.*, **77**, 3–30.
- Robinson, F. J., S. C. Sherwood, and Y. Li, 2008: Resonant response of deep convection to surface hot spots. *J. Atmos. Sci.*, **65**, 276–286.
- Rotunno, R., J. B. Klemp, and M. L. Weisman, 1988: A theory for strong, long-lived squall lines. *J. Atmos. Sci.*, **45**, 463–485.
- Ruppert, J. H., and X. Chen, 2020: Island rainfall enhancement in the Maritime Continent. *Geophys. Res. Lett.*, **47**, e2019GL086545.
- Ruppert, J. H., X. Chen, and F. Zhang, 2020: Convectively forced diurnal gravity waves in the Maritime Continent. *J. Atmos. Sci.*, **77**, 1119–1136.
- Ruppert, J. H., and F. Zhang, 2019: Diurnal forcing and phase locking of gravity waves in the Maritime Continent. *J. Atmos. Sci.*, **76**, 2815–2835.
- Sahlu, D., E. I. Nikolopoulos, S. A. Moges, E. N. Anagnostou, and D. Hailu, 2016: First evaluation of the day-1 IMERG over the upper Blue Nile basin. *J. Hydrometeor.*, **17**, 2875–2882.
- Saito, K., T. Keenan, G. Holland, and K. Puri, 2001: Numerical simulation of the diurnal evolution of tropical island convection over the Maritime Continent. *Mon. Wea. Rev.*, **129**, 378–400.

- Sakaeda, N., G. Kiladis, and J. Dias, 2020: The diurnal cycle of rainfall and the convectively coupled equatorial waves over the Maritime Continent. *J. Climate*, **33**, 3307–3331.
- Sakaeda, N., G. N. Kiladis, and J. Dias, 2017: The diurnal cycle of tropical cloudiness and rainfall associated with the Madden-Julian oscillation. *J. Climate*, **30**, 3999–4020.
- Sakurai, N., and Coauthors, 2005: Diurnal cycle of cloud system migration over sumatera island. *J. Meteor. Soc. Japan*, **83**, 835–850.
- Shige, S., Y. Nakano, and M. K. Yamamoto, 2017: Role of orography, diurnal cycle, and intraseasonal oscillation in summer monsoon rainfall over the Western Ghats and Myanmar coast. *J. Climate*, **30**, 9365–9381.
- Short, E., C. L. Vincent, and T. P. Lane, 2019: Diurnal cycle of surface winds in the Maritime Continent observed through satellite scatterometry. *Mon. Wea. Rev.*, **147**, 2023–2044.
- Sobel, A. H., J. Sprintall, E. D. Maloney, Z. K. Martin, S. Wang, S. P. de Szoeke, B. C. Trabling, and S. A. Rutledge, 2021: Large-scale state and evolution of the atmosphere and ocean during PISTON 2018. *J. Climate*, **34**, 5017–5035.
- Sui, C.-H., and K.-M. Lau, 1992: Multiscale phenomena in the tropical atmosphere over the western Pacific. *Mon. Wea. Rev.*, **120**, 407–430.
- Tan, H., P. Ray, B. Barrett, J. Dudhia, and M. W. Moncrieff, 2021: Systematic patterns in land precipitation due to convection in neighboring islands in the Maritime Continent during MJO Propagation. *J. Geophys. Res. Atmos.*, **126**, e2020JD033 465.
- Tao, L., X. Fu, and W. Lu, 2009: Moisture structure of the quasi-biweekly mode revealed by AIRS in western Pacific. *Adv. Atmos. Sci.*, **26**, 513–522.
- Tulich, S. N., and B. E. Mapes, 2008: Multiscale convective wave disturbances in the tropics: Insights from a two-dimensional cloud-resolving model. *J. Atmos. Sci.*, **65**, 140–155.

- Tulich, S. N., D. A. Randall, and B. E. Mapes, 2007: Vertical-mode and cloud decomposition of large-scale convectively coupled gravity waves in a two-dimensional cloud-resolving model. *J. Atmos. Sci.*, **64**, 1210–1229.
- Vincent, C. L., and T. P. Lane, 2016: Evolution of the diurnal precipitation cycle with the passage of a Madden-Julian oscillation event through the Maritime Continent. *Mon. Wea. Rev.*, **144**, 1983–2005.
- Vincent, C. L., and T. P. Lane, 2017: A 10-Year Austral summer climatology of observed and modeled intraseasonal, mesoscale, and diurnal variations over the Maritime Continent. *J. Climate*, **30**, 3807–3828.
- Vincent, C. L., and T. P. Lane, 2018: Mesoscale variation in diabatic heating around Sumatra, and its modulation with the Madden-Julian Oscillation. *Mon. Wea. Rev.*, **146**, 2599–2614.
- Virts, K. S., J. M. Wallace, M. L. Hutchins, and R. H. Holzworth, 2013: Diurnal lightning variability over the Maritime Continent: Impact of low-level winds, cloudiness, and the MJO. *J. Atmos. Sci.*, **70**, 3128–3146.
- Wang, B., and X. Xu, 1997: Northern Hemisphere summer monsoon singularities and climatological intraseasonal oscillation. *J. Climate*, **10**, 1071–1085.
- Wang, S., D. Ma, A. H. Sobel, and M. K. Tippett, 2018: Propagation characteristics of BSISO indices. *Geophys. Res. Lett.*, **45**, 9934–9943.
- Wang, S., and A. H. Sobel, 2017: Factors controlling rain on small tropical islands: Diurnal cycle, large-scale wind speed, and topography. *J. Atmos. Sci.*, **74**, 3515–3532.
- Wang, S., and A. H. Sobel, 2022: A unified moisture mode theory for the Madden-Julian oscillation and the boreal summer intraseasonal oscillation. *J. Climate*, **35**, 1267–1291.
- Wheeler, M., and H. H. Hendon, 2004: An all-season real-time multivariate MJO index: Development of an index for monitoring and prediction. *Mon. Wea. Rev.*, **132**, 1917–1932.

- Wu, P., D. Ardiansyah, S. Yokoi, S. Mori, F. Syamsudin, and K. Yoneyama, 2017: Why torrential rain occurs on the western coast of Sumatra island at the leading edge of the MJO westerly wind bursts. *SOLA*, **13**, 36–40.
- Wu, P., S. Mori, and F. Syamsudin, 2018: Land-sea surface air temperature contrast on the western coast of Sumatra island during an active phase of the Madden-Julian Oscillation. *Prog. Earth Planet. Sci.*, **5**, 4.
- Xie, P., R. Joyce, S. Wu, S.-H. Yoo, Y. Yarosh, F. Sun, and R. Lin, 2017: Reprocessed, bias-corrected CMORPH global high-resolution precipitation estimates from 1998. *J. Hydrometeor.*, **18**, 1617–1641.
- Xu, W., and S. A. Rutledge, 2018: Convective variability associated with the Boreal Summer Intraseasonal Oscillation in the South China Sea region. *J. Climate*, **31**, 7363–7383.
- Xu, W., S. A. Rutledge, and K. Chudler, 2021: Diurnal cycle of coastal convection in the South China Sea Region and modulation by the BSISO. *J. Climate*, **34**, 4297–4314.
- Yan, X., S. Yang, T. Wang, E. D. Maloney, S. Dong, W. Wei, and S. He, 2019: Quasi-biweekly oscillation of the Asian monsoon rainfall in late summer and autumn: different types of structure and propagation. *Clim. Dyn.*, **53**, 6611–6628.
- Yanase, A., K. Yasunaga, and H. Masunaga, 2017: Relationship between the direction of diurnal rainfall migration and the ambient wind over the southern Sumatra island. *Earth and Space Science*, **4**, 117–127.
- Yang, G.-Y., and J. Slingo, 2001: The diurnal cycle in the tropics. *Mon. Wea. Rev.*, **129**, 784–801.
- Yang, J., B. Wang, and B. Wang, 2008: Anticorrelated intensity change of the quasi-biweekly and 30-50-day oscillations over the South China Sea. *Geophys. Res. Lett.*, **35**, L16 702.

- Yokoi, S., S. Mori, M. Katsumata, B. Geng, K. Yasunaga, F. Syamsudin, Nurhayati, and K. Yoneyama, 2017: Diurnal cycle of precipitation observed in the western coastal area of Sumatra island: Offshore preconditioning by gravity waves. *Mon. Wea. Rev.*, **145**, 3745–3761.
- Yokoi, S., S. Mori, F. Syamsudin, U. Haryoko, and B. Geng, 2019: Environmental conditions for nighttime offshore migration of precipitation area as revealed by in situ observation off Sumatra Island. *Mon. Wea. Rev.*, **147**, 3391–3407.
- Yusef, A. A., and H. Francisco, 2009: Climate change vulnerability mapping for Southeast Asia, Economy and Environment Program for Southeast Asia (EEPSEA) report, June 2009. Economy and Environment Program for Southeast Asia, available online at <http://www.eepsea.org>, 32pp pp.
- Zhang, C., and J. Ling, 2017: Barrier effect of the Indo-Pacific Maritime Continent on the MJO: Perspectives from tracking MJO precipitation. *J. Climate*, **30**, 3439–3459.
- Zhong, S., and E. S. Takle, 1993: The effects of large-scale winds on the sea-land-breeze circulations in an area of complex coastal heating. *J. Appl. Meteor.*, **32**, 1181–1195.
- Zhou, H., P.-C. Hsu, and Y. Qian, 2018: Close linkage between quasi-biweekly oscillation and tropical cyclone intensification over the western north pacific. *Atmos. Sci. Lett.*, **19**, e826.
- Zhu, L., Z. Meng, F. Zhang, and P. M. Markowski, 2017: The influence of sea- and land-breeze circulations on the diurnal variability in precipitation over a tropical island. *Atmos. Chem. Phys.*, **17**, 13 213–13 232.